INVESTIGATING THE REACTIVITY OF SIZE-SELECTED METAL OXIDE CLUSTERS FOR ORGANOPHOSPHORUS NERVE AGENT DECOMPOSITION

By

Nicolas G. Blando

A dissertation submitted to Johns Hopkins University in conformity with the requirements of the degree of Doctor of Philosophy.

Baltimore, Maryland

August 2020

Abstract

Metal and metal oxide nanostructures of varying size and composition are currently the industry standard for protection against chemical warfare agents (CWAs), yet there is limited understanding of the effects that the size and composition of the nanostructures have on the reaction mechanisms. Ultra-small, size-selected metal oxide clusters offer the opportunity of a nearly limitless number of unstudied candidate species as well as a chance to understand reactivity trends that may drive the discovery of more engineered catalysts. Clusters are small aggregates of atoms, <1000, which often display intriguing properties in that size range due quantum confinement, undercoordination and other emergent properties. In this work, the history and development of molecular beam techniques that support the study of size-selected clusters *in-vacuo* are discussed, leading up to the construction of a novel beamline apparatus designed for the synthesis and deposition of size-selected clusters for reactivity studies. Using these techniques, size selected manganese oxide, niobium oxide, tungsten oxide, copper molybdenum oxide, and copper zirconium oxide clusters were each studied for their ability to adsorb and decompose the organophosphorus nerve agent simulant dimethyl methylphosphonate.

Advisor: Dr. Kit H. Bowen

Committee: Dr. Howard Fairbrother

Dr. Lan Cheng

Acknowledgments

I have been amazingly lucky to have the mentors and support that has allowed me, and even pushed me, to make it to this point.

First, I'd like to thank my PhD advisor, Dr. Kit Bowen, who has given me every opportunity to succeed and become a better scientist and experimentalist. I recognize that my path to Johns Hopkins and to becoming a successful experimentalist was largely because he saw potential in me, and I could never thank him enough for that opportunity. Besides the important laboratory experience and mentorship he offered, I'd like to thank him for the opportunity to attend large conferences around the US and world, where experiences I had with collaborators and peers will be cherished forever.

Second, I'd like to thank my graduate research committee members, Dr. Howard Fairbrother, Dr. Lan Cheng, and Dr. Art Bragg, for taking the time to be part of my graduate career. I'm particularly grateful to Dr. Fairbrother as well as his students for their support over the years.

Next I would like to thank the members of my "sub-group", the surface team, who have I have spent the last 3 years getting to know. I will forever be indebted to Dr. Zachary Hicks, our original sub-group leader, for the potential he saw in me and his decision to bring me into his project. His never-ending curiosity and drive were a wonderful example for a young scientist. Learning from and getting to know Linjie Wang has been one of the high points of my graduate career. She is a thoughtful and caring person, but as a scientist her power of deduction is without equal, and it has been a privilege to learn from and with her these last few years. Similarly, learning from Mike Denchy and watching him grow into an adept scientist the last couple years has been a privilege, his unwavering determination to fully understand the system or project at hand will continue to serve him well in life. In my short time with Ben Bilik, I have been impressed by his curiosity, and know that he will be extremely successful if he can apply that in the Bowen Lab, and similarly, Lucas Hansen's theoretical prowess will make him a strong experimentalist.

Throughout my 6 years in the Bowen lab, there is no one I have been closer to than Dr. Sandra Ciborowski. Her companionship since the very first day of graduate classes and the years of friendship and support since have been invaluable. She is a brilliant scientist and adept problem solver that I know will continue to impress others. Similarly, Mary Marshall was one of the first graduate students I worked closely with, and it has been a great experience to watch her grow into an adept experimentalist, whose advise I often seek, for both science and life questions. It has been gratifying to watch Zhaoguo Zhu become an extremely talented and well-rounded scientist, his personality will continue to brighten rooms wherever he goes. Rachel Harris is an extremely determined scientist and engineer, I have no doubt her tenacity will take her far after she is done at Johns Hopkins.

My undergraduate research advisor Kris Hagel is responsible for introducing me to experimental physics, and I will always be grateful that he started that ball rolling. His enthusiasm and ingenuity set a high bar for any scientist.

I'd like to thank the chemistry building manager, Boris Steinberg, who has been a great resource for work problems and life advice, and does an enormous amount of work behind the scenes to facilitate our research.

My brother Robert for believing in me when no one, including myself, did.

I'd like to thank my partner Allie for the endless adventures and unwavering support she has offered.

And finally, my parents, without whom I would certainly not be here today. They provided me all the opportunity and skills that I could ever need, but it was their support along the way that I cherish most.

Table of Contents

List of Figures

I Atoms to Clusters

The word atom originates from the Greek words *a-* meaning not and *temnien* meaning to cut. Around 400BC, the Greek philosophers Leucippus and Democritus theorized that matter cannot be subdivided infinitely, that there must be some bit of matter, too small to be seen, that can no longer be divided. They coined this indivisible entity *atomos.* It only took 2,300 more years for John Dalton to consider and develop the first theory of the atom, and even created the first symbols to represent different elements **(Figure I-I)**. (1) (2)

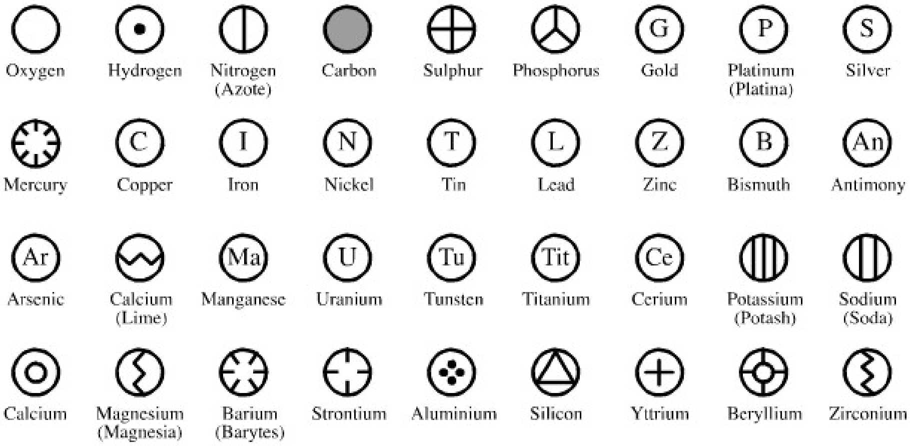

***Figure I-I**: John Dalton's 3rd list of elements published in 1827.* (2)

Growing inadequacies found in Dalton's hard sphere model by early physicists came to a boil at the Cavendish Laboratory in Cambridge University at the end of the 19th century. Succeeding famous scientists James Maxwell and Lord Rayleigh as the leader of the laboratory, J.J. Thomson set up cutting edge experiments discussed in depth in Section III, to measure the mass-to-charge ratio of the small negatively charged particles that constituted *cathode rays*, termed *corpuscles,* but we now know as electrons. (3) In groundbreaking work published in 1904, Thomson lays out the theory replacing Dalton's hard sphere model of an atom with the idea that an atom is a positively charged spherical volume with small negatively charged entities distributed within, balancing the charge; in his own words,

"We have thus in the first place a sphere of uniform positive electrification, and inside this sphere a number of corpsucles arranged in a series of parallel rings, the number of corpuscles in a ring varying from ring to ring." (4)

One of Thomson's early lab assistants and his eventual successor at Cavendish, Ernest Rutherford, left Cavendish after Thomson's famous discovery in order to carve out a name for himself. In 1908 Rutherford won a Nobel Prize "for his investigations into the disintegration of the elements, and the chemistry of radioactive substances", and is credited for the terms *alpha, beta* and *gamma* radiation. Surprisingly, his most famous work was yet to come. Considering his work on nuclear decay and the earlier work with J.J. Thomson on the atomic model, Rutherford's famous gold foil experiments (III.1) led to his proposal in 1911 of an atomic model where the negatively charged particles were distributed around a small positively charged center, rather than being dispersed in a positively charged volume. (3)

Soon after in 1913, Niels Bohr, seeking to explain the spectrographic lines emitting from the sun that follow the famous Balmer series, modified Rutherford's model to show that electrons moved around the nucleus in fixed (quantized) orbits. Reasoning that electrons can only have discrete values of angular momentum, the model dictated circular orbits with fixed radii and Bohr was finally able to account for the series of characteristic wavelength emission lines from the sun that Balmer observed. With this model, Bohr explained how light absorption or radiation from an atom is intrinsically tied to the movement of an electron between discrete orbits which correspond to different electron energy levels, as described in **Figure I-II**. (5)

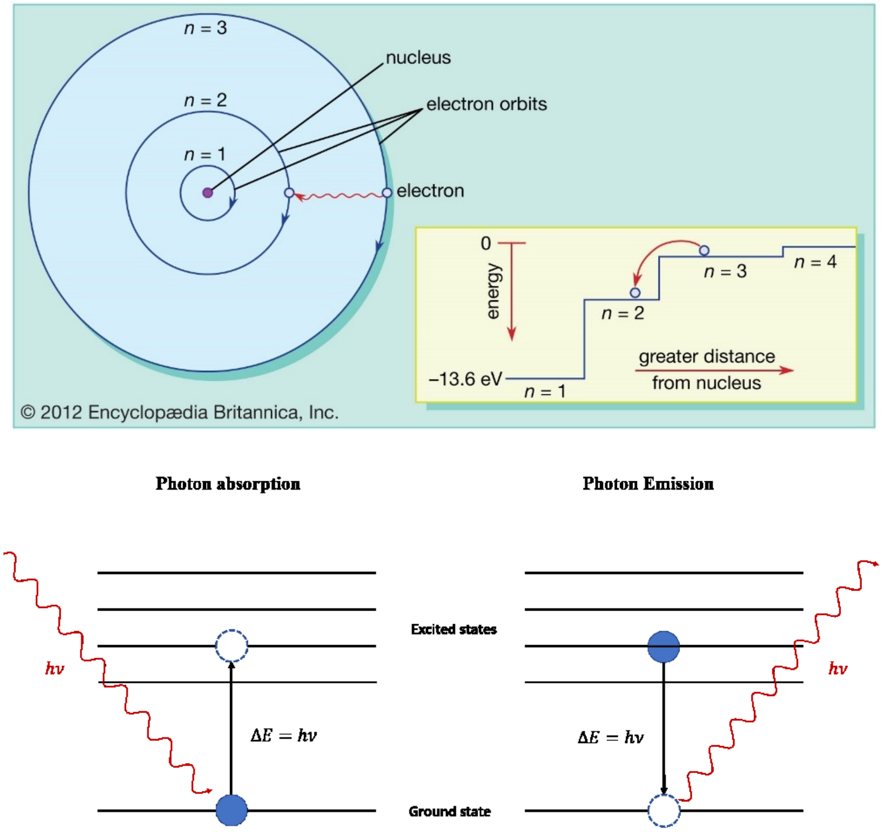

Figure I-II: *Top: Energy Level diagram of a hypothetical hydrogen atom. Bottom: absorption and emission diagrams for a hypothetical two-state system. (5)*

With the energy of a photon equal to hv, we know that the change in energy of an electron during emission or absorption is

$$\Delta E = hv$$

Equation 1

Bohr's model did not resolve every failing of Rutherford's nuclear model, it couldn't explain emission spectra from heavier elements, and violated the Heisenberg uncertainty principle by defining both the position and the momentum of an electron.

Finally, in 1926, after studying the problem extensively, Erwin Schrodinger famously proposed that electrons should not be considered as particles on discrete orbits, but as waves. After discussing Einstein's particle wave duality with Peter Debye, Schrodinger decided to begin with the standing wave that music theorists had popularized, and developed the historic Schrödinger equation, which initially described the motion of an electron in the hydrogen atom, but can be used to describe any quantum-mechanical system. (6)

$$i\hbar\frac{\partial}{\partial t}\Psi(\vec{\boldsymbol{r}},t)=\left[-\frac{\hbar^2}{2m}\nabla^2+V(\vec{\boldsymbol{r}},t)\right]\Psi(\vec{\boldsymbol{r}},t)$$

Equation 2

As scientists began to study atoms and molecules with the theory to accompany it, many began to probe the interface between the classical chemical properties of bulk materials and those of lone atoms or molecules. At what point in the range of particle sizes did materials behave like a collection of discrete entities rather than a bulk entity? It was quickly found that, like one might imagine, properties often did not change all at once, and instead followed trends related to the size of the material, i.e. the number of atoms. In the 1960's, Texas A&M professor Frank Cotton coined the term "cluster" to refer to small aggregates of metal or metal oxide molecules held together primarily by metal-metal bonds. Since then, the word cluster has come to refer to any ultrasmall aggregates of atoms and molecules, from 2 atoms to a few thousand, held together by Van der Waals or stronger forces. (7)

Clusters are attractive for a range of applications due to the bizarre properties they possess in the nanometer size range. In some semiconductor nanoparticles, called quantum dots, as the diameter of a semiconductor particle approaches the Bohr radius, quantum confinement restricts exitons to discrete energy levels. Analogous to the particle in a box system, increasing the diameter of a quantum dot reduces the band gap and the absorption and fluorescence spectra are *redshifted.* Similarly, metals such as magnesium exhibit the emergent property of a conductor in the bulk but semiconductor at the atomic level. Photoelectron studies of size-selected Mg_n clusters in a molecular beam experiment demonstrated that the combining atomic orbitals led to a reduction in the HOMO-LUMO gap until $n \approx 18$, where the HOMO (highest occupied molecular orbital) and LUMO (lowest unoccupied molecular orbital) begin to overlap, producing the conduction band expected for a metal[4], illustrated below in **Figure I-III**.

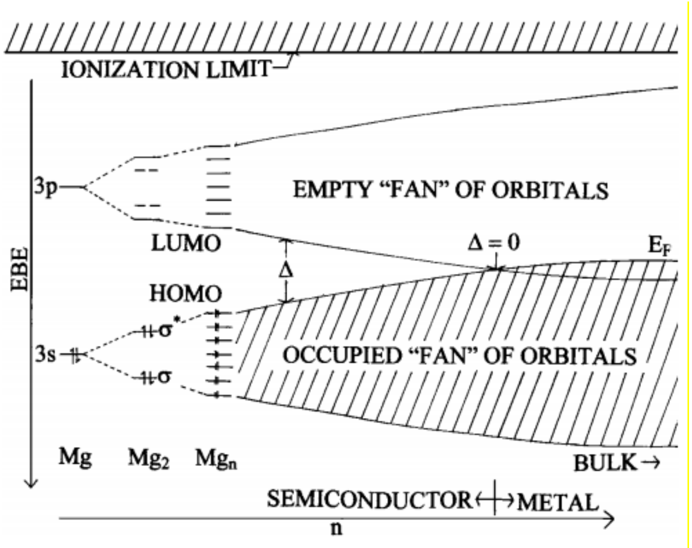

Figure I-III *Evolution of Mg conduction band as a function of cluster size. (8)*

This study highlights the emergence of properties on an atom-by-atom basis and demonstrates the potential to engineer highly specific reactivity in size-selected clusters. The fine line between unreactive and overly reactive can be carefully probed via size dependence to discover an optimal interaction.

References

1. STRUCTURE OF THE TERMS IN THE FIELD OF NUCLEAR PHYSICS. **Z Serikbekova, N.P. Golovin.** s.l. : 8th International Conference "Social Science and Humanity", 2018.

2. **Dalton, John.** John Dalton's Periodic Tables. *sussexvt.k12.de.us.* [Online] [Cited: 07 12, 2020.]

http://www.sussexvt.k12.de.us/science/the%20history%20of%20the%20world%201500-1899/john%20dalton%27s%20periodic%20tables.htm.

3. **Baron, Maximo.** J.J. Thomsons Atom:. [book auth.] Akhlesh Lakhtakia. *Models and Modelers of Hydrogen: Thales, Thomson, Rutherford, Bohr, Sommerfeld, Goudsmit, Heisenberg, Schrodinger, Dirac, Sallhofer.* s.l. : World Scientific, 1996.

4. *On the Structure of the Atom.* **Tompson, J.J.** s.l. : Phylos Mag , 1904, Vol. 7.

5. **The Editors of Encyclopaedia Britannica.** Encyclopaedia Britannica. *Bohr Model.* [Online] January 23, 2020. [Cited: 07 25, 2020.] https://www.britannica.com/science/Bohr-model.

6. **Zyga, Lisa.** On the origins of the Schrodinger equation. *Phys.org.* [Online] April 8, 2013. [Cited: 07 25, 2020.] https://phys.org/news/2013-04-schrodinger-equation.html.

7. *Metal Atom Clusters in Oxide Systems.* **Cotton, F.A.** 9, s.l. : Inorganic Chemistry, 1964, Vol. 3.

8. **Thomas, Owen C., et al.** "Onset of metallic behavior in magnesium clusters." *Physical review letters* 89.21 (2002): 213403.

II Catalysis

Several industries were quick to explore the potential offered by the size-induced effects of small “clusters”, but few so much as the catalytic industry. Humans have been using catalysts for thousands of years to increase reaction rates, while fermenting alcohol or tanning leather, for instance. Since then, advances in thermodynamics and kinetics have elucidated the source of this phenomenon.

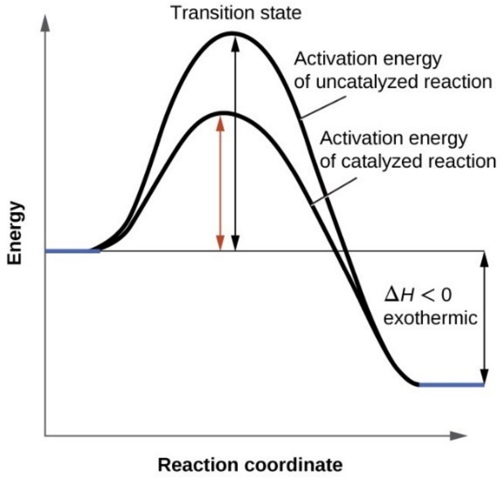

Figure II-I: *Catalytic reaction energy coordinate diagram. (5)*

The general phenomenon is illustrated in **Figure II-I**; in the presence of a catalyst, the reaction can proceed via the pathway with the lower activation energy. From the Arrhenius equation, where k is the reaction rate and R is the ideal gas constant, we can see that by discovering a catalyst that catalyzes a reaction and reduces the activation energy, E_a, the reaction rate is increased an exponential amount.

$$k = Ae^{-\frac{E_a}{RT}}$$

Equation 3

Catalysts are distinguished as either heterogeneous or homogeneous by the phases of the two species involved, homogeneous if they are in the same phase and heterogeneous if not. Homogeneous catalysts, such as dissolved metal complexes or miscible solutions, are considered relatively easier to design and study due to the largely unambiguous nature of isolated $A \rightarrow B$ reactions; scientists can design or choose catalysts which promote only the intended reaction pathway, increasing the "selectivity" of the catalyst. (1) Heterogeneous catalysts on the other hand, such as metal or metal oxide surfaces, thin films, and supported clusters, are primarily chemically active at the phase boundary where adsorption and interaction can take place. Compared to the batch reactors and complex separation processes that many homogeneous catalysts require, the immiscibility of the heterogeneous catalyst provides simple separation and the catalyst is well-suited for continuous reactors. Given that the chemistry of heterogeneous catalysis is generally limited to the surface area of the interphase, using thin films and smaller particles with a higher surface-to-volume ratio can increase the density of active sites while exploiting size-induced effects such as quantum confinement, Schottky junctions, and the devolution of other emergent phenomena.

Although some early breakthroughs in ultra-small, supported catalysts such as the catalytic converter grabbed the interest of industry, researchers soon learned that kinetic studies alone were not enough to characterize materials with such small features. As improved synthesis and UHV characterization techniques have provided new means to study model heterogeneous systems, the potential for driven development of synthetic nanomaterial catalysts is being realized. The expanding demand for better catalysts has invariably led to exploration of the nanometer size range, where features compromised of relatively few atoms are used for their size-induced effects, and their small size provides an opportunity for tunability that until now only homogenous catalysts could provide. While early work has extensively characterized the activity of thin metal and oxide films, systems consisting of clusters dispersed on a prepared surface are a relatively new topic of investigation.

An important aspect in understanding and therefore controlling the dispersion of clusters on a surface involves the limiting of their movement on the surface by a variety of means. The two sintering processes that often occur are Ostwald ripening in which atoms and small intermediates evaporate from small clusters and condense onto larger ones, and Smoluchowski ripening in which entire clusters diffuse and aggregate. To avoid sintering processes on a surface, it is important to choose a system with the correct cluster-support affinity, where too weak of an interaction might allow diffusion over the surface or too strong of an interaction could reduce the activity of the catalyst. (1) Unfortunately, there is no absolute trend in this interaction strength, the optimal cluster-support interaction is often non-intuitive and a product of convoluted geometric and electronic effects. Although particle sintering is a chief concern when studying supported clusters, recent work has shown that some metal oxide surfaces as well as Moir films may be good candidates for anchoring dispersed clusters. (2) (3) Similarly, clusters can be immobilized on a surface by reducing the temperature. At liquid nitrogen (LN2) temperatures, clusters will not have the internal energy to move from the first slightly stable location they find.

While vapor deposition and impregnation are often used to deposit thin films and clusters, molecular beam methods are well-suited to synthesize and study size-selected clusters deposited on surfaces *in situ*. In molecular beam systems, abundant amounts of model clusters can be generated in vacuum, filtered by mass, and then deposited onto a prepared surface in a vacuum environment so that they can be studied in isolation. In a vacuum isolated environment, the relative lack of oxygen, water and other reactants allows the scientist to probe the individual interactions of a new material, in this case the surface supported clusters.

Similarly, gas phase molecular beam studies provide an additional avenue to study size- and composition-dependent properties of isolated model cluster systems using electronic and structural changes. Coupled with the surface techniques to characterize the surface-cluster reaction as well as methods to quantify adsorption energies and describe the binding environment, molecular beam experiments provide a comprehensive method to study model cluster systems for heterogeneous catalysis.

References

1. Chemisorption and reactivity on supported clusters and thin films: Towards an understanding of microscopic processing catalysis. **R.M. Lambert, G. Pacchioni.** s.l. : Springer Science & Business Media, 2013, Vol. 331.

2. *Fundamental insight into the substrate-dependent ripening of monodisperse clusters.* **Y. Fukamori, M. Konig, B. Yoon.** 11, s.l. : Chem Cat Chem, 2013, Vol. 5.

3. *Catalytic oxidation of carbon monoxide over transition metal oxides.* **S. Royer, D. Duprez.** 11, s.l. : Chem Cat Chem, 2011, Vol. 3.

4. *Photoemission from mass-selected monodispersed Pt clusters.* **W. Eberhardt, P. Fayet, D. Cox.** 7, s.l. : Phys Rev Lett., 1990, Vol. 64.

5. Learning, Lumen. "General College Chemistry II." *12.7 Catalysis | General College Chemistry II*, courses.lumenlearning.com/suny-mcc-chemistryformajors-2/chapter/catalysis/.

III Molecular Beams and Mass Spectrometry, a Historical Perspective

The study of fundamental physical sciences is intrinsically tied to our ability to harness and measure physical phenomena, that is, instrumentation and technology. Without the development of physical instrumentation to see atomic scale interactions, and the lexicon to go with it, Thomson, Rutherford and others would never have been able to expand the theory of atoms and elements farther than a theoretical understanding which began with the ancient Greeks. Indeed, before the idea of clusters and nanotechnology, before we could imagine investigating the wide range of phenomena these fields would focus on, we had to answer, “what is an atom?”. Thankfully, at the beginning of the 20th century, theoretical atomic models suggested by scientists such as J.J. Thomson and Ernest Rutherford demanded innovations in instrumentation and technology in order to probe the nature of the atom itself. The study of the atomic model was of high concern to scientists at the turn of the century, and through it was born a workhorse of experimental physics, the molecular beam.

> *“Born in leaks, the original sin of vacuum technology, molecular beams are collimated wisps of molecules traversing the chambered void that is their theater […]. On stage for only milliseconds between their entrances and exits, they have captivated an ever growing audience by the variety and range of their repertoire.”*
>
> \- *John B. Fenn*

In one of the first instances of molecular beam experiments, Hans Geiger and Ernest Marsden, at the behest of Ernest Rutherford, used a series of custom instruments, one shown schematically in **Figure III-I**, to measure the deflection of alpha particles passing through a thin gold foil.

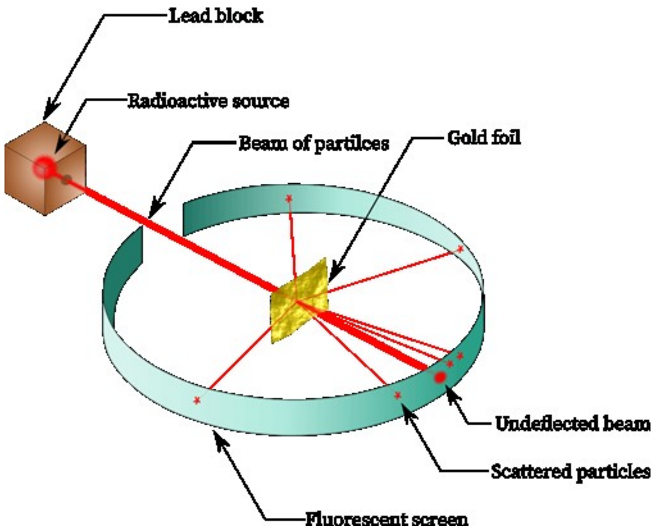

Figure III-I*: Depiction of Ernest Rutherford's gold foil scattering apparatus. (15)*

Rutherford used a radioactive alpha emitter as the source of his molecular beam, a spherical aperture to collimate the beam, and a curved phosphorescent screen to detect the implantation of alpha particles. Finally, after 4 years of instrument improvements and experiments, Rutherford famously revealed to the world in 1911 that the volume of an atom is mostly void, but includes a heavy, small, positively charged nucleus surrounded by light, small negatively charged electrons. (8) With the data taken from this experiment, it took only 5 years for him to construct an instrument to split the first nucleus: a lithium atom, and to further confirm aspects of the nuclear model. The atom was defined; the size, mass, charge and location of its constituents were known, and the modern age of experimental physics had begun.

Understanding the utility of molecular beams for probing the states of atoms and molecules in isolation, it was not long until Otto Stern envisioned, and Walther Gerlach conducted, the famous Stern-Gerlach experiment, which proved to the scientific community that spatial quantization existed. The famous experiment incorrectly attributed the deflection of a neutral beam of molecules by an inhomogeneous magnetic field to the angular momentum from the electron's orbit. Little did they know the silver atoms they used did not have angular momentum themselves, instead it was the angular momentum created by an intrinsic spin of the electron itself, theorized by Uhlenbeck and Goudsmit a few years later, that fully explained the results of the experiment. (9) (10)

Before early chemical physicists could hope to use these innovative molecular beam methods to investigate chemical properties and reactions, early experiments by JJ Thomson demonstrated the need to isolate species of interest. In these early experiments, he incorrectly attributed the mechanism of electricity to protons, H^+, rather than electrons due to hydrogen contamination. It was only with a new research assistant Francis Aston in 1910 that Thomson identified his mistake, and by incidentally creating and identifying heavier ions, realized the true utility of his "positive ray analyzer" as a tool for chemical analysis. Thus the mass spectrometer, the workhorse of chemical analysis through molecular beams, was invented. (11)

III.1 Mass Spectrometry

At its premise, mass spectrometry is a technique that simply involves the segregation of charged particles by their mass-to-charge ratio (*m/z)*, allowing one to not only measure the abundance of different species, as Thomson and Aston did with one of their first mass spectrograph instruments, but also isolate species of interest, for a seemingly infinite number of physical and chemical studies. Because most conventional ionization techniques (notable exceptions include electrospray) result in mostly singly charged species, that is, molecules with only one extra or one fewer electron than their neutral counterpart, i.e., $z = \pm 1$, we assume $m/z = \pm m$, so the mass-to-charge ratio is often used interchangeably with mass when discussing mass spectrometry.

Before Thomson and his student Aston could build the first mass spectrometer, Willhelm Wien independently devised a similar device to measure the velocity, and from that, the *m/z* of the protons that constitute anode rays, or *channel rays* as they were referred to at the time. In Wien's instrument, (**Figure III-II**) ions created by a gas discharge source were all given the same potential energy and collimated by a small aperture, after which they continued through perpendicular homogenous electric and magnetic fields before implanting on a scintillating material for detection. (12)

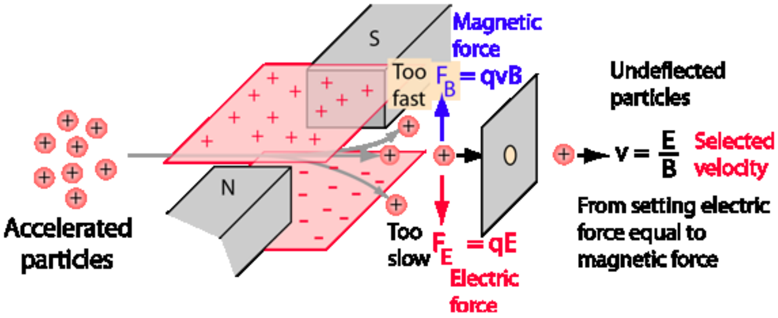

Figure III-II: *The Wein Filter, uses perpendicular electric and magnetic fields to filter ions by velocity. (12)*

In this device, now known as a *Wien Filter*, only ions of a velocity *v* will pass undeflected through the electric field with strength *E* and perpendicular magnetic field *B,* such that

$$v = \frac{E}{B}$$

Equation 4

Knowing that the initial potential energy used to accelerate the ion is converted to kinetic energy, Wien used use the kinetic energy relation $KE = \frac{1}{2}mv^2$ to accurately predict the mass of the proton, although he did not yet understand its significance as one of the subatomic particles. Wien's device suffered from high pressures in the instrument, with collisions between the particles in the beam and gas molecules impeding accurate results.

In Thomson’s version, incoming charged particles are deflected by parallel electric and homogenous fields, deflecting different masses into parabolic trajectories (**Figure III-III**). (13)

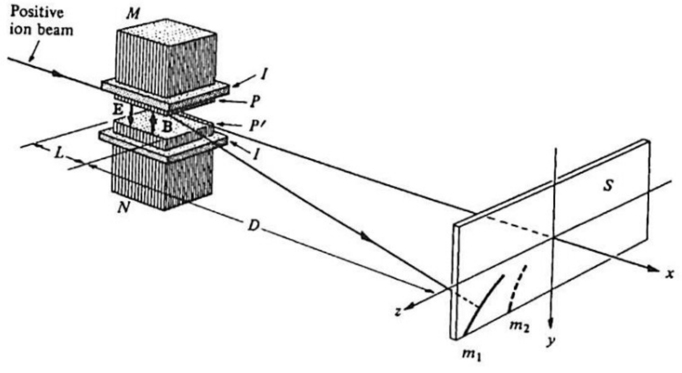

***Figure III-III**: JJ Thomson’s first mass spectrometer. (13)*

While Wien technically beat Thomson to the first mass filter by almost a decade, the lower pressures on Thomson’s instrument, due to his student Aston’s home-made adsorption pump, allowed their results to be correlated, and the importance of a mass filter for molecular beams became plain to the scientific community. (14) This point was well made in a 1913 lecture when Thomson noted this new *“method had several advantages… especially for the detection of new substances”*. (15) While Wien, Thomson and in particular, Aston continued to pave the way for the advancement of mass spectrometry, particularly as it related to nuclear science, an often-overlooked student of Wien’s deserves much credit for developing mass spectrometry as a modern accessible benchtop technique.

III.1.1 Magnetic Sector Mass Spectrometer

After starting out in Wien’s Lab, Arthur Dempster came to finish his PhD in the US at the start of the First World War, where he continued to explore ions and channel rays like he had done with Wien. Dempster’s first instrument was similar to Thomson’s, with parallel electric and magnetic fields, but instead of using an electrical arc discharge like Thomson as the source of his positive rays, used electron emission from a filament to ionize gases, which proved substantially easier to control. This development paved the way for the robust technique known as electron bombardment ionization as a tool to create ions that can then be controlled and manipulated in a molecular beam from an initial sample of gas or volatile liquid. Furthermore, rather than utilize optical detection methods via photosensitive coatings, Dempster chose to use electrical detection, in the form of a faraday cup attached to a rudimentary electrometer to precisely measure current.

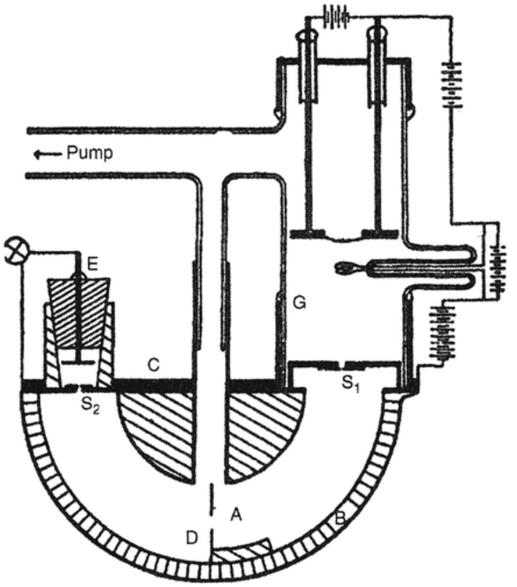

Figure III-IV *Arthur Dempster's first magnetic sector mass spectrometer. (16)*

Dempster's next instrument, he famously used a magnetic field to deflect traveling ions. Shown in **Figure III-IV**, ions are created at the source G, and accelerated towards a slit S_1 to collimate the beam of ions, where they are deflected by a magnetic field with field lines perpendicular to the axis of travel(coming out of the page). (16) According to Hendrik Lorentz, the force *F* acting on a particle with velocity **v** and charge *q* in magnetic field **B** is equal to;

$$F = q(\mathbf{v} \times \mathbf{B})$$

Equation 5

and Dempster could deflect ions around a 180° radius such that only ions with the correct *m/z* would be deflected through the endplate slit S_2 and onto the faraday detector E. Solving this equation gives the operating equation for magnetic sector mass spectrometers that relates *m/z* to the magnetic field strength B, bending radius r, and ion velocity v,

$$\frac{m}{z} = \frac{Ber}{v}$$

Equation 6

The first iteration of his magnetic sector mass analyzer suffered from large velocity distributions of ions created by the source, and therefore poor mass resolution. The operating equations required a constant ion velocity to accurately determine their mass, so Dempster's next model solved this by using Wien's velocity filter to allow only ions of a certain velocity to proceed straight into the inlet slit, increasing the resolution of the analysis. Over the years, Dempster and his students continued to provide improvements, such as additional electrostatic focusing and improved ion sources and detection methods. The second book ever written about mass spectroscopy in 1937 found that a majority of instruments being used were derivative of Dempster's magnetic sector design rather than Thomson and Aston's, probably owing to the fact that Aston did not mentor graduate students, while Dempster mentored many that in turn became behemoths of their field. (17)

The previous cluster deposition instrument used in the Bowen lab incorporated a magnetic sector mass spectrometer. With a 60° bend to isolate ions by their m/z, the old instrument was able to probe extremely high masses, constrained only by the current of the power supply on hand, but suffered from poor resolution.

The field of *Mass Spectrometry* saw its first uses outside of fundamental physics in the Second World War when it was used to determine the purity of fuel in refining processes, and saw rapid application development in the Manhattan project for a number of tasks such as process control, leak isolation and various other nuclear science experiments. The 20th century saw an explosion in instrumentation related to mass spectrometry techniques that cannot all be touched upon in the current text, but the ingenuity required, and the innovation that they spurred, cannot be understated. A final development in mass spectrometry will be considered: the quadrupole mass spectrometer (QMS). The new cluster deposition instrument was built with a quadrupole mass spectrometer in order to improve the mass resolution to a point that would allow one to more easily differentiate between clusters of similar mass.

III.1.2 Quadrupole Mass Spectrometer

In 1953, using recent advances in strong focusing of ions by way of quadrupole fields, Wolfgang Paul and Helmut Steinwedel published a paper describing the first quadrupole mass spectrometer. By applying a combination of AC (V) and DC (U) voltage potentials to four parallel concentric rods, they alternately "squeeze" an ion beam, first in one direction, and then in the other. With the correct ratio of AC to DC voltage, only a single *m/z* can pass through the center of the rods without being ejected from the potential well along the axis of travel **(Figure III-V)**. (18)

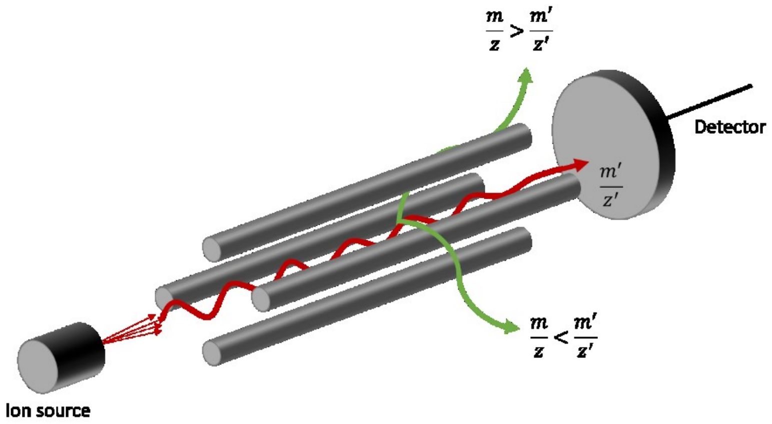

Figure III-V: *QMS diagram, only ions with the correct m/z will have a stable trajectory through the central axis*

In an ideal quadrupole field, the motion of an ion can be described by the differential Mathieu equation,

$$\frac{d^2u}{d\xi^2} + (a_u - 2q_u cos2\xi)u = 0$$

Equation 7

where *u* is the (x,y) displacement, ξ is a dimensionless time variable defined by $\xi = \omega t/2$, ω is the angular frequency of the AC voltage, and r_0 is the inscribed radius of the quadrupole rods. This allows one to define two dimensionless stability parameters,

$$a_x = -a_y = \frac{8eU}{m\omega^2 r_0^2}$$

Equation 8

and

$$q_x = -q_y = \frac{4eV}{m\omega^2 r_0^2}$$

Equation 9

which define a parameter space for possible operating conditions of the quadrupole rods. The solutions of the Mathieu equation, mapped into the *a / q* parameter space, define regions of stability for ions of mass *m*, the lowest voltage stability region is shown in **Figure III-VI**. (19)

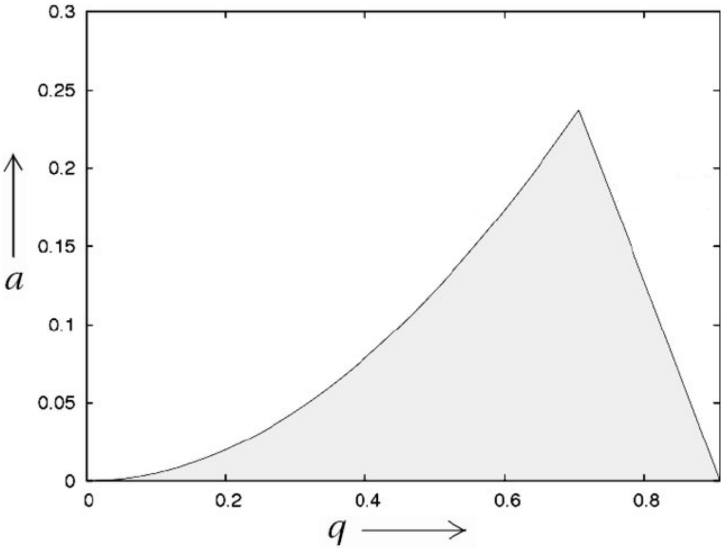

Figure III-VI: Parameter space of a QMS showing lowest voltage stability region. (19)

Since the dimensionless parameter *a* is proportional to the DC voltage, and the parameter *q* proportional to the AC voltage, if *ω* and the voltage ratio U/V are held constant, linearly ramping the voltages causes the system to follow the diagonal line on the plot in (**Figure III-VII**), allowing it to provide a stable trajectory of ions of mass *m* for a period of time. By linearly increasing the RF and DC voltages over a large enough region, the QMS will pass through stability regions for progressively larger and larger masses, allowing them to momentarily have a stable trajectory through the quadrupole rods. (20) A mass spectrum, is then easily generated by placing an ion detector after the QMS and measuring the ion current. By decreasing the slope of the scan line, the abundance of each successive species to pass through the mass spectrometer will increase, but will lose resolution and distance between neighboring peaks (**Figure III-VII)**.

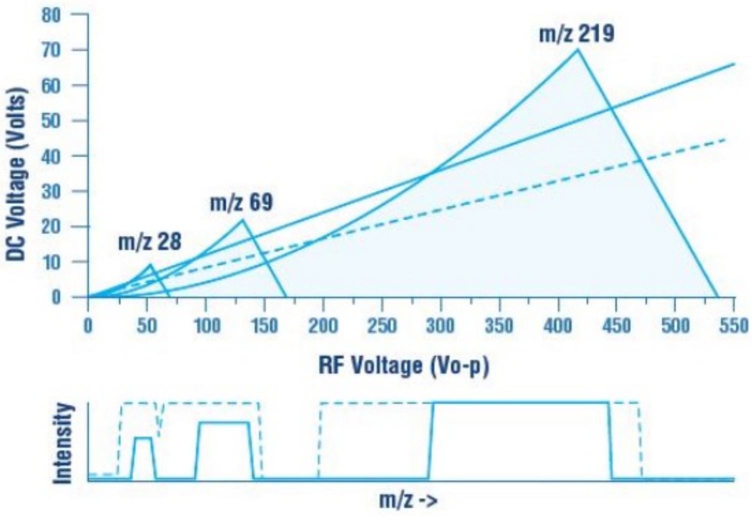

Figure III-VII: *Scan line of a QMS increases linearly, high resolution(solid line) and lower resolution scan line(dotted line). (19)*

Conversely, by increasing the slope, a smaller section of the stability region for each mass is sampled, decreasing the intensity or abundance of ions that pass through the quadrupole field, but increasing the space between neighboring peaks, i.e., better resolving the individual peaks. If the scan line were perfectly straight, it is obvious to see that the higher masses would be less and less resolved. To make up for this, modern QMS controllers will output a scan line +6whose slope increases with mass, giving better quality data.

References

1. The Scattering of alpha and beta particles by Matter and the Structure of the Atom. **Rutherford, E.** s.l. : Philos Mag, 1911, Vol. 21.

2. **Franklin, Allan.** Right Experiment, Wrong Theory: The Stern-Gerlach Experiment. *Standford Encyclopedia of Philosophy.* [Online] 2019. [Cited: 07 20, 2020.] https://plato.stanford.edu/entries/physics-experiment/app5.html.

3. *The Stern-Gerlach Experiment and the Electron Spin.* **Pakvasa, Sandip.** s.l. : arXiv, 2018.

4. *J.J. Thompson's Work on Positive Rays, 1906-1914.* **Falconer, Isobel.** 1988, Historical Studies in the Physical and Biological Sciences, pp. 268-310.

5. *Colloquium: 100 years of mass spectrometry: Perspectives and future trends.* **Simon Maher, Fred Jjunu et al.** s.l. : Reives of Modern Physics, 2015, Vol. 87.

6. *J.J. Thomson - the Centeneary of His Discovery of the Electron and of His Invention of Mass Spectrometry.* **Griffiths, Iwan.** 2-16, s.l. : Rapid Communications in Mass Spectrometry, 1997, Vol. 11.

7. *Development of mass spectrometeres from Thomson and Aston to present.* **Munzenberg, G.** s.l. : International Journal off Mass Spectrometry, 2013, Vols. 349-350.

8. *Rays of positive electricity.* **Thomson, J.J.** s.l. : Royal Society, 1913.

9. *Dempster's Descendants - The core of the develpoment of mass spectrometry.* **Nier, Keith.** 8, s.l. : Journal of Mass Spectrometry, 2019, Vol. 55.

10. *100 years of mass spectrometry: Perspectives and future trends.* **Simon Maher, Fred Jjunju, Stephen Taylor.** Januray-March, s.l. : Reviews of Modern Physics, 2015, Vol. 87.

11. *Benchtop mass spectrometry in clinical biochemistry.* **Honour, John.** 6, s.l. : International Journal of Laboratory Medicine, 2003, Vol. 40.

12. **Extrel CMS, LLC.** Using Graphical Tools to Understand Quadrupole Theory. *AZO Materials.* [Online] May 2014. [Cited: 07 20, 2020.] https://www.azom.com/article.aspx?ArticleID=10996.

13. **Ginsbach, Frank Dunnivant and Jake.** Quadrupole mass filter. *GAS CHROMATOGRAPHY, LIQUID CHROMATOGRAPHY, CAPILLARY ELECTROPHORESIS - MASS SPECTROMETRY.* s.l. : Whitman College, 2011.

14. ChemistryGod. "Rutherford's Gold Foil Experiment ~ ChemistryGod." *ChemistryGod*, ChemistryGod, 31 Dec. 2019, chemistrygod.com/gold-scattering-experiment.

IV Ion Sources for Cluster Beams

The ability to mass select ions of interest from a molecular ion beam means very little if there does not exist an abundant source of the ions. Early experimentalists such as Thomson relied on a high voltage arc between a cathode and anode to create a plasma discharge; a plasma being a hot gas with equal parts negatively and positively charged ions. With this discharge source, a high voltage applied across a gap causes an electrical arc, and ions can either be vaporized from one of the electrodes themselves or created by the ionization of neutral gas molecules in the path of the electric discharge.

The original discovery of the proton, as *channel rays* as described previously, was from the ionization of trace hydrogen gas in the area between the anode and cathode of Goldstein's glow discharge source. In the region of the high current arc, a neutral diatomic hydrogen molecule can be split into separate atoms and lose its electron as a consequence of a collision with fast moving electrons or other ions, leaving behind a positively charged hydrogen nucleus, i.e., a single proton. The lone proton is then accelerated by the potential between the cathode and anode, creating an avalanche of charged particles that are accelerated toward their respective electrode (**Figure IV-I**). (1)

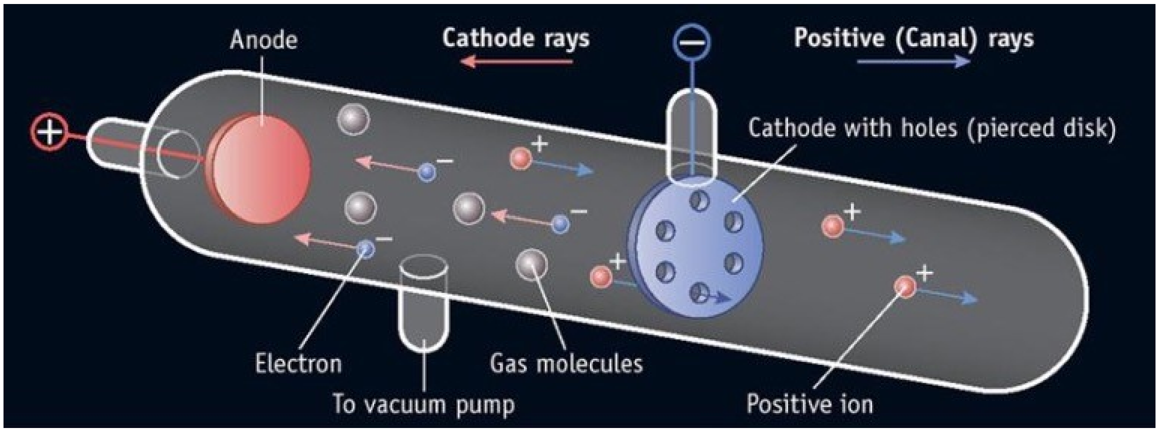

Figure IV-I*: Early cathode ray tube used by Goldstein to discover the proton. (1)*

After drilling holes in the cathode of his discharge tube, Eugen Goldstein observed glowing rays emitting from the holes. These were the positive ions that had been created in the discharge and accelerated toward the plate.

The glow seen in such plasma sources is from exited electronic states of ions, which will decay radiatively to a more stable state by expelling a photon. Using electrostatic deflectors, Goldstein was able to measure the mass of the lightest *channel ray*, which turned out to be the proton, and the first ion source was born. Scientists had discovered how to break down matter into its smallest subdivision, the atom, but chemistry is not limited to interactions with single atoms and molecules, so experimentalists would have to discover how to reverse the trend and condense atoms into as clusters in order to study the emergent phenomena and the size-dependent properties of small clusters. (2)

IV.1 Condensation and Cooling

Cluster ion sources are unique from early ion sources only in the fact that they promote the condensation of ions after the initial vaporization and ionization process. Early ion sources were effusive, they involved the simple expansion of an ion cloud through an orifice from one a chamber to the next chamber which was held at lower pressure. Because early ion sources used a low pressure source for generating ions, and/or a small aperture, such that $D \ll \lambda_0$, where D is the diameter of the orifice, and λ_0 is the mean free path of a gas at initial reservoir pressure P_0, the molecules suffered no collisions with the walls of the aperture and were inherently unchanged on either side of the aperture. Because molecules in an effusive expansion suffer no more collisions than those in the initial reservoir, the velocity distribution of the beam corresponds roughly to the Maxwell-Boltzmann velocity distribution of the reservoir temperature. (3)

By taking advantage of thermodynamic and kinetic processes, cluster ion sources promote aggregation or “condensation” of individual atoms and molecules into larger species. Because “cold” ions are more likely to stick to one another, collisional cooling with an inert carrier gas such as helium or argon is often the first step towards promoting the aggregation of atomic ions into cluster ions. By expanding the hot ions into a room temperature carrier gas at relatively high pressure, ions suffer repeated collisions, losing energy with every collision and leading to the so-called collisional cooling.

A further cooling step often involves the expansion of the ion gas cloud from the high-pressure source chamber into a downstream chamber maintained at a much lower pressure. Without time for the expanding gas to thermally equilibrate with the nozzle walls, and the absence of PV work, the gas expansion can be considered adiabatic, therefore the change in volume results in a loss of internal energy and cools the gas substantially. The precise geometry of the channel that expels the ions is important for controlling the final cooling and clustering process, as well as the velocity distribution of the resulting ion plume. (4)

IV.1.1 Supersonic Expansion

In 1951, looking for a way to produce more intense molecular beams, Kantrowitz and Grey (5) conceived of a nozzle-skimmer set-up that would allow the user to create a supersonic beam of molecules with a much higher ion intensity than previous effusive sources, as well as a much more narrow velocity distribution. Because translational temperature is determined by the width of the molecular velocity distribution and not its position, they also knew that this would result in a very cold molecular beam, although this was not their original intent. They imagined that to create a supersonic expansion source would require a much higher pressure in the source region, necessitating a razor sharp cone called a *skimmer* to prevent off-axis, subsonic ions and gases from passing into the next chamber, as well as higher pumping speeds to lower the pressure and reduce collisions (**Figure IV-II**).

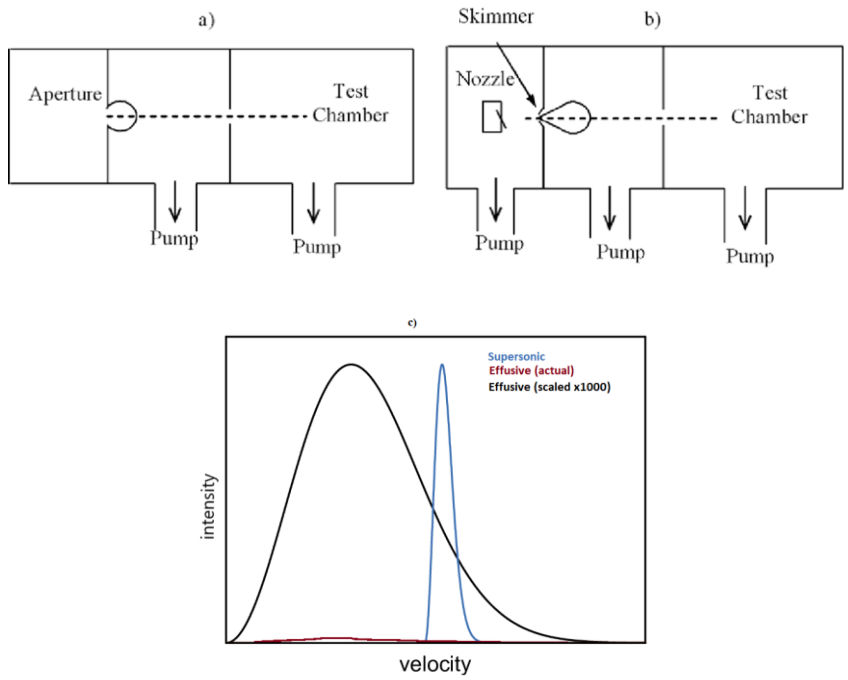

Figure IV-II*: a) Traditional effusive source, limited by pressure in the source chamber. b) Supersonic source using differential pumping and a skimmer to decrease the gas load to downstream chambers. c) Graph showing the velocity distribution from the two types of ion sources. (19)*

In order to maintain a source region at higher pressure while maintaining a suitable downstream pressure that would reduce the likelihood of collisions between beam molecules and remaining gas molecules in the chamber, improvements in high vacuum pumps were required. In 1954 Becker and Bier (6) used powerful diffusion pumps and differential pumping to finally demonstrate the effectiveness of the supersonic source. It was only two years later than Becker and Bier, using this supersonic beam method, observed the first small aggregates of atomic species, i.e., clusters.

The cooling effect from a supersonic expansion happens when the ion/gas mixture is throttled through a nozzle and into a lower pressure region beyond. In an adiabatic expansion, the gas expands but there is no heat transfer between the system and the surroundings. In application, an expansion is adiabatic if there is no time for the system(the gas) and the surrounding(the nozzle walls) to reach a thermal equilibrium, and is an important final tool to direct the condensation of smaller ions. (7) The closer the expansion is to completely adiabatic, i.e., no heat transfer, the more work the system must do and the more translational cooling that results. In a perfect supersonic expansion, all work done to expand the volume of the system comes from internal energy via translation degrees of freedom, and the expanding gas becomes very cold, into the single digit kelvin range. As the gas expands however, individual molecules spread farther apart and undergo fewer collisions, causing the aggregation process to slow down. For this reason, the most adiabatic expansion will produce the coldest clusters but not necessarily the largest clusters. Additionally, if the orifice size is magnitudes larger than the mean free path of molecules at the inlet pressure, which we expect with a high source pressure, there will be many collisions between gas molecules, converting the random atomic motion into directional flow and collimating the expansion while increasing the average velocity.

A supersonic expansion will create regions with different flow characteristics that demonstrate how a skimmer is vital to capture and transport only the cold, dense and collimated interior of the supersonic expansion (**Figure IV-III**). (8)

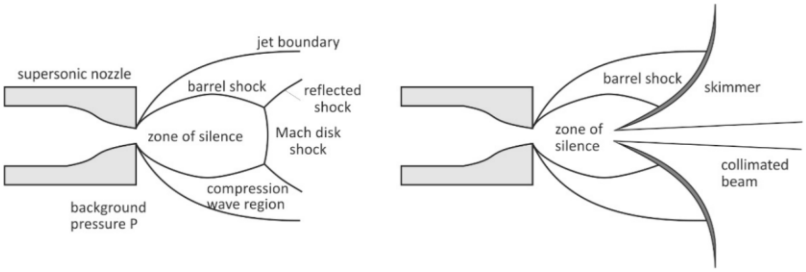

***Figure IV-III**: (left) Dynamic flow regimes directly following a supersonic expansion, (right) proper skimmer placement to transport only the cold interior of the expansion into the molecular beam. (8)*

By placing the nozzle 1-2cm away from the razor-sharp skimmer, it is possible to extract only the center of the so-called “zone of silence” where you have a cold, collimated supersonic expansion.

Similarly, the nozzle geometry itself is important to create a useful range of cluster sizes, and a few important examples are that of the originally designed supersonic or sonic nozzle, the Laval nozzle, and the conical nozzle, all of which use an initial "converging" geometry (**Figure IV-IV**). (4)

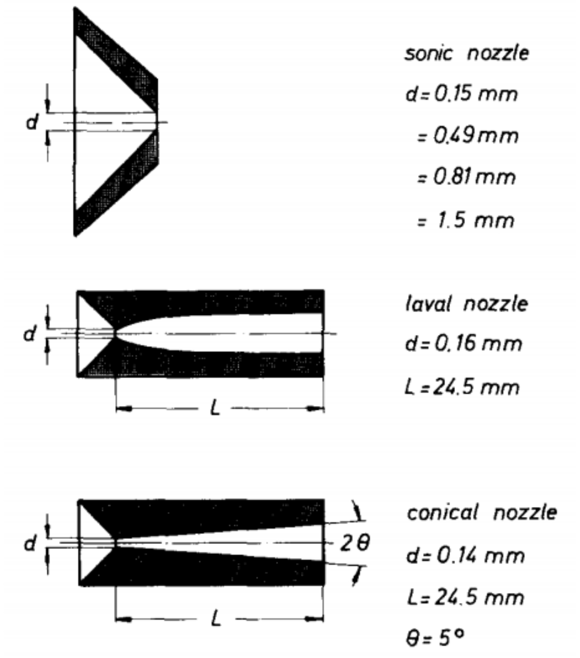

Figure IV-IV: *Nozzle geometries for supersonic expansion. (4)*

As described previously, the pure supersonic nozzle provides the closest equivalent to an adiabatic expansion, cooling the expanding gas/ion cloud the most, but possibly not producing the coolest molecules, nor the ideal angular and velocity distribution. The Laval nozzle incorporates a small orifice that restricts flow, then allows the gas to expand into a lower pressure region on the other side, but not freely like in the sonic nozzle. (9) (10) (11) The sloping walls of the Laval nozzle into a final channel help to direct the translation energy of the expanding gas, collimating it and also providing a brief period where the pressure is still slightly higher than the final region, allowing collisions to continue briefly. Finally, a similar and often more practical solution is that of the conical nozzle, where the faces of the wall after the initial orifice are straight and angled away from the orifice. Being so easy to machine by hand, these are often adequate solutions when promoting clustering. The effect of an outwards sloping channel immediately after the choke point cannot be understated; experiments and simulation confirm the order of magnitude increase in beam intensity downstream along the beam axis, for beams formed with channel openings over the basic pinhole opening. (12) Methodical experimentation has indicated that the optimal angle for conical nozzle openings is 40-60° (full angle).

Following the discovery by Becker, Bier and Henkes of the condensation of atomic beams into small aerosols or “clusters” as they became known, a new field of molecular beam science was ignited as researchers attempted to bridge the divide between macroscopic material properties and those of atoms and molecules. In the Bowen lab, probing this interface between molecules and the bulk has always been one of the driving goals. The new surface deposition instrument was designed with three cluster ion sources in mind, the pulsed arc cluster ion source, the laser vaporization source, and the magnetron sputtering source.

IV.2 Pulsed Arc Cluster Ionization Source (PACIS)

Using a high voltage DC discharge between electrodes like the early glow discharge sources of Goldstein and Thomson, the PACIS source creates cluster ions from a discharge that vaporizes material from the cathode. A DC arc is created between the electrodes, a specially built power supply applies a 20kV pulse to form the initial arc, after which it is turned to a current limiting mode where the current can be manipulated between 1,000 – 5,000A. The vaporized metal atoms are expelled into the gap between the electrodes, where they are ionized by the avalanche of electrons and other charged particles created by the arc, and propelled away by a carrier gas that is intermittently pulsed in to transport the ions out of the source region. The arc and carrier gas timings and the pulse durations are controlled by advanced timing boxes and are precisely manipulated to maximize the creation of ions under different conditions and scenarios.

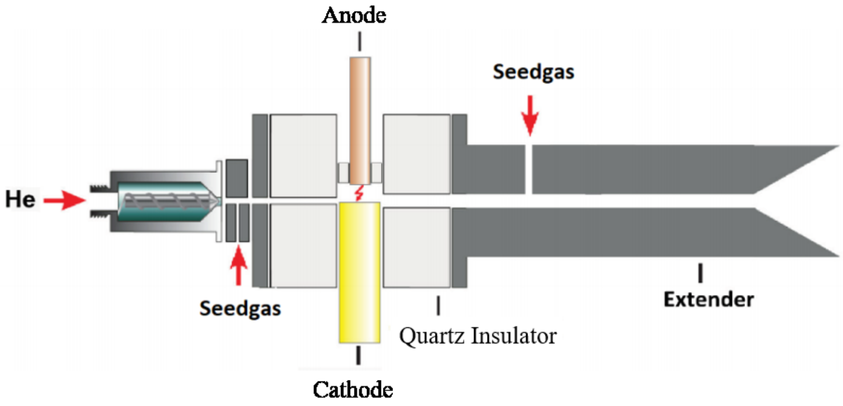

***Figure IV-V**: Diagram of PACIS source. Arc discharge between the high voltage electrodes creates ions which are entrained in a carrier gas and expand through a nozzle into vacuum.*

Shown in **Figure IV-V**, (13) the carrier gas flows through the gap between the electrodes, carrying ions along a channel and farther downstream. A seed gas can also be used to create favorable reaction conditions for certain species, such as hydrogen to promote metal hydride formation, or oxygen for the formation of metal oxides. Like the other sources, the nozzle geometry can be adjusted using different nozzle attachments. As described, the trade-off between cooling, collimation and clustering of an expanding gas/ion beam requires flexibility in geometries if there is any hope to change the aggregation tendencies and achieve a desired cluster distribution.

IV.3 Laser Vaporization Source

In the process of laser vaporization, a.k.a. laser ablation, atoms are removed from a solid as a result of irradiation with a continuous or pulsed laser beam. In 1981, Richard Smalley presented work on a laser vaporization cluster source which forms cold beams of metal clusters via irradiation of a metal with a pulsed high-powered laser. (14) Combined with supersonic nozzle technology, he produced several condensed species and provided a new tool for introducing metals and other species to a molecular beamline.

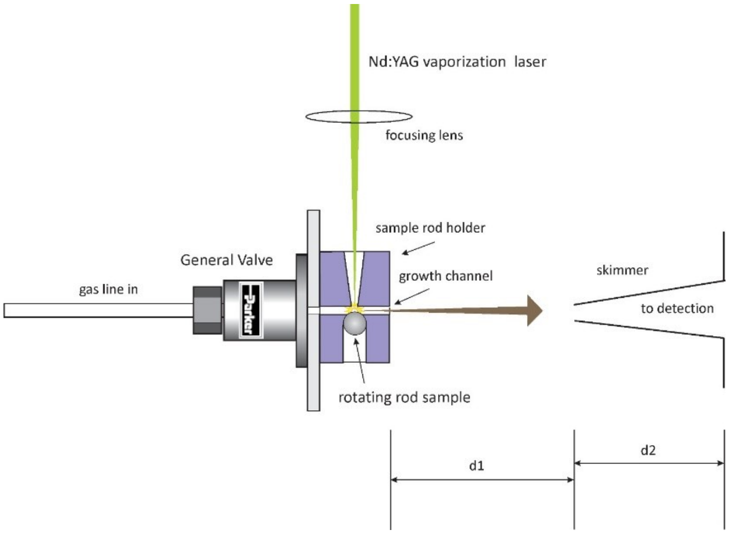

***Figure IV-VI**: Diagram of laser vaporization rod source, the laser hits a fresh place every pulse, generating ions in a carrier gas that are ejected into the vacuum chamber. (16)*

The basic components of the laser vaporization source (**Figure IV-VI)** are a metal rod that is rotated and translated at the same time, a solenoid pulse valve that pulses a carrier gas into the ablation area at regular intervals, a focused laser pulse, a housing which forces the expanding gas/laser ablation cloud into a growth channel before being expelled into vacuum as a supersonic jet, and lastly a skimmer to prevent the off-axis portion of the expanding gas cloud from reaching the next chamber and increasing its pressure. The carrier gas can be chosen from inert gases such as helium and argon, and the pressure and duration of the pulse controlled to modify the condensation process that leads to clusters. The carrier gas can also be seeded with a reactive species such as oxygen, e.g., to create oxides. By both rotating and translating the metal rod along its axis, every laser pulse ablates a fresh piece of metal, whereas ablating the same spot would result in increasingly hotter ions and a decreasing intensity over time.

The laser must be high enough intensity to cause a spark on the metal, which is often accomplished with the second harmonic frequency of a Nd:YAG laser, in our case a DPSS 250 from Innolas (25W, 150Hz, 145mJ). A thin copper plate held at the nozzle entrance can be used as an indication of the laser's focus; once it produces a sizeable spark, then, laser spot paper is used at lower laser power (30Hz & <50mJ) to fine tune the size and shape of the laser spot. The the laser is kept below eye-level and aligned using two mirrors that are oriented at 45° angles to the beam, to direct the beam first up, and then horizontally down the beam axis (**Figure IV-VII**).

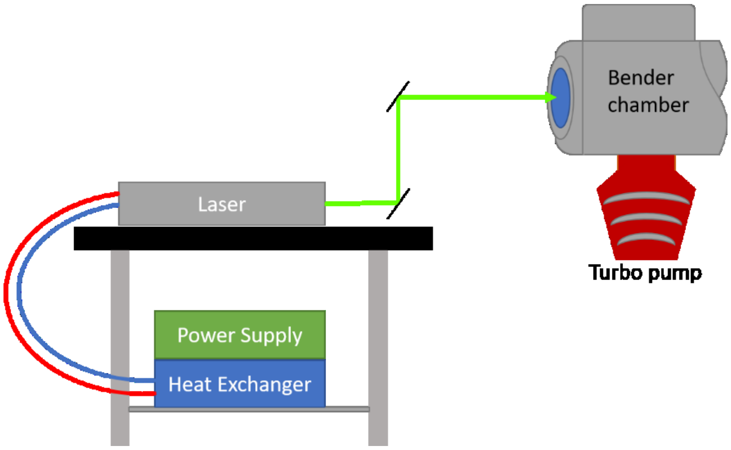

Figure IV-VII: *Depiction of laser setup, two mirrors to align laser into the instrument.*

By iteratively centering the laser spot on each mirror and then in front of the laser vaporization target, one can align the laser with the intended laser vaporization source, and then focus it for the optimal ablation intensity.

IV.3.1 Laser Vaporization Rod Source

One such laser vaporization rod source was recently designed for the surface deposition instrument. Using the experience that the spectroscopy instruments in the Bowen lab have with the laser vaporization technique, it was decided to adapt that source to the surface deposition instrument. A key requirement for the surface deposition instrument is that it must accommodate the existing laser, which is aligned to shoot down the beam axis, parallel and opposite the flow of ions in the beamline. As one might imagine, the limitation is that the denser the vaporization plume, the more the laser beam itself is attenuated before reaching the sample. Any loss in laser power as it passes through the ion cloud will be balanced by a temperature increase in the ions themselves, which is also undesirable. For this reason, high laser repetition rate and power may not always achieve the greatest intensity of ions, even if useful for isolated laser ablation. Other solutions may be possible in the future, such as using optics to bring the laser in from a side window, however the solution to bring the laser in through the beam axis has worked well in some prolific instruments (15) so it will be used initially.

It is often difficult to align all of the different parts of the laser vaporization source with each other, and then with the laser beam, so a laser vaporization experiment table (**Figure IV-VIII**) was conceived that could allow the user to easily install and adjust the parts of the laser vaporization rod source.

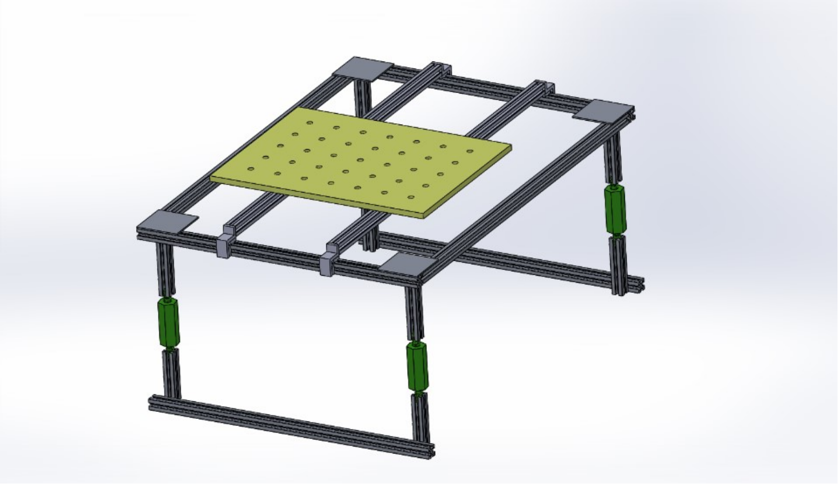

***Figure IV-VIII**: Adjustable stand for LSV source and future adaptions*

This experiment table will sit in the source chamber and uses Teflon bearings slotted into 8020 aluminum extrusions to allow the mounting plate to be moved in the X and Y directions, in principle to align the source with the skimmer or change the source-skimmer distance.

On this plate, ¼-20 tapped holes are arranged in 1” increments and can be used to align different parts of the laser vaporization source with one another. The entire stand can be removed from the source chamber so that the different pieces of the laser vaporization source can be installed. The laser vaporization source parts were machined by hand and are variations of a similar laser vaporization source created by other members of our lab.

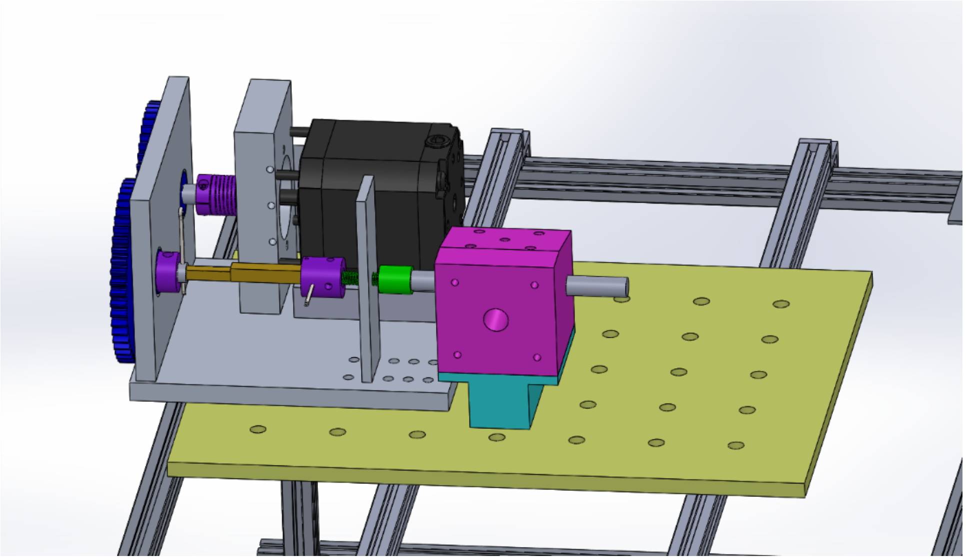

***Figure IV-IX**: View of LSV source without nozzle on adjustable stand*

The motor, shown in black (**Figure IV-IX**), an Arun Microelectronics D42.2, turns a set of gears, shown in blue, which turn a set of nested square brass rods. The brass rods are not attached to each other, the inner one simply rests inside the outer, and turning one will force the other to turn. The larger square brass rod is then attached to a coupling, shown in purple, that holds a 10-32 rod adapter, shown in bright green. This rod adapter, attached to the brass rod via the purple cotter pin shaft coupling, is attached to the end of the target laser vaporization rod, after a long section of 10-32 thread that passed through a tapped hole in the gray post. As the brass rods turn, the green rod adapter is forced to turn, but since it is in a threaded hole, translates, and causes the square brass rods to further recess or pull out of one another. In this way, the laser vaporization rod can be translated and rotated at the same time.

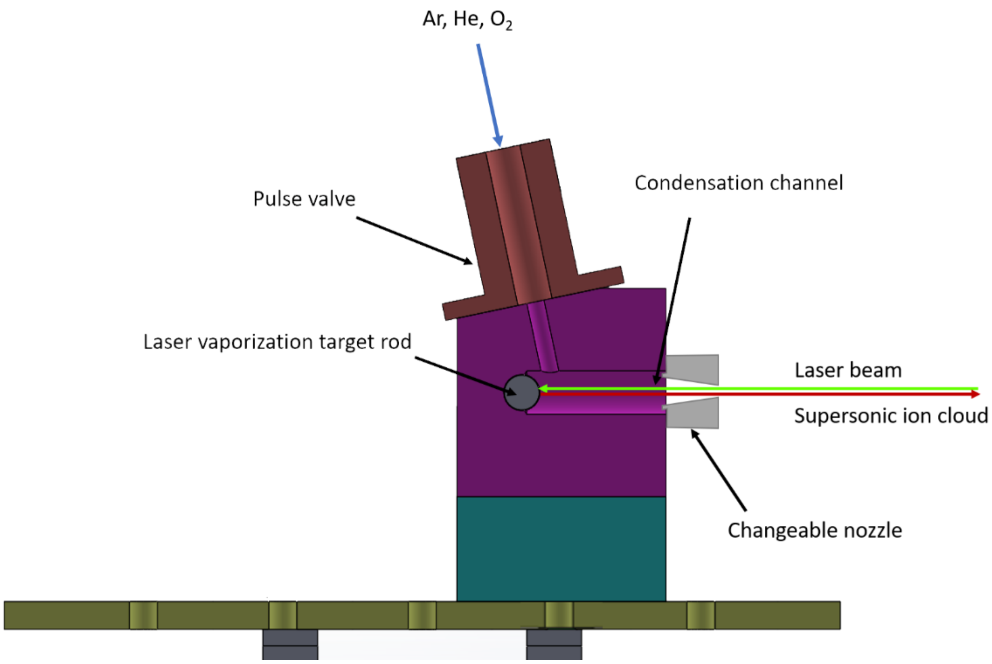

Figure IV-X*: Annotated cut-away of laser-vaporization housing block*

The laser vaporization rod itself then passes through the vaporization housing, shown in a cut-away in **Figure IV-X**. The pulse valve is mounted above and slightly behind the ablation region, with a channel for the initial condensation to occur. The end of the condensation region has a 3/8-16 tapped hole that is used to thread in a nozzle. This way, different nozzle geometries can be explored without changing the rest of the setup. After all these components have been mounted and locked in place with set-screws the stand can be inserted into the source chamber and correctly aligned with the laser and skimmer (**Figure IV-XI**).

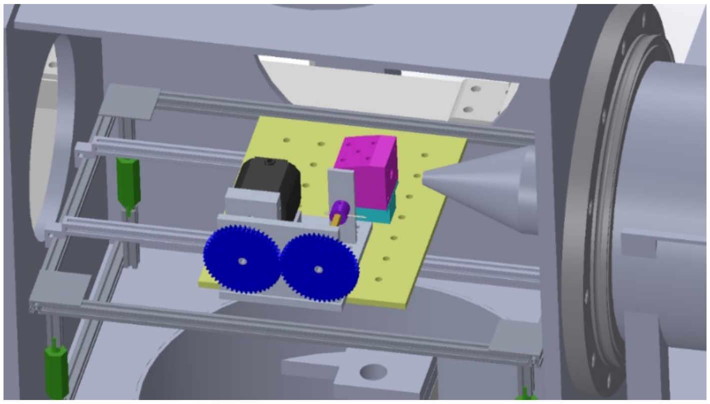

***Figure IV-XI**: 3D view of LVS rod source inside the cluster source chamber, positioned in front of the skimmer*

Once placed in the source chamber, the plate holding the motor, gears and rod housing can be moved around until it is aligned with the laser and has the optimal nozzle-to-skimmer distance via the Teflon bearings. Finally, another setscrew is tightened and the source is fully constrained and aligned with the ablation laser. Work is currently being done to install a chain and stepper motor that will allow the nozzle-to-skimmer distance to be changed while the source chamber is held at vacuum.

IV.3.2 Laser Vaporization Disk Source

Another laser vaporization technique is being developed by our lab that involves the ablation of metal from a thin disk instead of a rod. Because the volume of a rod is mostly trapped on the interior, it is an inefficient source for metal ablation that is limited by clean surface area, and especially costly for precious materials. By ablating a pattern into a thin metal disk, more of the materials volume is exposed, and a higher percentage of it can be ablated before the surface deteriorates with char and oxide buildup. Using a design by Zach Hicks (16), a metal disk is mounted on one of the planetary gears in a planetary gear set-up, allowing the laser spot to ablate fresh surface along a rose petaled pattern with 91 loops before coming back to the starting point (**Figure IV-XII**).

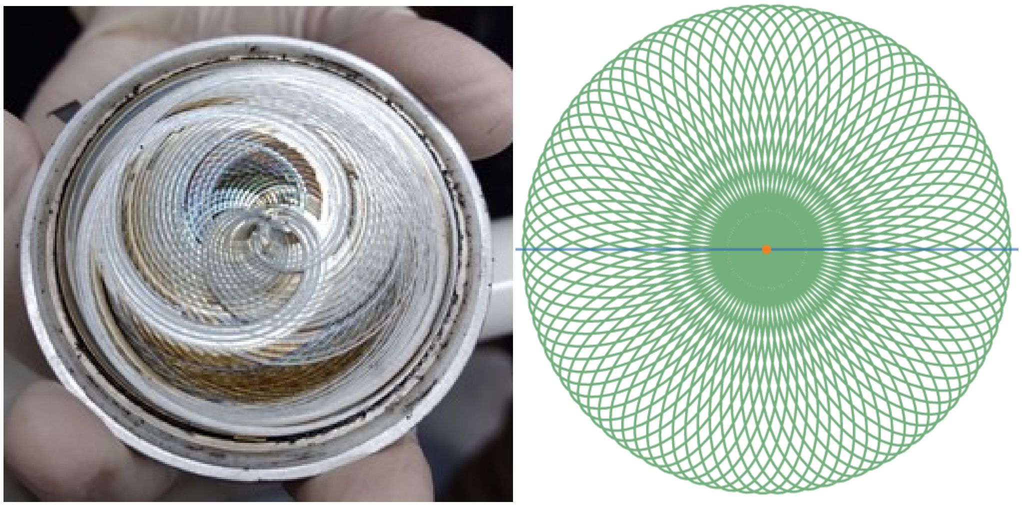

Figure IV-XII*: Design of rose pattern, and the produced laser ablation pattern on a cobalt metal disk*

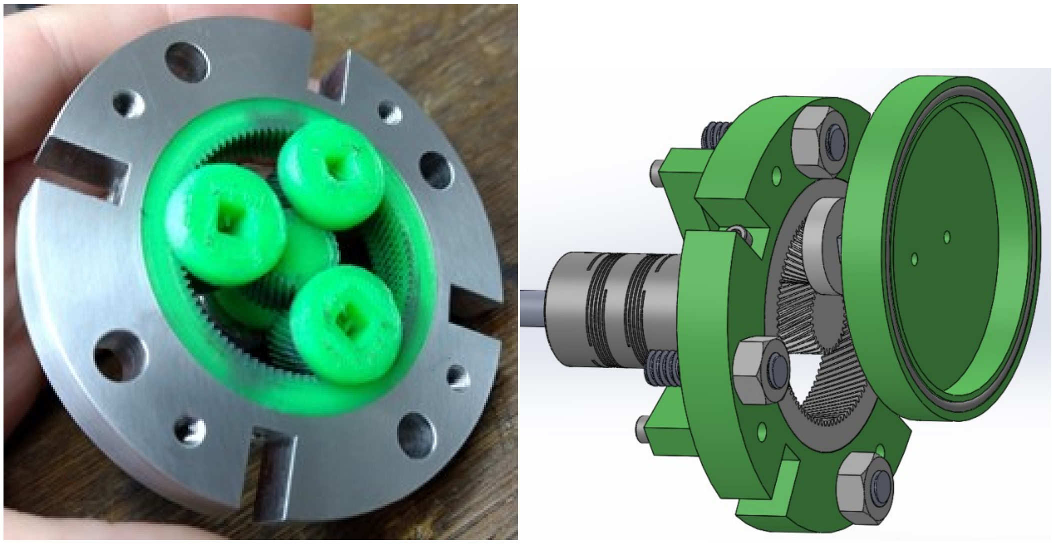

Figure IV-XIII*: Design and application of the planetary gear for the laser vaporization target disk holder*

The thin metal disk that is to be ablated, i.e., the “target”, is inserted into the target holder and held against the laser vaporization housing using a spring (**Figure IV-XIII)**. The laser vaporization housing has a position for the solenoid pulse valve, which injects a burst of gas coinciding with the laser pulse, forcing the expanding ion/gas cloud into the condensation region of a nozzle, before being compressed in the nozzle’s (variable length) throat, and finally being expelled into the vacuum.

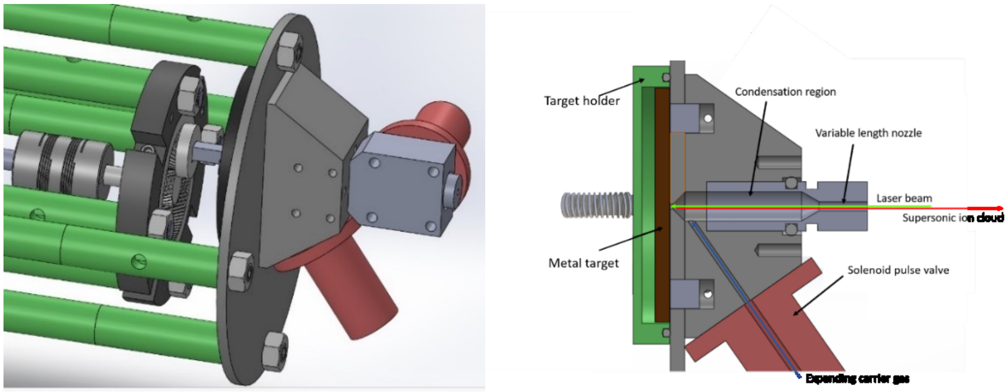

Figure IV-XIV*: 3D view and side view of the laser vaporization disk source housing*

The planetary gears and laser vaporization housing are all mounted on adjustable pegs that extend from the rear of the source chamber. The source was designed with an adjustable condensation region/nozzle geometry in mind. By removing the nozzle, which is held in place by O-rings, the entire nozzle can be switched out, allowing one to change the geometry of the condensation region or the nozzle. Furthermore, a second pulse valve can be attached to an extension, where a seed gas can be added to the expanding ion cloud. Experience with this source has shown that the longer nozzle created the most ion intensity down axis, probably due to a better collimating effect. The seed gas nozzle has not been used yet but could be in the future.

IV.4 DC Magnetron Sputtering Source

Coined at General Electric in the 1920s, the term magnetron describes an ionization technique in which magnetic fields are used to control the motion of ions. As a charged particle, a moving ion will experience a force perpendicular to the magnetic field according to Lorentz's law discussed previously. Early scientists experimented with the orientation of magnetic and electric fields to improve the thermal evaporation of atoms from a surface in low pressure. In 1939 the famous physicist F.M. Penning patented a use of this technique for the deposition of a thin film by a process which he called "cathode disintegration", but we now call sputtering.

(17) This technique catalyzed an explosion in thin film deposition techniques that are now ubiquitous in manufacturing of many consumer products, such as flat panel displays(plasma, LED, OLED), glass technology(photochromic glass, reflective glass), plating and tooling in car manufacturing, as well as many emerging fields. (18)

In one notable configuration by Penning, he positioned magnetron electrodes with a magnetic field perpendicular to the electric field. In Penning's design, ions and electrons accelerating toward the anode or cathode move in helical paths as a result of the Lorentz force produced by the magnetic field acting on a moving charge. The helical paths due to the magnetic field increases the path length of electrons and ions and increases the probability of colliding with and ionizing neutral gas molecules, thus creates a self-sustaining avalanche of ions and electrons moving toward their respective electrode. Via this process of "cathode disintegration", fast moving negative ions created by the cascade of electron collisions collide with the cathode surface and eject ions, electrons and neutrals into space. (17) The negatively charged anions will be quickly accelerated away from the cathode and produce a glowing discharge.

Using a version of this process, called DC magnetron sputtering, a high voltage arc is created between a cathode and anode, a metal target disc is mounted in front of permanent cylindrical magnets, a carrier gas is seeded in, and high intensity metal ions of either polarity can be accelerated away from the often described "ion cannon". One such source was built at the University of Konstanz for Gerd Ganteför and is now used in our surface deposition instrument. A new magnetron head was recently built in Dr. Ganteför's lab and brought over by his student Dominik Hierling, who helped to prepare and test the new magnetron head.

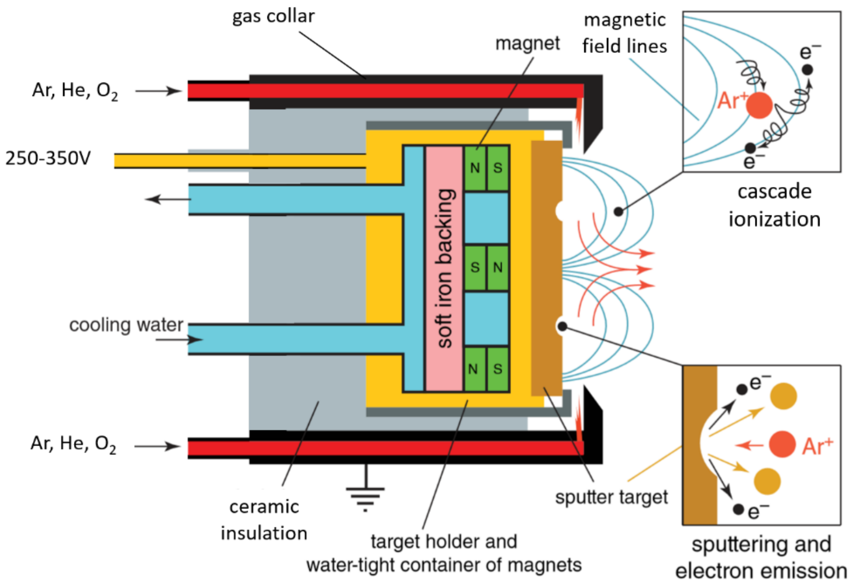

Figure IV-XV *Schematic of the magnetron head. (16)*

In the magnetron head (**Figure IV-XV**), two rings of magnets are placed behind the end of a cylindrical target holder and inside of an empty volume for cooling water to circulate. The sputtering target itself must be a 2" diameter, 0.125" thick, conductive and non-ferromagnetic disk, and is placed in a groove right in front of the magnets. It must be conductive to prevent the surface from building up a static charge due to charge conservation as ions of the opposite charge are sputtered away. Similarly, the target must not be ferromagnetic in order for unpaired electrons in the material to not arrange in a way that attenuates the magnetic field. The rings of magnets produce loops of magnetic fields in a ring around the center of the magnetron head. At some point between the inner and outer magnet, the magnetic field line is roughly perpendicular to the electric field. Similar to the effect first discovered by Penning, helical trajectories of charged particles create a cascade of ions, causing the target to be preferentially sputtered away in a characteristic ring known as a racetrack. A gas collar is retracted over the magnetron head after installing the sputtering target and should be tightened in place when it is as close as possible to the target holder, < 0.1".

A gas containing a combination of argon and helium, as well as a small amount of oxygen if producing metal oxide clusters, is fed into the magnetron head and flow out of small holes from a gas collar. To initiate the sputtering process, a high voltage, 400-500V is applied to the magnetron head, which is kept electrically isolated from the support structure and gas collar by a ceramic piece, generating an arc that initiates the ionization of neutral Argon molecules to Ar^+ and e^-. These are accelerated by the electric and magnetic fields, creating the cascade of charged particles that sputter the target disk and eject oppositely charged ions such as metals and metal oxides M^- and MO^-. Once the arc has been created, it can be maintained with a relatively lower voltage(250-350V) and a current of 150-350mA. The current is a sum of the closed loop current created by the arc as well as the current created by loss of positively charged species from the sputtering target. The current seems to have the most effect on cluster generation, so it is often most convenient to set the magnetron power supply to constant current, allowing it to manipulate the voltage accordingly. Once the oxide coating has been sputtered off the target, the voltage required to maintain the arc is usually relatively stable. If the voltage is unstable, it is best to increase the current set-point temporarily in order to “burn off” any oxide or material inconsistency that is causing the voltage variation. Adjusting the partial pressures of argon, helium, and oxygen can have a substantial effect on the cluster distribution, intensity, and magnetron voltage required to maintain a certain current.

References

1. **McKenzie, Mr.** *Atomic Theory.*

2. *The history of nuclidic masses and of their evaluation.* **Audi, G.** s.l. : International Journal off Mass Spectrometry, 2006.

3. *Nucleation and growth of clusters in expanding nozzle flows.* **Hagena, Otto.** 1-3, s.l. : Surface Science, 2020, Vol. 106.

4. *Cluster formation in expanding supersonic jets: effect of pressure, temperature, nozzle size, and test gas.* **O.F. Hagena, W. Obert.** 1793, s.l. : J Chem Physs, 1972, Vol. 56.

5. **Anderson, J.B., R. P. Andres, and J. B. Fenn.** Molecular Beams. [book auth.] Ross J. *Molecular Beams.* 1966.

6. *Die Erzeugung eines intensiven, teilweise monochromatisierten Wasserstoff-Molekularstrahles mit einer Laval-Düse.* **Bier, E.W. Becker and K.** 11, s.l. : Zeitschrift für Naturforschung A, 1954, Vol. 9.

7. *Molecular Optical Spectroscopy with Supersonic Beams and Jets.* **Richard Smalley, Lennard Wharton, Donald Levy.** s.l. : Accounts of Chemical Research, 1977, Vol. 10.4.

8. **Tseng, Chien-Ming.** *Molecular science using VUV FEL.* s.l. : Department of Applied Chemistry, National Chiao Tung University, 2019.

9. *Homogeneous nucleation of sulfur hexafluoride clusters in Laval nozzle molecular beams.* **Abraham Oommen, Kim Sang-Soo, Gilbert Stein.** 402, s.l. : Jouranl of Chemical Physics, 1981, Vol. 75.

10. *Gasdynamics of very small Laval nozzles.* **Oomen Abraham, Jack Binn, Barry DeBoer, Gilvert Stien.** 1017, s.l. : American Institute of Physics, 1981, Vol. 24.

11. *Nucleation and growth of clusters in expanding nozzle flows.* **Hagena, Otto.** s.l. : Surface Science, 1981, Vol. 106.

12. *Generation and Propagaion of Intense Supersonic Beams.* **K. Luria, W. Christen, and U. Even.** 115, s.l. : Journal of Physical Chemistry A, 2011, Vol. A.

13. *Pure metal and metal-doped rare-gas clusters grown in a pulsed ARC cluster ion source.* **Gantefor, Gerd.** 1990, s.l. : Chemical Physics Letters, Vol. 165.4.

14. *Laser production of supersonic metal cluster beams.* **T.G. Dietz, M.A. Duncan, D.E. Powers, R.E. Smalley.** 6511, s.l. : Journal of Chemical Physics, 1981, Vol. 74.

15. *Photoelectron spectroscopy of size-selected transition metal clusters: Fen-, n=3-24.* **Wang, Lai-Sheng.** 6987, s.l. : Journal of Chemical Physics, 1995, Vol. 93.

16. **Hicks, Zack.** *Design and Construction of Molecular Beamline for Cluster Catalysis Studies.* Baltimore : s.n., 2019.

17. *A Short History: Magnetron Sputter Deposition.* **Mattox, Donald.** s.l. : SVC Bulletin, 2015.

18. **Han, Jeon.** Magnetron Sputtering Technology. [Online] [Cited: July 6, 2020.] https://www.ispc-conference.org/ispcdocs/ispc18/ispc18/content/slide00822.pdf.

19. O'Brien, Kerry. “DigiVac Training for Customers.” *SlideShare*, 7 Oct. 2016, www.slideshare.net/KerryOBrien16/digivac-training-for-customers-66872427.

V Ion Transport System

In concert with the development of ion sources and mass spectrometers were the systems that allow the experimentalist to physically extract a collimated ion beam from its source and transport the beam of ions to the intended probe technique. Ion transport techniques allow the experimentalist to manipulate the cross section, speed and other characteristics of the molecular beam as it travels through vacuum chambers. Ion transport systems fall generally into two categories, electrostatic optics such as lenses or the quadrupole bender, which apply a controllable but constant voltage in order to accelerate ions toward conductive pieces with applied voltage, and RF multipoles which apply alternating currents to focus a beam in devices called ion traps, funnels, and guides.

In the cluster deposition system, a few sources are used to create ions that are intended for deposition on a prepared surface. In order to transport these ions to the prepared surface, several electrostatic optics and multi-pole ion guides are employed and allow the operator to gently guide the ions down the beamline and "soft land" them onto the surface. In order to prevent ions from being implanted into the prepared surface or from bouncing off entirely, it is important that they be soft landed, i.e. their kinetic energy when reaching the deposition target must be lower than ~25eV per atom.

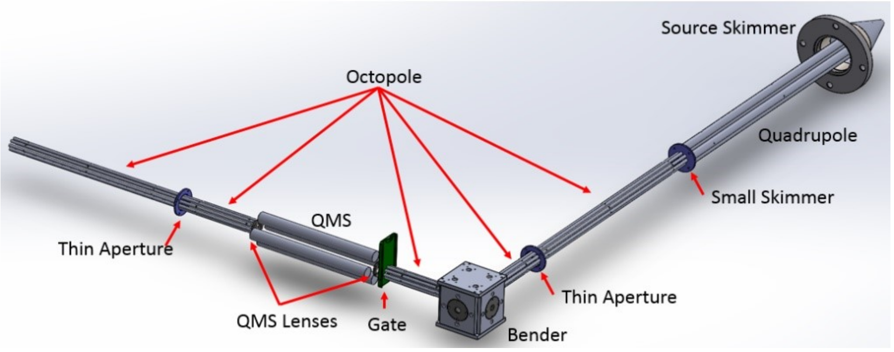

Figure V-I: *3D model of naked ion optics for cluster deposition beamline*

The ion optics of the cluster deposition system are shown in **Figure V-I** and will discussed in depth afterwards. Generally, the ion guides are used to transport the beam through a chamber without change to its on-axis kinetic energy, while the electrostatic optics are used to accelerate, decelerate, focus, deflect and otherwise change the characteristics of an ion beam. The ion guides will be discussed first, and then the electrostatic optics in sequential order down the beamline, while the lenses that are part of the QMS system will be discussed independently with the QMS.

V.1 Ion Guides

Multipole ion guides are used to focus and transport ions through a vacuum chamber. There are several reasons that it is impossible to maintain the collimation of ions through a vacuum without an applied field to focus or guide them. Protruding fields, such as electric fringe fields from nearby electrodes or simply the earth's magnetic field, will cause slight deflections in the travel of moving ions. Another important source of beam divergence is any transverse kinetic energy not lost in the initial gas expansion remains and causes beam expansion. A final main cause of beam divergence is that like charges will repel, causing ions in the beam to feel a repulsive force from one another known as "space charge".

The total kinetic energy of a beam can be described by Equation 10, where the on-axis beam kinetic energy E_{axis} is maintained by lenses, and the idea is to minimize the off transverse kinetic energy of the beam $E_{transverse}$ and prevent beam divergence using multipole guides. Because beam optics and therefore the beam itself is generally cylindrical, it is often useful to refer to it in polar coordinates, where the radial component is equivalent to the afore-mentioned transverse component.

$$E_{total} = E_{axis} + E_{transverse} = E_z + E_r$$

Equation 10

Compared to traditional electrostatic lenses which can be used to focus the beam from an image to an object, the multipole ion guide increases transmission and ease of use. Analogous to the quadrupole mass spectrometer shown before, a multipole ion guide is composed of an even number cylindrical or hyperbolic rods arranged around a central axis (**Figure V-II**), such as quadrupole, hexupole, octupole and so on.

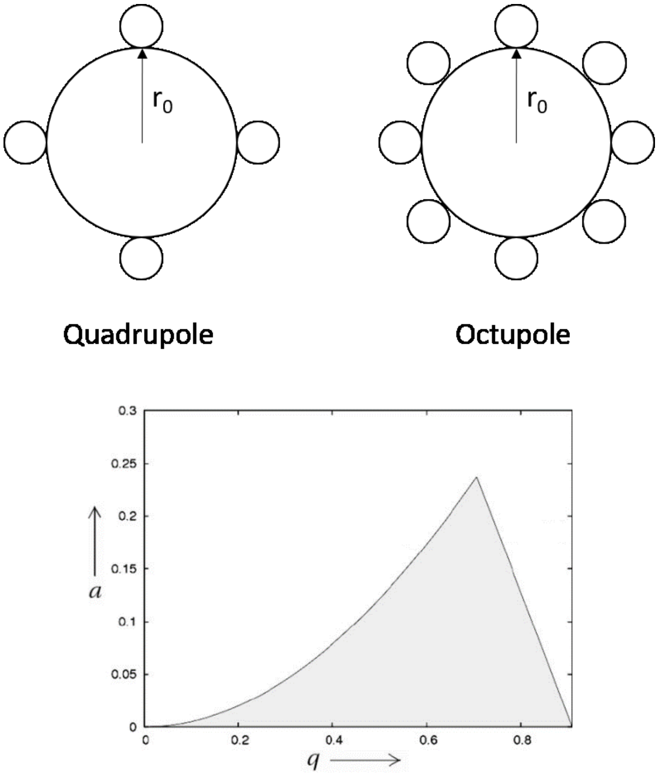

***Figure V-II**: Multipoles (left) and stability region defined by Mathieu equation (right) (3)*

Taking a look at the stability region (**Figure V-II**) and operating equations (Equation 7, Equation 8, Equation 9) for the quadrupole mass spectrometer, we can see that if $U = 0$, then $a = 0$, and any ion with a stability parameter $q < 0.905$ will have a stable trajectory through the quadrupole field. That is, if there is no DC component to the oscillating voltages applied to the quadrupole rods and it is operated in "RF only" mode, the multipole rods act as a high pass filter, letting ions with a mass m pass down the center axis undeflected. Rearranging the definition of q we can find the low mass cutoff m where:

$$m > \frac{k_H \cdot V}{r_0^2 \cdot f^2}$$

Equation 11

and $k_H = 1.0801 \cdot 10^7\ A \cdot s \cdot kg^{-1}$ is a constant. By making the frequency f of the applied voltage sufficiently high, in the so-called radio frequency (RF) range, the multi-pole ion guide can be made to transport all relevant atomic masses. (1) The alternating voltages applied to rod pairs (**Figure V-III**) essentially squeezes the ions between alternating pairs of rod electrodes, causing ions to take a helical path down the beam axis (**Figure V-IV**), and leaving the on-axis kinetic energy unchanged.

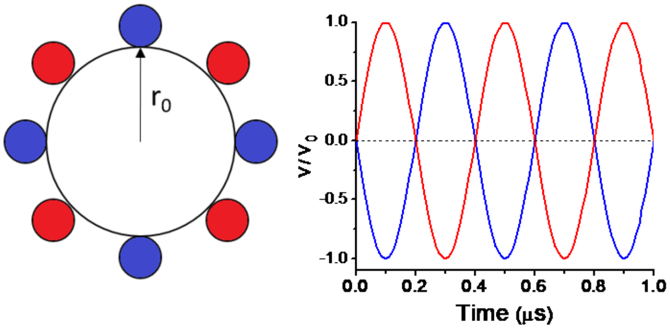

***Figure V-III**: Octupole ion guide and applied voltages*

The multipole field generated by the alternating voltages induces a restoring force that pushes ions toward the central guide axis and can be averaged over time to produce an "effective mathematical potential". The effective potential (Equation 12) for any multipole with 2N electrodes can accurately model the average radial force felt by ions within the RF field, therefore is proportional to the amount that ions will spread out as they travel down the central guide axis. (2)

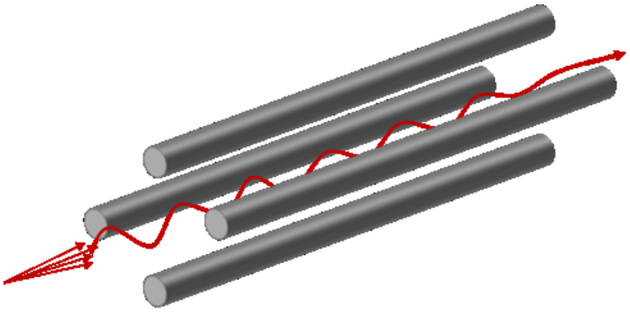

***Figure V-IV**: Illustration of a multipole ion guide in application*

$$V_{eff}(r) = V_0 \left(\frac{r}{r_0}\right)^{2N-2}$$

Equation 12

The effective potential is plotted for multipoles (**Figure V-V**) with a given number of rod electrodes N and inscribed radius r_0, depicting how the higher number of rod electrodes directly leads inducing a relatively weaker restoring force and having a wider beam diameter, all else being equal. For instance, as you move outward radially from the central axis to the inscribed radius r_0, the effective potential for the lower order multipoles rises quicker than those of higher order multipoles. This means an ion in an octupole at a radial position of $0.8r_0$ will feel about 30% of the maximum restoring force. But in a quadrupole, the same ion at $0.8r_0$ would feel about 60% of the maximum restoring force, causing ions in a quadrupole to be much more quickly collimated around the central axis than in comparatively higher order fields. (3)

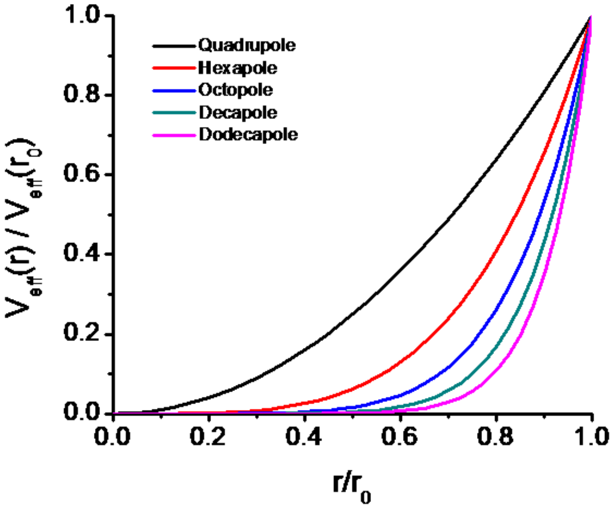

***Figure V-V**: Effective potentials plotted for several order multipole ion guides. (5)*

The fact that different multipole guides will lead to different beam diameters leads to the use of quadrupolar fields specifically for situations where ions are entering with a relatively large amount of off-axis kinetic energy, $E_{transverse}$, such as from the cluster ion source. By forcing ions with excess $E_{transverse}$ into a tight beam, they are forced to suffer scattering collisions with one another that quickly reduce their off-axis energy. By removing the transverse energy associated with the ion beam, the quadrupole is said to produce collisional focusing. This manifestation is illustrated via a SIMION simulation in which an initially dispersed beam enters a quadrupole field and due to collisions and a stronger effective potential, is focused to a small beam diameter (**Figure V-VI**).

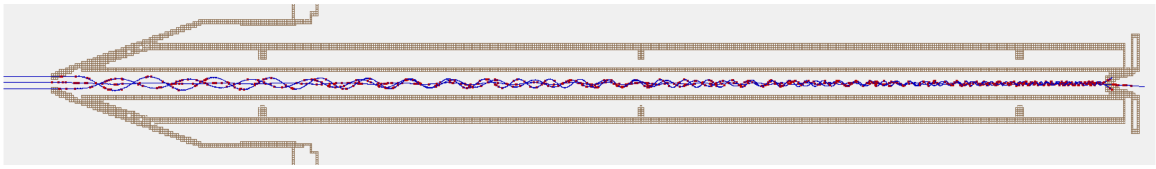

***Figure V-VI**: Simulation of ions collisional focusing due to the large effective potential of the quadrupole field*

Taking advantage of this "collisional focusing" phenomenon of lower order multipoles, the cluster deposition instrument was designed with a quadrupole in chamber 1 directly following the cluster ion source, and octupoles were used in the subsequent chambers to guide the beam once its excess $E_{transverse}$ had been removed. (4)

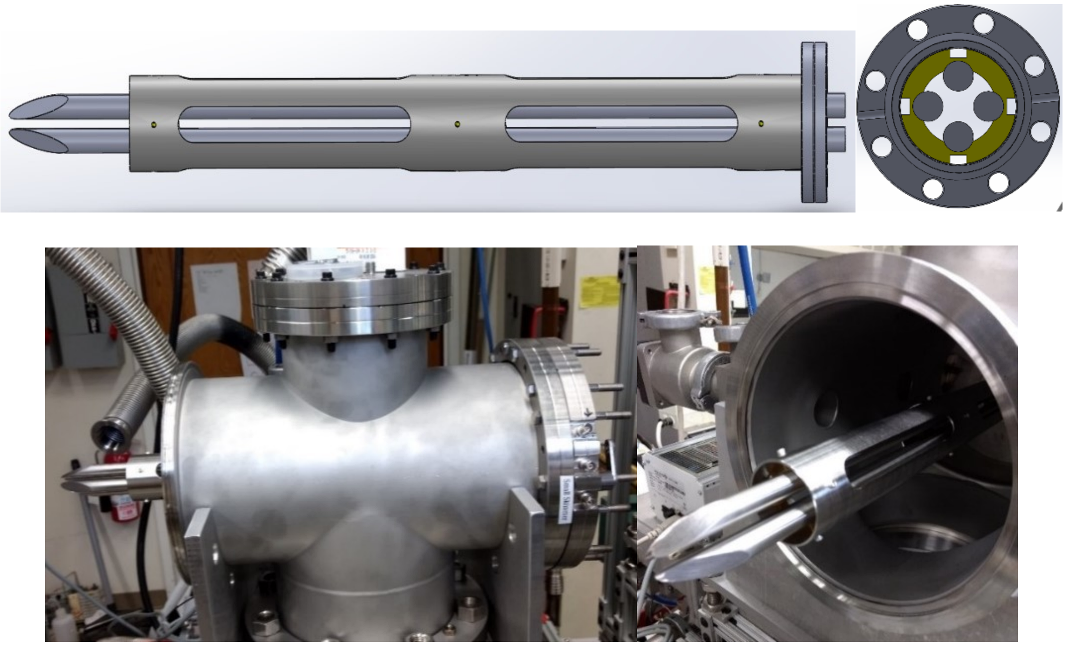

Figure V-VII: *Flange mounted multipole ion guide (top) shown mounted in chamber (bottom)*

All the multipole guides are flange mounted to hold the rods straight inside the vacuum chamber and are held in place by retaining rings within a metal shroud used to block out any fringe-fields (**Figure V-VII**).

There is a separate steel retaining ring for each set of rod pairs, and the two retaining rings are held in place inside of the shroud by a holder made from Ultem. Three of these raining ring sets are fit along the length of the shroud so that the rods are held to their exact inscribed radius the entire length. The quadrupole electrodes are 0.5" OD cylindrical rods with an inscribed radius of 0.25". The end of the quadrupole shroud ends with a 3.375" CF flange that is bolted to a blind tapped bolt pattern on the far side of chamber 1.

Following the quadrupole ion guide in chamber 1, there are five octupole ion guides arranged down the remainder of the beamline in order to effectively transport the cluster ion beam to the QMS where a species of interest is mass selected, and then to the prepared surface to be soft landed. These octupoles are of different overall lengths but are all made from 3/16" rods with an inscribed radius of 9/32" and mounted with similar retaining rings that bolt to every other rod, held by Ultem spacers inside of 316 steel shrouds (**Figure V-VIII**).

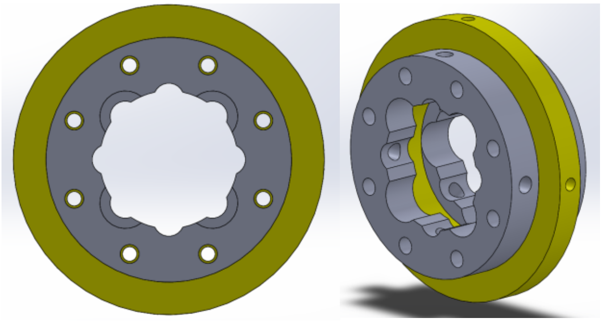

***Figure V-VIII**: Retaining ring for a hexupole ion guide*

Each flange between neighboring chambers has medium high voltage (MHV) electrical feedthroughs to apply the correct RF voltage to each set of multipole electrodes as well as a DC voltage to the aperture between the chambers. The design and details of the multipole ion guides used are discussed in greater detail in the thesis of Zach Hicks. (5)

V.2 Electrostatic Optics

V.2.1 Electrostatic Aperture

The first optic of the beamline is a special type of electrostatic aperture that was discussed previously, the source skimmer. The electrostatic aperture fundamentally consists of a small circular hole in a conductive plate, with electric field lines applied perpendicular to the plate. An aperture often serves to limit off-axis ions from passing into the next vacuum chamber and can be used to accelerate or decelerate the ion depending on the applied voltage. The aperture is arguably the simplest of electrostatic optics and is depicted in (**Figure V-IX**).

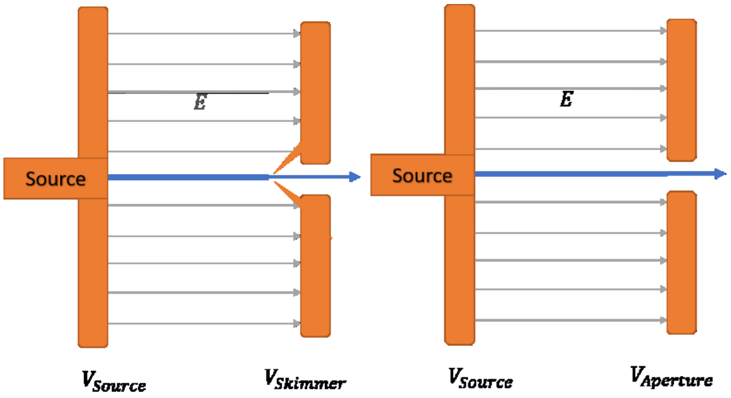

Figure V-IX: *Electrostatic aperture in skimmer geometry(left) and normal aperture (right) depending on the pressure*

In a higher pressure setting that more closely approaches a viscous flow regime, such as in the source chamber, the razor-sharp cone is necessary to prevent turbulence that will affect the beam quality, however as the pressure is reduced in subsequent chambers and the flow regime approaches molecular flow, hydrodynamic considerations become insignificant and a simple hole in a conductive plate will accomplish the same effect. The flow regime is defined by the dimensionless quantity known as the *Knudsen number,*

$$Kn = \frac{\bar{l}}{d}$$

Equation 13

where $\bar{l}$ is the mean free path and d is the diameter of the flow channel. In general, viscous flow occurs in low vacuum settings with Kn < 0.01, Knudsen flow occurs in medium vacuum situations with a range of 0.01 < Kn < 0.5, and molecular flow occurs in high/ultra-high vacuum when Kn > 0.5.

For supersonic jet expansions and beams at higher pressures, diagram of the hydrodynamic regions created by a supersonic jet illustrates (**Figure IV-III)** why a skimmer is sometimes necessary to preserve the collimated beam.

Several apertures and skimmers are used along the course of the beamline to tune the kinetic energy and provide the most stable path to the deposition target.

The skimmer mentioned previously is a type of aperture in which the prescribed geometry is important for differential pumping and beam quality. An ion beam born at a source voltage V_{source} and accelerated toward an aperture with an applied voltage $V_{aperture}$ will generate a beam of ions which leaves the aperture with kinetic energy given by

$$KE = q\left(V_{source} - V_{aperture}\right)$$

Equation 14

The first optic, known as the source skimmer, is mounted via an ISO63 bolt-pattern to an ISO200 double sided flange which bolts to chamber 1 with K type ISO clamps (**Figure V-X**).

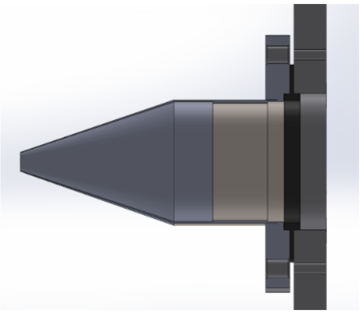

Figure V-X: *Source skimmer*

The cone has a 19° angle and a 1cm OD opening, a spacer made of Delrin is used to keep the skimmer from touching the grounded ISO200 flange. Home-made Teflon washers and screw insulation are used to keep the skimmer electrically isolated so that a voltage can be applied to it.

By wrapping a bare copper wire between one of the skimmer mounting screws and its Teflon washer, one can apply a controlled voltage to the optic. Parts in the source chamber especially will oxidize and become dirty from plasma ejecta so periodical cleaning of the electrical points of contact as well as the surfaces of optics such as the skimmer with an abrasive material such as Scotch-brite, is necessary. It is important not to gouge the optic while cleaning or handling and possibly introduce electric fringe fields, however slight.

Following the source skimmer, there is are several more apertures along the ion transport system. Specifically, there is a small skimmer mounted between chamber 1 and chamber 2, and thin apertures without conical features between chamber 2 and the bender chamber, as well as between the QMS chamber and deposition chamber. The small skimmer and thin aperture (**Figure V-XI)** mount to electrically isolated conductive plates on the end of their respective chamber, so that voltage can be applied, similar to the skimmer, to accelerate or decelerate the ion beam as it moves down the beamline.

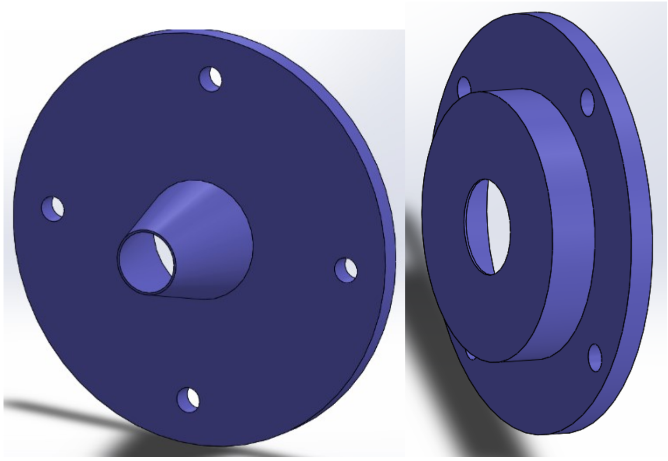

Figure V-XI *Small skimmer (left) and thin aperture (right)*

V.2.2 Electrostatic Quadrupole Bender

Most ion sources will produce an initially hot plasma with negatively and positively charged ions as well as neutral atoms and molecules. The electrostatic extraction voltages felt by the ions will cause only the ions with desired charge to be accelerated down the beamline, leaving many neutral molecules created in the source travelling down the beam axis largely undisturbed by collisions or electric fields. In order to filter out these neutrals, a bend in the beam axis is often utilized. As shown again in (**Figure V-XII**), the ion beam is guided through a 90° electrostatic quadrupole bender.

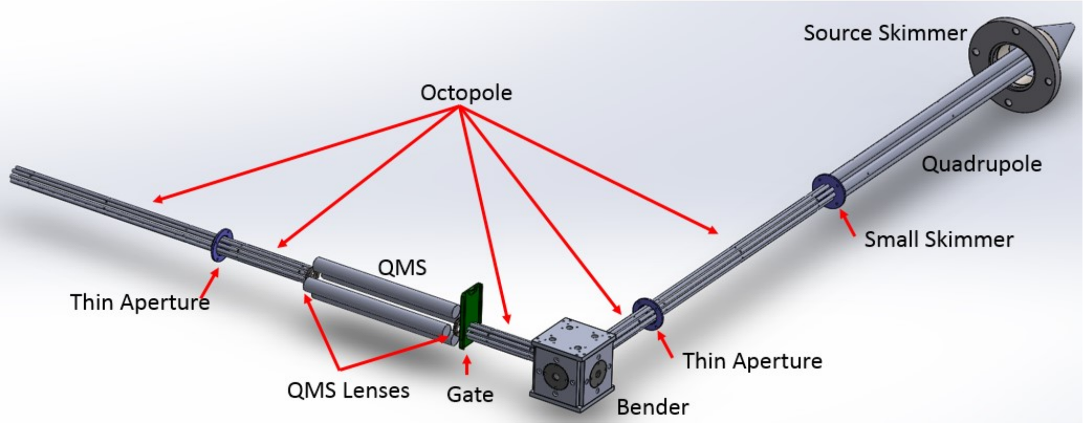

Figure V-XII*: 3D model of naked ion optics for cluster deposition beamline*

The bender itself is housed in a steel box to ensure that electric fields from nearby optics do not penetrate and change the ion trajectories. Inside the box, four quadrants of a 1” OD cylinder are arranged with an inscribed radius of 0.58” and isolated from the box via 0.125” ruby balls (**Figure V-XII**).

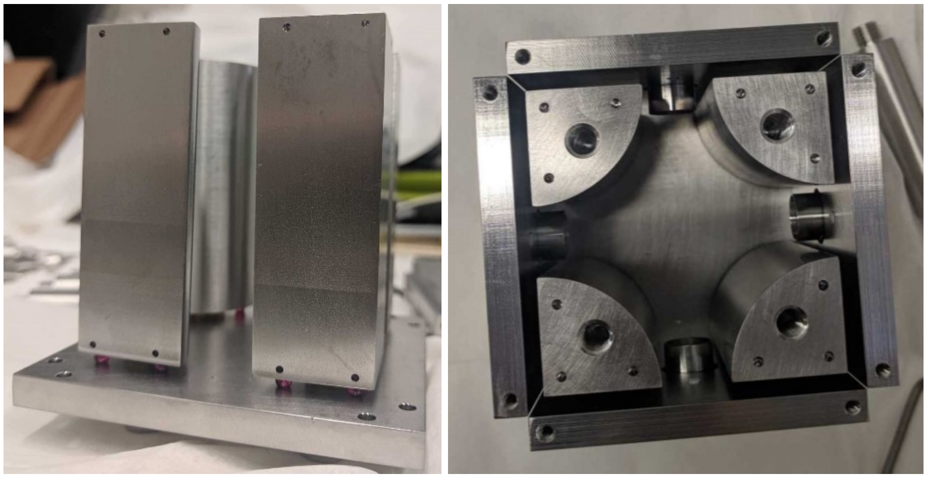

***Figure V-XIII**: Electrostatic bender assembly mounted on ruby balls (left) from abov (right)*

On each of the four in-plane faces of the box, a special tube aperture **(Figure V-XIV)** is placed to allow the ions to enter the chamber without being deflected by fringe fields that one would find near the edges of the bender quadrants. With these apertures we can also accelerate or decelerate the ion beam as it passes through the bender. They are isolated from the face of the bender box by 0.01" thin Teflon spacers.

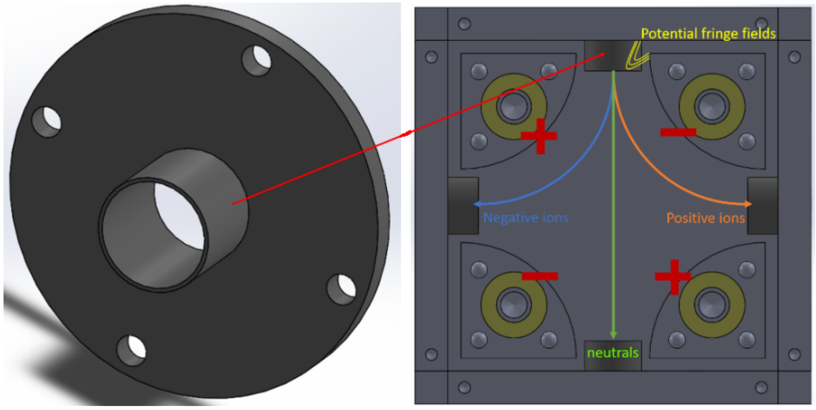

***Figure V-XIV:** Bender electrostatic aperture (left) and bender operation diagram (right)*

By applying voltages to opposite pairs of the bender quadrants, one can very easily create an electrostatic field that bends ions of the desired polarity by 90°, as shown (**Figure V-XIV**). If ions of the unintended polarity happened to still exist in the beamline, they would be “bent” in the opposite direction, and neutral molecules will continue, undisturbed by the electrostatic field, and crash into the far wall.

V.2.3 Thin Plate Einzel Lens

A newer addition to the beamline optics has been a thin plate einzel lens that is used to focus the ion beam onto the target. An einzel lens is a three-element cylindrical optic in which the first and third elements are maintained at the same potential, i.e., no acceleration or deceleration. In this way, the ions enter and leave with the same kinetic energy, but fringe fields act on outer ion trajectories and bend them into the beam axis, focusing the ions down the beamline onto an image point. Although it is hard empirically to determine the effects of focusing ions onto our HOPG surface, SIMION calculations readily show how an einzel lens will help to focus ions to a point (**Figure V-XV**).

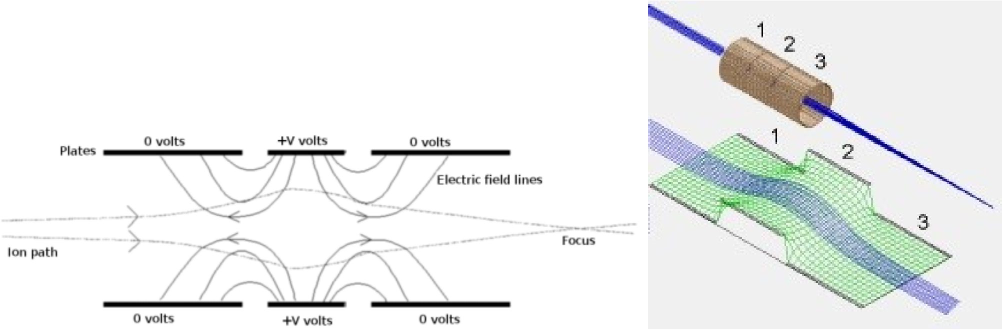

***Figure V-XV**: Einzel lens and ion trajectories, illustrated (left) and in a SIMION calculation modeling electrostatic potential (right). (5)*

After initially setting up the cluster deposition instrument, it was decided to add an einzel lens to the end of the final ion guide. To do this, we purchased thin lens optics from Thorlabs and constructed an insulating holder out of Ultem that could be slid over the end of the last octupole (**Figure V-XVI**). Voltages are applied to the lens via wires that are attached to each lens element and run to barrel connectors on a multi-pin feedthrough on a deposition chamber flange.

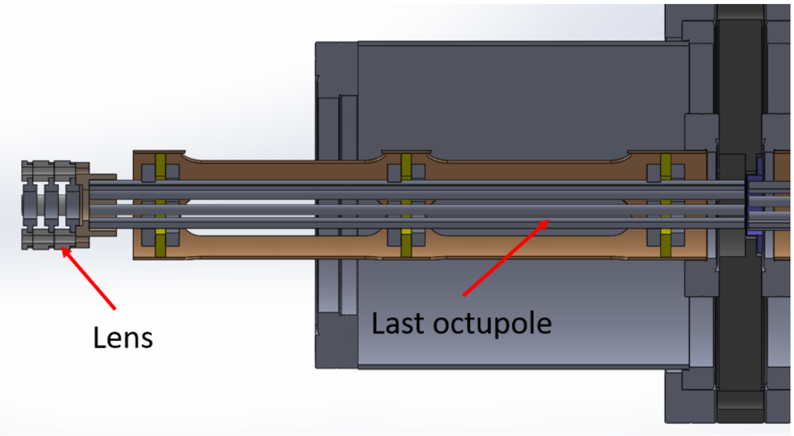

Figure V-XVI*: Cutaway side view of last octupole and deposition einzel lens*

References

1. *Fundamentals of ion motion in electric radio-frequency multipole fields.* **A. Yergey, J.E. Campana.** 1, s.l. : Journal of Physics E, 2000, Vol. 15.

2. *Features of the effective potential formed by multipole ion trap.* **S. Rudyi, T. Vovk.** 9, s.l. : Journal of Physics B , 2019, Vol. 52.

3. **Multipole Ion Guide.** ***Mass Spec Pro.*** **[Online] [Cited: 07 19, 2020.] http://www.massspecpro.com/technology/ion-optics/multipole-ion-guide.**

4. ***Collision activation of ions in RF ion traps and ion guides: The effective ion temperature treatment.*** **al, A. Tolmachev et. 11, s.l. : Journal of the American Society for Mass Spectrometry, 2004, Vol. 15.**

5. Hicks, Zachary. ***Design and Construction of Molecular Beamline for Cluster Catalysis Studies*** **. s.l. : Johns Hopkins University, 2019.**

VI Vacuum chambers and pumping system

VI.1 Vacuum theory

In order to avoid collisions with gas molecules in the air, molecular beam experiments are conducted in vacuum chambers that are designed to minimize the inevitable leaking of air into the chamber. The mean free path of a molecule, $\bar{l}$, describes the average distance a gas molecule with diameter d will travel before suffering a collision when in a region at pressure P:

$$\bar{l} = \frac{k \cdot T}{\sqrt{2} \cdot \pi \cdot P \cdot d^2}$$

Equation 15

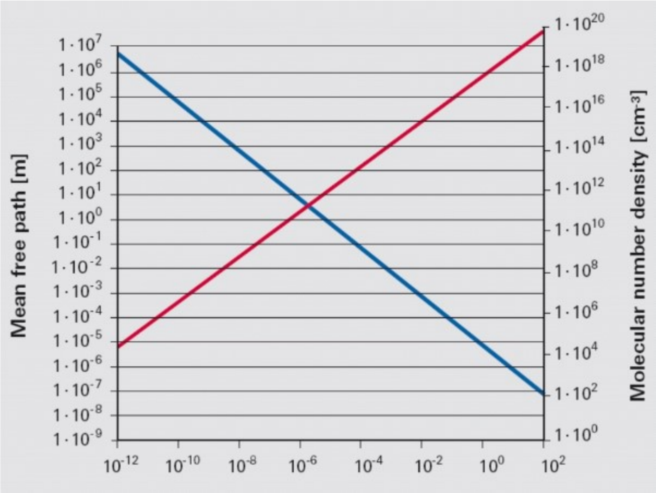

***Figure VI-I**: Graph of mean free path and molecular number density as a function of gas pressure. (1)*

As the pressure in a relatively leak-free chamber is lowered and the density of gas molecules decreases, the mean free path increases proportionally as a gas molecule can travel farther before suffering a collision (**Figure VI-I**). (1) The necessity of vacuum chambers is illustrated by the graph, where a nitrogen molecule at atmosphere, 760 torr, will travel on average 100 nanometers before suffering a collision. At $1*10^{-6}$ torr, the mean free path has been increased to roughly a meter, while at $1*10^{-8}$ torr the mean free path is almost 100 meters, providing a much more higher probability that cluster ions generated in the source will be successfully transported down the beamline to the deposition target without being knocked off course by stray gas molecules.

Figure VI-II: Pressure regimes and notable applicationsError! Reference source not found.briefly describes a few pressure regimes that can be defined and referenced for utility.

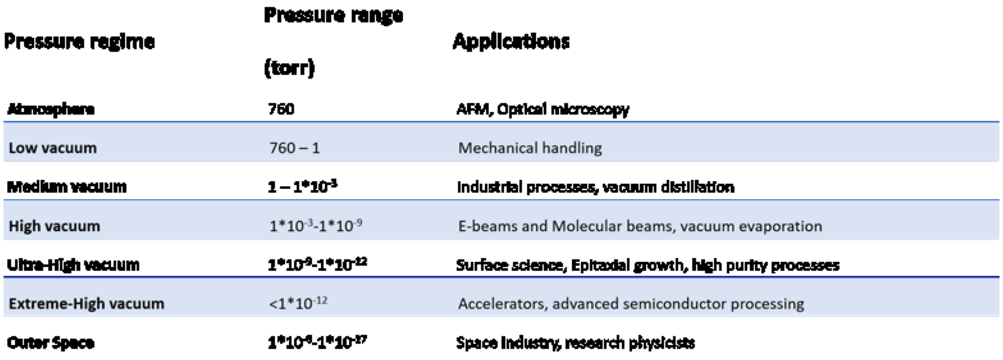

Pressure regime	Pressure range (torr)	Applications
Atmosphere	**760**	**AFM, Optical microscopy**
Low vacuum	760 – 1	Mechanical handling
Medium vacuum	**$1 – 1*10^{-3}$**	**Industrial processes, vacuum distillation**
High vacuum	$1*10^{-3}$-$1*10^{-9}$	E-beams and Molecular beams, vacuum evaporation
Ultra-High vacuum	**$1*10^{-9}$-$1*10^{-12}$**	**Surface science, Epitaxial growth, high purity processes**
Extreme-High vacuum	$<1*10^{-12}$	Accelerators, advanced semiconductor processing
Outer Space	**$1*10^{-6}$-$1*10^{-17}$**	**Space Industry, research physicists**

***Figure VI-II:** Pressure regimes and notable applications*

Vacuum pumps are used to remove gas from the inside of chambers. Gas in the chamber can originate from a number of places (**Figure VI-III),** such as the original gas in the chamber, the gas load from any techniques being run inside the chamber, entrapped gases in virtual leaks, backstreaming, atmospheric leaks, diffusion or outgassing from materials.

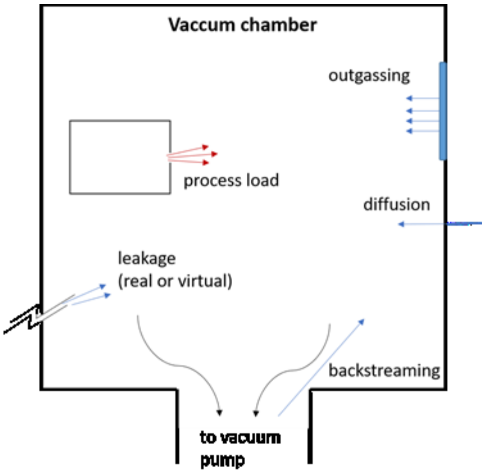

***Figure VI-III**: Illustration of some of the major sources of gas in a "sealed" chamber*

A virtual leak is one in which a pocket of air is created within the vacuum chamber, such as a by a blind-tapped screw hole or a double weld that leaks on the vacuum side, that then leaks into the chamber over time. Backstreaming occurs when gas molecules are either impinged out of the vacuum pumps or otherwise find their way through the vacuum pump and into the chamber. Diffusion is not usually an issue until at least UHV, when hydrogen diffusion in steel can present an issue, utmost care should be taken when choosing vacuum chamber materials when going below high vacuum settings. Outgassing is the slow evaporation of adsorbed molecules from surfaces. Assuming a monolayer of adsorbed molecules from contact with air, rapidly pumping a chamber down to $1*10^{-6}$ torr will leave roughly 1000 molecules adsorbed to surfaces for every gas molecule floating around. This illustrates effectively why pumping to even lower pressure is a lesson in kinetics, you are limited not only by how quickly you can pump gas out of the chamber, but also by the speed at which adsorbed gases will evaporate. Different materials will have different porosity and effective surface area, thereby increasing the level of outgassing one would expect. For this reason, after exposing a vacuum surface to air it is useful to heat up the part, or "bake", -while under vacuum to increase the rate of desorption and reduce the chamber pressure quicker, usually to 100^{oC}. Additionally, high vapor pressure metals such as cadmium, zinc, antimony and lead, in addition to many plastics, paints, flux from solder, and anything “sticky” that will create excess outgassing should be avoided in a high vacuum environment. (2) (3)

VI.1.1 Differential Pumping

In order to provide the lowest pressure environments possible for the molecular beam, a hierarchy of pumping stages, from higher pressure to the lower pressure, must be used to achieve the $<1*10^{-9}$ torr pressure in the cluster deposition chamber and as much of the beamline as possible. Called differential pumping, the practice of pumping on sequential vacuum regions that operate at different pressures and having only small orifices between them that limit gas flow is necessary to achieve UHV pressures and below for molecular beam experiments, and illustrated for a generalized molecular beam in **Figure VI-IV**.

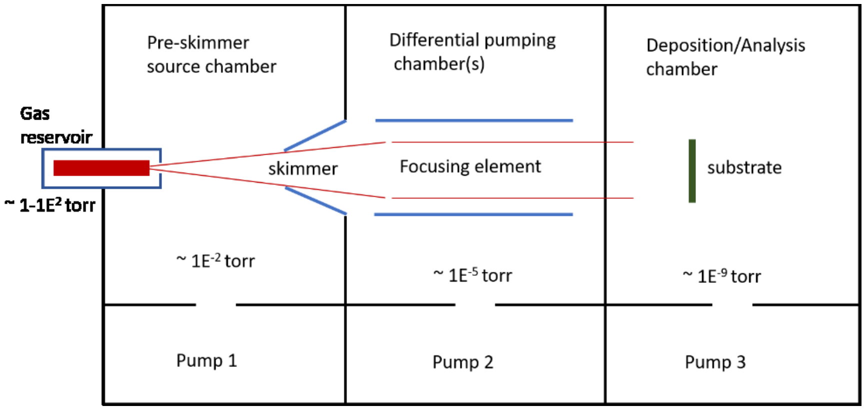

***Figure VI-IV**: Diagram of differential pumping setup that reduces the pressure in the final chamber*

VI.1.2 Vacuum Pumps

Several pump types, which have different characteristics such as blank-off pressure, throughput, and pumping speed, are used to reduce the pressure in stages. As they pertain to experimentalists, vacuum pumps can be broken down into two general categories based on their relative blank-off pressure, roughing pumps and high vacuum pumps. Roughing pumps, also called fore pumps, are meant to operate in low to medium vacuum environments. They are often mechanically driven positive displacement pumps with high throughput and are used to "rough" pump a vacuum chamber from atmosphere to medium vacuum. Roughing pumps generally rely on positive displacement to "push" air through a compression area, and several types are shown in **Figure VI-V**. (4) By their nature, rotary compression systems require a well-oiled environment, some of this oil will inevitably make its way into the compression region and backstream into the vacuum chamber itself.

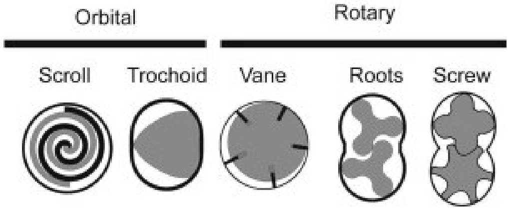

***Figure VI-V**: Diagrams of compression regions of various mechanical vacuum pumps. (4)*

This issue begins to show itself in high vacuum environments by the slow buildup of oils on otherwise clean surfaces. Care must be taken whenever shutting off a rotary vane mechanical pump to bleed it to atmosphere so that air does not leak in to the vacuum region and pull oil with it. Oil-free roughing pumps, such as scroll pumps, are necessary to back the high vacuum pumps at the upper limits of high vacuum, UHV and XHV, to avoid trace contamination by hydrocarbons in the mechanical oil.

Once a vacuum chamber has been pumped to medium vacuum by a roughing pump, it is possible to use a high vacuum pump to remove residual air and further decrease the pressure. There are a number of high vacuum pumps whose suitable operating pressure region is described by (**Figure VI-VI)**, but only the ones used in the surface deposition instrument will be described here, the turbomolecular pump, the diffusion pump, and the ion pump.

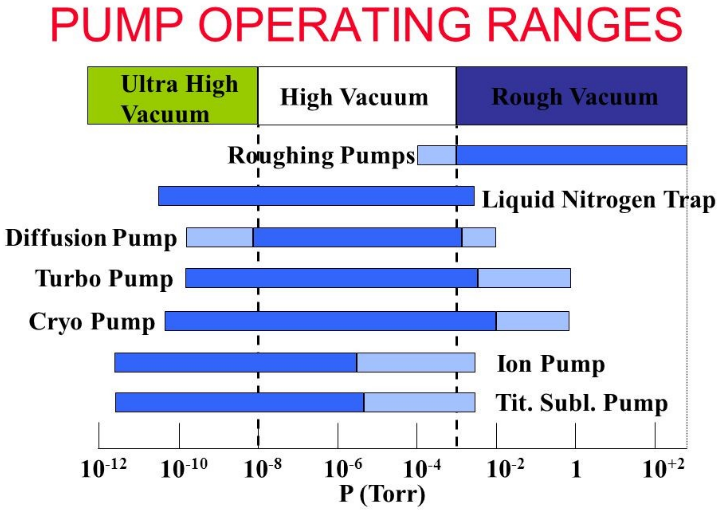

Figure VI-VI*: Chart with several relevant vacuum pumps and their respective operating pressure regime.*

Like the positive displacement pumps, turbo pumps and diffusion pumps still operate by the principle of gas transfer, yet instead of using positive displacement, the low operating pressure requires that the gas be moved via momentum transfer to individual molecules. A turbomolecular pump consists of stages of spinning and stationary fan blades, with the rotary blades mounted on magnetically levitated or highly frictionless bearings (**Figure VI-VII)**.

By spinning the blades at very high speeds (>1000 Hz) the blades hit gas molecules and transfer kinetic energy in the direction of the exhaust. The direction they will be deflected lines up with the angle of the stationary fan blade underneath, increasing the chance that gas molecules will only be directed toward the exhaust, and not in the opposite direction. In order to spin at the speeds required without building up heat from friction, the exhaust of a turbo pump should be lower than 0.1 torr, ideally in the millitorr range. In order to accomplish this, a fore pump needs to be attached to the exhaust of the turbo pump.

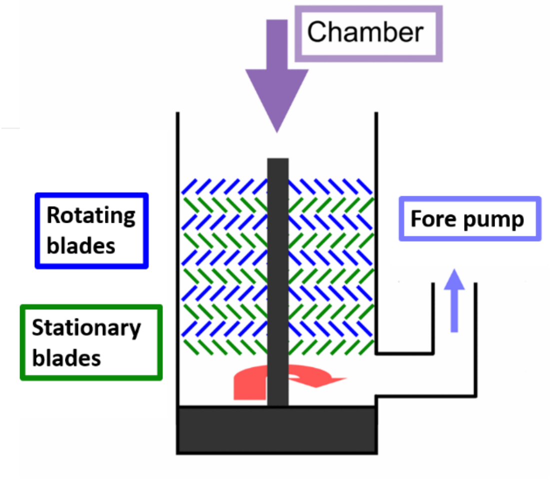

***Figure VI-VII**: Diagram of turbomolecular pump. (9)*

In this way, the fore pump reduces the pressure at the exhaust, or foreline, of the turbo pump and allows it to achieve its ultimate pressure. If the turbo is operating in UHV conditions, it is necessary to using a fore pump that is oil-free, as mentioned previously. Turbo pumps create a huge compression ratio and can quickly build up significant foreline pressure. Because the pumping speed of different gases in a turbo pump is based on their compression ratio, and compression ratio is dependent on molecular weight, heavier gases will have a higher effective pumping speed in turbo pumps. (5)

In vacuum environments that can handle a small degree of oil back-streaming, diffusion pumps offer a robust method for high pumping speed and lower blank-off pressure. With a large electric heater at the bottom of the diffusion pump, it vaporizes a synthetic oil that does not decompose at high temperatures The internal pump body forces the expanding vapor into jets that are angled downward and then toward side of the pump exhaust **(Figure VI-VIII)**.

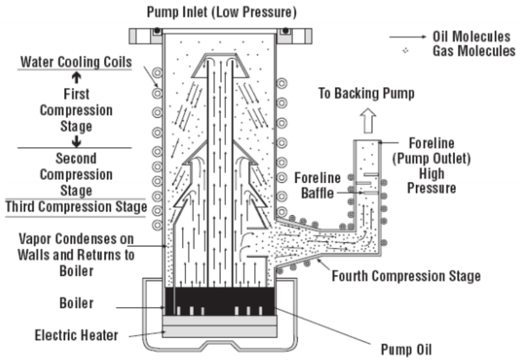

Figure VI-VIII*: Diagram of a diffusion pump. (10)*

Analogously to the turbo pump blades, individual gas molecules that make their way into the pump entrance are imparted kinetic energy by collisions with directed oil vapor. By wrapping the entire pump exterior with circulating water-cooling lines, any oil vapor that hits the interior pump walls will immediately condense and flow to the oil reservoir where it can be vaporized and restart the cycle. In a diffusion pump, the pump speed for different gases will be proportional to their flux through the pump entrance. Because the rate of effusion of gases is inversely proportional to the square root of their molecular weight, diffusion pumps will offer a higher effective pumping speed for lighter gases. (6) (7)

VI.2 Cluster Deposition Pumping System

In order to protect the sensitive equipment of the deposition/analysis chamber, and to provide the best possible vacuum environment for the molecular beam along the way, it is convenient to split the pumping system into a higher vacuum side and the relatively higher pressure source side, separated by an inline gate valve, **t**. Shown in **Figure VI-IX**, there are three main fore pumps and a number of high vacuum pumps that are used in our set-up.

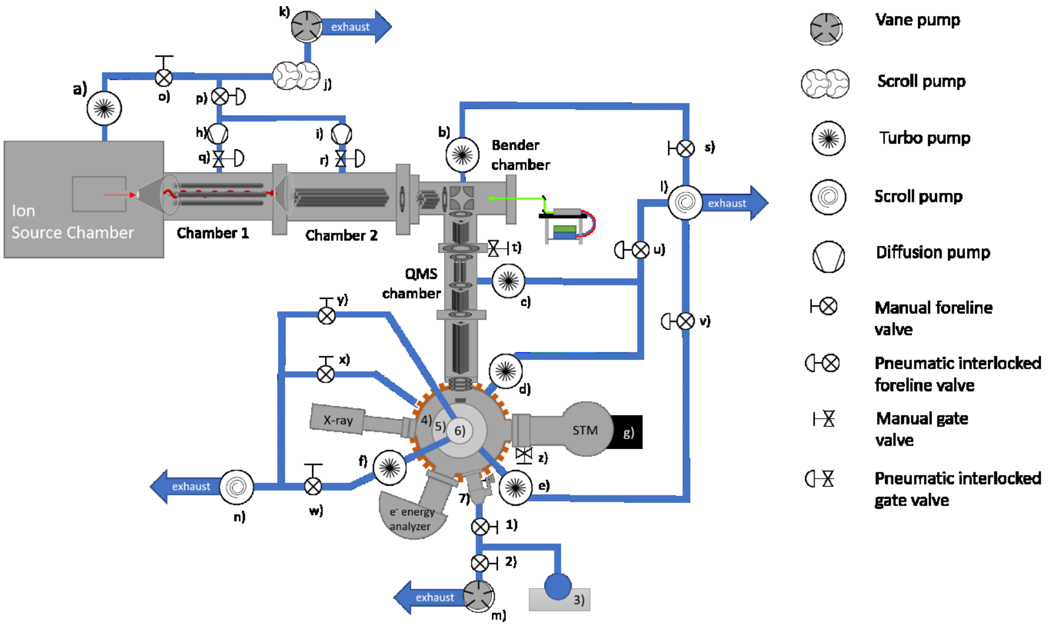

Pumps

a	Source turbo pump	Pfeiffer TPU1201
b	Bender turbo pump	Pfeiffer HiPace 700
c	QMS turbo pump	Pfeiffer HiPace 700
d	Deposition turbo pump	Pfeiffer HiPace 300
e	Basement turbo pump	Pfeiffer HiPace 80
f	Slide-seal turbo pump	
g	STM chamber Ion Pump	250 l/s diode pump
h	Ch1 Diffusion pump	Varian VHS6
i	Ch2 Diffusion pump	Varian VHS6
j	Source side vane pump	Alkaltel 2063
k	Roots blower pump	Pfeiffer WPK-500-A
l	High vacuum side scroll pump	Edwards XDS5
m	Dosing line pump	
n	Slide-seal fore pump	Leybold SC 15D

Valves and chambers

o	Source turbo foreline valve
p	Diffusion pumps foreline valve
q	Ch1 diffusion pump gate valve
r	Ch2 diffusion pump gate valve
s	Bender turbo foreline valve
t	In-line gate valve
u	Deposition turbo foreline valve
v	Basement turbo foreline valve
w	Slide-seal turbo foreline valve
x	Sample rotation stage foreline valve
y	Slide-seal roughing stage foreline valve
z	STM chamber in-line gate valve
1	Variable rate leak valve
2	Dosing line roughing valve
3	Freeze-pump reactant reservoir
4	Deposition chamber
5	Basement Chamber
6	Slide-seal pumping stages

***Figure VI-IX**: Pumping diagram of cluster deposition system.*

A rotary vane pump is used to back high vacuum pumps that operate in “dirty” environments, while scroll pumps are used to back clean high vacuum pumps that operate downstream from the source in cleaner environments. Because of the large gas load generated by the ion sources, a high speed roots pump is attached in series with the main fore pump to compress the exhaust from the high vacuum pumps so that the rotary vane pump can operate in a higher pumping speed region. Every pump has a pump curve chart, usually supplied by the manufacturer, which shows how the pumping speed can change as a result of the inlet pressure, and the compression ratio of the roots pump is used to place the rotary pump in its optimal range to handle the large gas load.

The bender turbo, QMS turbo, deposition chamber turbo and basement turbo are all backed by an Edwards scroll pump. The high vacuum side turbos are normally left running, while the bender turbo is turned on only when running an experiment. Normally the bender foreline valve **s** is left closed; in order to open **s** without flooding the foreline's of turbo pumps **c**, **d** and **e** with gas, the manual foreline valve **s** should only be opened when the foreline valves **u** & **v** have been closed, and they can be reopened once the drive current on the bender turbo is <0.7 A.

Coming off the deposition chamber, the STM chamber is separated by an in-line gate valve and pumped on by a conventional diode ion pump to achieve UHV conditions with a base pressure in the 10^{-10} torr range. The diode ion pump is based on the penning trap design by F. M. Penning previously. Briefly, he uses an arc discharge in a magnetic field, similar to the magnetron source, to ionize gas molecules and titanium atoms sputtered off the anode, all of which are accelerated towards electrodes by high voltage, >5kV. Since titanium atoms are extremely reactive, any residual gas components that collide with titanium atoms will likely form a stable product, causing an oxide and carbide heavy titanium film to develop on the anode walls. As this build up occurs and the cathode titanium is slowly sputtered away, so does the ion pumps' finite lifetime and they will need to be regenerated or replaced. (8)

Below the deposition chamber is the load-lock or "basement" chamber as it's come to be called, which is a chamber that the deposition sample can be lowered into and cleaned without exposing the deposition chamber and sensitive analytics to atmospheric pressure. The basement chamber and deposition chamber turbos are backed by the same Edwards scroll pump and use pneumatic interlocked foreline valves to protect the sensitive equipment in the case of an equipment failure. The pneumatic foreline valves are set to close if the pumps ever lose power, if compressed air is lost, or if the foreline pressure rises above 0.5 torr. The valves themselves are designed to fail closed, so any problem leads to the foreline valves shutting, preventing a shock of air rushing through the high-speed turbo's and potentially damaging them.

The slide seal is a small differentially pumped tube between the deposition and basement chambers that allows the instrument operator to drop the prepared sample though two O-ring sealed pumping stages into a chamber that can be bled to atmosphere, even as the top of the rod remains at UHV conditions. This allows convenient access to the prepared sample that clusters are deposited onto, for cleaning or replacing. This is accomplished by mounting the sample holder on the end of a 48" long, 1.375" OD tube with a mirror polish, so that it makes a good seal with the Teflon O-rings in the slide seal. After the slide-seal gate valve has been opened, a two person team can use the large viewport on the bottom of the basement chamber to align the sample holder rod, and then slowly lower the sample through the slide seal O-rings into the "basement" chamber. **Figure VI-X** illustrates the process of lowering the sample holder through the slide seal and using differential pumping to maintain a suitable base pressure in the cluster deposition chamber.

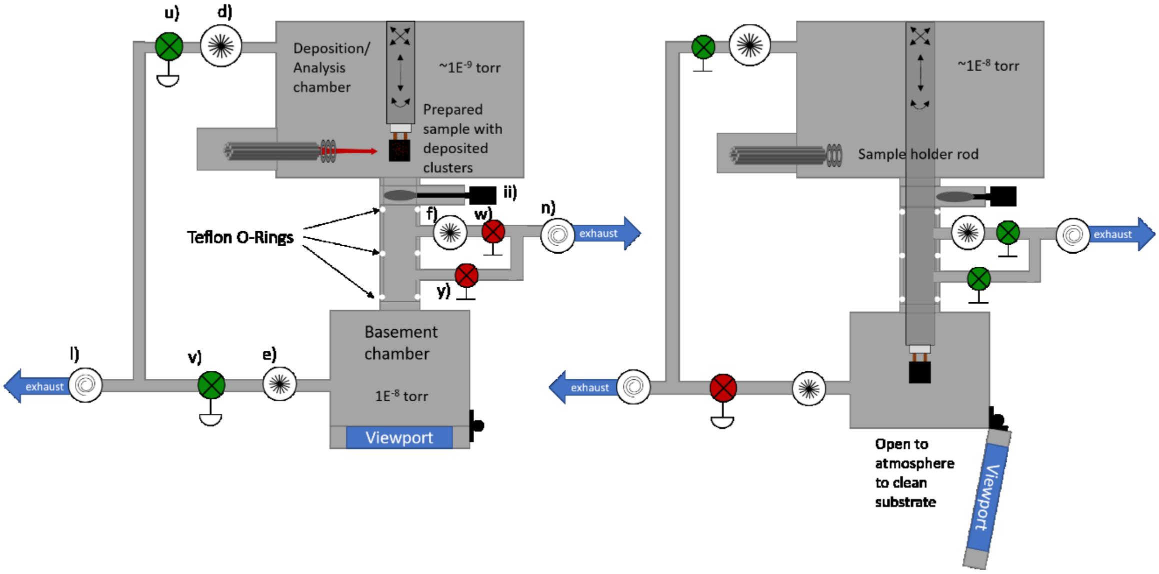

***Figure VI-X**: Diagram of slide seal and sample cleaning procedure, lowering from deposition chamber to basement chamber*

After the sample has been lowered, the basement turbo is turned off and valve **v** is closed, and air is slowly leaked into the basement chamber while the basement turbo spins down. At the same time, the slide seal turbo **f** is turned on, but its foreline valve **w** is not opened yet, causing the turbo to begin compressing gas against a closed foreline valve, it is important to not leave it like this very long. The deposition chamber pressure will begin to rise as the basement chamber is vented. Once the deposition chamber reaches $1*10^{-7}$ torr, or the basement is completely vented, whichever comes first, it is a suitable time to open the slide-seal valves, **y** first and then **w** in order to prevent backstreaming. After cleaning the sample and closing the viewport, the bender and deposition turbo foreline valves must be closed before roughing out the basement chamber. To prevent unneeded stress on the flexible metal hoses under rapid compression when pumping out the basement chamber from atmosphere, it is best to close all the forelines, turn off the scroll pump and vent it to atmosphere, open the basement foreline valve, and then turn the scroll pump back on in.

In the deposition chamber, a small gas reservoir is attached to the deposition chamber via a variable leak valve is used to dose reactants into the chamber, which can then condense on the prepared surface for reaction studies. The partial pressure of the dosed molecule in the deposition chamber can be monitored with the residual gas analyzer and the overall pressure monitored with the chamber's Bayard-Alpert nude ion gauge. The Langmuir is a unit invented by surface scientists to designate gas exposure to a surface in a vacuum setting. A gas exposure that increases the pressure by $1*10^{-6}$ torr for 1 second is defined as 1 Langmuir, which can be used as a standard unit to compare gas exposures in UHV settings.

References

1. **Pfieffer Vacuum.** 1.2.5 Mean free path. [book auth.] Pfieffer Vacuum. *The Vacuum Technology Book Volume II.* s.l. : Pfieffer Vacuum.
2. **Coyne, D.** *LIGO Vacuum Compatible Materials List.* s.l. : LIGO, 2011.
3. **Danielson, Phil.** *Choosing the right vacuum materials.* [https://www.normandale.edu/departments/stem-and-education/vacuum-and-thin-film-technology/learning-in-a-vacuum---what-to-expect/articles/choosing-the-right-vacuum-materials] s.l. : R&D Magazine.
4. **Michael Smith Engineers LTD.** [Online] [Cited: 07 23, 2020.] https://www.michael-smith-engineers.co.uk/resources/useful-info/positive-displacement-pumps.
5. **Leybold.** *Introduction to high vacuum and ultra high vacuum production.*
6. —. *High Vacuum Pumps.*

7. **OpenStax, Chemistry. OpenStax CNX. Jun 20, 2016 http://cnx.org/contents/85abf193-2bd2-4908-8563-90b8a7ac8df6@9.311.** *Effusion.*

8. **Schultz, L.** *Sputter-Ion Pumps.* [pdf] s.l. : CERN.

9. **Elina.** "Turbomolecular Pumps: Learn about Turbomolecular Pumps." *VacCoat*, 15 Aug. 2020, vaccoat.com/blog/learn-more-about-turbomolecular-pumps/.

10. **O'Brien, Kerry.** "DigiVac Training for Customers." *SlideShare*, 7 Oct. 2016, www.slideshare.net/KerryOBrien16/digivac-training-for-customers-66872427

VII Deposition and analysis system

VII.1 Deposition chamber

The purpose of the cluster deposition instrument is to generate cluster ions, mass select a species of interest from the resulting molecular beam, and gently deposit them onto a prepared surface, in our case a freshly cleaned, highly-oriented pyrolytic graphite (HOPG) sample (1cm x 1cm). The cluster deposition happens in the deposition chamber (**Figure VII-I**) where the sample is held in the path of beam, directly following the deposition lens, by a mechanically manipulatable sample holder rod.

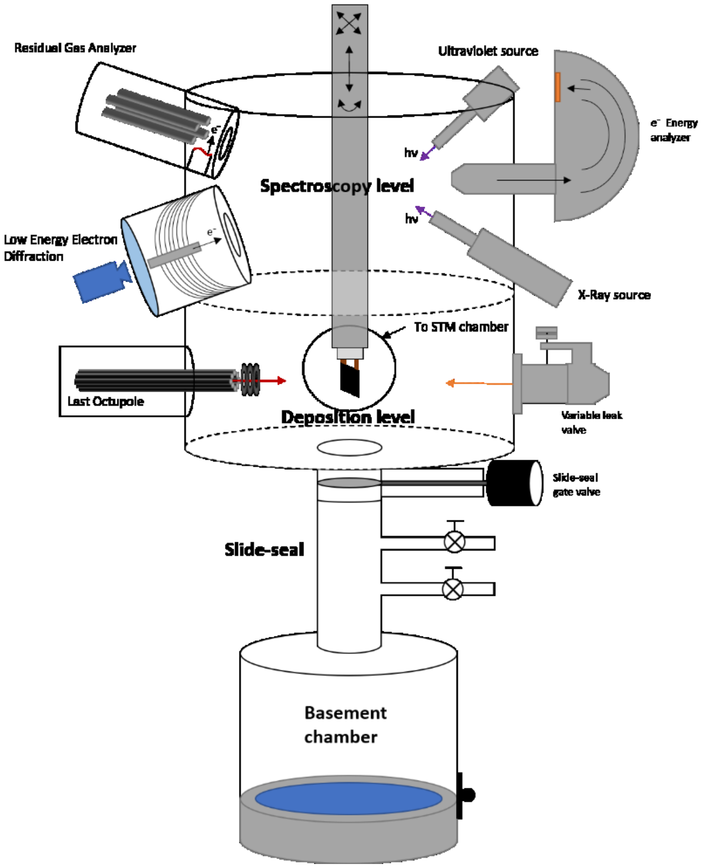

Figure VII-I: *Diagram of the cluster deposition chamber with analytics positioned roughly correctly but not to scale*

The sample holder tube is a hollow, 48” long mirror polished steel tube that is manipulated with motors on the top flange to give X, Y, Z and rotational motion to the sample. In this way, the sample can be moved around and “parked” in front of any of the techniques and instruments protruding into the deposition chamber or moved through the slide seal in order to clean or replace the prepared sample. The sample is mounted on titanium clips that are handmade and attached to a 2-pin miniconflat power/thermocouple feedthrough, allowing current to be run through the sample for resistive heating, and the measurement of the sample temperature with a K-type thermocouple.

Inside the deposition chamber, there are two levels of chamber ports that have attached equipment. There is a deposition level, where the dosing and cluster deposition generally happens, and a spectroscopy level, where several probe techniques are installed to characterize the surface and its reactivity (**Figure VII-II**).

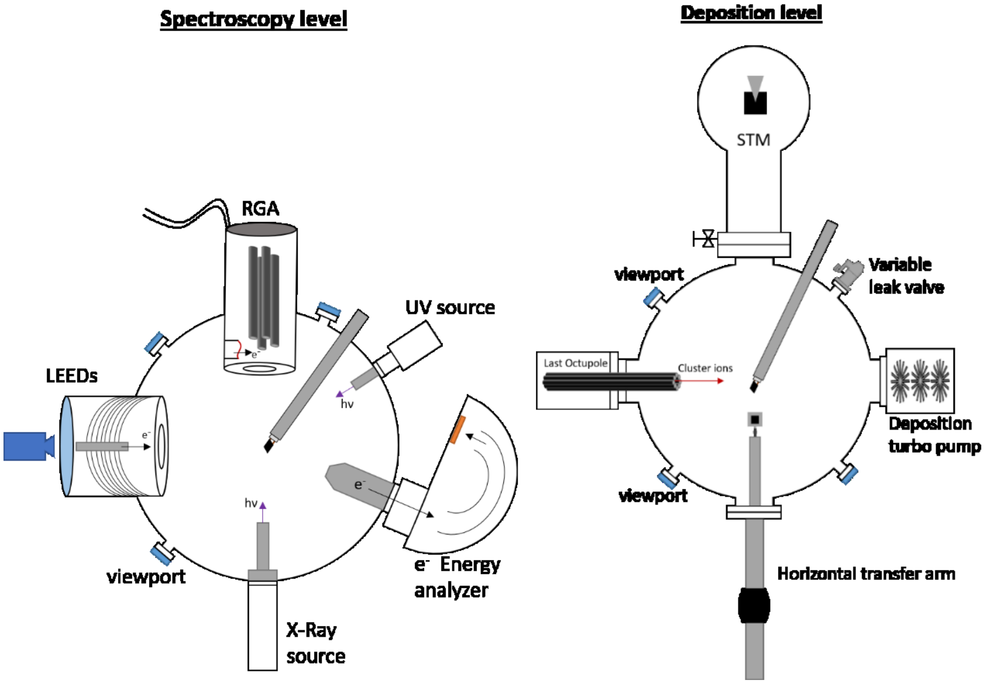

***Figure VII-II**: Illustration of the two levels of tools and techniques in the deposition chamber*

At the deposition level, the last octupole and lens set protrudes into the chamber, allowing the ion-guiding electric fields of the beamline to continue nearly all the way to the sample surface. Because the sample can be moved around in the chamber via the sample holder, it can be moved as close to the last lens element as possible and centered on the beam axis. Several glass viewports are mounted around the chamber on both levels in order to facilitate the positioning of the sample for various procedures. Also on the deposition level is the variable leak valve for the application of controlled doses of gas exposure to prepared surfaces for reactivity studies, the deposition turbo pump, and an inline gate valve that leads to the vacuum chamber in which is housed the scanning tunneling microscope (STM). The STM is accessible to the instrument operator using a horizontal transfer arm that is not currently installed on the instrument in order to leave an extra viewport but can easily be installed when STM studies are necessary. After raising the sample to the spectroscopy level, it can be exposed to different wavelength light sources, or probed with the residual gas analyzer (RGA), the low energy electron diffraction spectrometer, or hemispherical electron energy analyzer.

VII.2 Analysis Techniques and Instrumentation

VII.2.1 Residual Gas Analyzer

Studying the reactivity of deposited clusters is a difficult task, there is no “property of reactivity” that can be passively measured, instead, one must observe reactions happening in real time, by knowing the initial reactants and their amounts, and then characterizing the quantity and identity of their products. A vital tool for carrying out studies of this type on surfaces is the residual gas analyzer (RGA) which is essentially a quadrupole mass spectrometer in series with an electron bombardment filament to ionize incident molecules, and a multichannel plate detector to detect ions of the correct *m/z* that make it through the QMS field undisturbed, as shown schematically in (**Figure VII-III**).

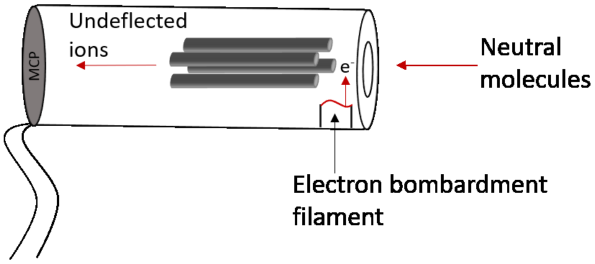

Figure VII-III: *Residual gas analyzer for monitoring the desorption of gases from a surface in UHV*

The multichannel plate is a sensitive charged particle detector that uses an emissive coating to amplify the detection signal to a level that can be easily detected as current and resolved from background noise. Neutral molecules with trajectories into the inlet of the RGA will undergo collisions with fast moving electrons from the filament that have a large chance of knocking off another electron and possibly cause the molecule to fragment into pieces. Collision induced dissociation is the mechanism by which neutral molecules being ionized by fast moving particles will fragment due to the a conversion of collisional kinetic energy to internal energy, which results in bond dissociation that can either split the bonded electrons between the fragments or see them preferentially stay with one of the fragments. Luckily, molecules will follow predicted fragmentation patters in these situations, and it is therefore vital that mass spectra collected using such harsh ionization techniques as electron bombardment be calibrated with fragmentation patterns of potential species in order to correctly determine the identity and abundance of different species entering the mass spectrometer, in this case the QMS of an RGA. The RGA is mounted on a linear manipulation bellows system so that it can be inserted into the chamber or retracted. When monitoring desorbing products from a surface, it is best to position the inlet of the RGA as close to the sample surface as possible (<1cm) and retract it afterwards to avoid collision when maneuvering the sample around.

VII.2.2 Temperature Programmed Reaction/Desorption Spectroscopy

In the process of Temperature Programmed Desorption/Reactivity (TPR/D), a sample is preloaded with reactants while held at an extremely low temperature in order to slow down reactions and aggregation processes that could happen on the surface. By positioning this cold pre-loaded sample directly in front and as close to the inlet of an RGA as possible, and then linearly increasing the sample temperature, a reaction can be induced between the reactants in a controlled manner and then the desorbed species from the surface can be detected with the RGA. By quantifying the identity and abundance of species desorbing from the surface, it is possible to deduce information which is directly related to the reaction mechanism and thermodynamics. The RGA measures reaction products indirectly by detecting the species that desorb from the surface.

In the surface deposition instrument, the RGA is a Hiden 301/3F RGA, containing a QMS with a mass limit of 300 amu. The detector is sensitive enough to detect volatile reaction products down to 4*10-15 torr partial pressures and up to 650 measurements per second. The fast scan time of the RGA is vital for TPD/R experiments and can be used to monitor the changing desorption intensity of several species when in multi-ion-detection mode. The QMS and filament ionizer are contained within a quartz housing with a 5mm OD hole in the front face to prevent stray gas molecules from entering the ionizer and QMS.

The sample is heated by attaching the copper leads that the sample is mounted on to a Sorensen DCS 55-55 programable high current power supply. By running current through the conductive sample, it is heated resistively. In order to maintain the isolation of the sample, the sample temperature is converted by a DAT 4531A isolation converter from the thermocouple's thermoelectric voltage to a proportional voltage on a 0-10 V DC scale, with -200°C being 0 V and 500°C corresponding to 10 V DC. The 0-10 V sample temperature is fed to a Eurotherm 2408 PID controller that monitors the sample temperature and outputs a programming current to the Sorensen high current supply, instructing it on what current to output. By accounting for the current deviation (proportional), the historic deviation (integral) and rate of change of deviation (differential), a PID controller is well suited to apply a precise temperature ramp to a sample under a range of conditions.

In a typical cluster deposition TPD/R experiment, e.g., those studying the decomposition pathways of chemical warfare agents over deposited metal oxide clusters, the sample is initially cooled to -170°C with liquid nitrogen (LN2). Using the leak valve, the sample is exposed to a predetermined amount of a chemical warfare agent simulant, such as dimethyl methylphosphonate (DMMP), measured in Langmuires. Exposing the sample to a gas while at this temperature will cause the gas to condense on the surface, forming a multilayer, or "frozen matrix" as the method has become known. Once a frozen matrix of DMMP has been condensed on the surface, the sample is positioned behind the electrostatic deposition lens, and a metal oxide cluster species is "soft landed" on the prepared surface via the molecular beam as described previously. By measuring the current generated by singly charged ions hitting a grounded surface, the surface coverage is explicitly measured. A monolayer is defined as 1 particle per active site for a particular surface based on its lattice parameters, but is often on the order of $\sim 1.5 \times 10^{15}\ particles/cm^2$, and the deposition is usually recorded as a fraction of a monolayer.

Once the appropriate quantity of metal oxide clusters are deposited onto the frozen matrix of DMMP, the sample temperature is raised to an intermediate temperature far away from the RGA, in order to remove the multilayers of DMMP without overwhelming the sensitive detector of the RGA. This initial annealing temperature is chosen empirically by trying different annealing temperatures and choosing the one that produces the best quality results. The purpose of first preparing the surface under cold conditions and then allowing the species to briefly interact during the intermediate anneal is to help the clusters and dosed reactants to saturate active sites on the clusters before they can aggregate on the surface. Once the sample has been annealed to this intermediate temperature, often $20^{\circ C}$ for 2 minutes, it is cooled back to $-200^{\circ C}$ and then positioned directly in front of the RGA. Finally, the sample temperature is linearly increased by its controller to a maximum of $500^{\circ C}$, as described by the following equations;

$$T(t) = T_0 + \beta t$$

Equation 16

$$\frac{dT}{dt} = \beta$$

Equation 17

If the surface coverage Θ is defined as the fraction of sites on the surface that are filled by an absorbed molecule, the principle of microscopic reversibility produces an equation relating the rate of desorption to surface coverage for an n^{th} order reaction;

$$r_{des} = -\frac{d\Theta}{dt} = k_d \cdot \Theta^{\mathrm{n}}$$

Equation 18

Or by making a variable substitution using the linear temperature ramp,

$$\frac{-d\Theta}{dT} = \frac{k_d}{\beta}\Theta^n$$

Equation 19

From the Arrhenius equation we can relate the rate constant for a desorption process k_d to the desorption energy E_d and a preexponential factor A:

$$k_d = Ae^{-\frac{E_d}{RT}}$$

Equation 20

Combining these equations results in the Polanyi-Wagner equation which is the starting point for analysis of most TPD data:

$$r_{des} = -\frac{d\Theta}{dT} = \frac{A}{\beta} \cdot \Theta^n \cdot e^{-\frac{E_d}{RT}}$$

Equation 21

In a method outlined by Redhead (1), it can be shown that for a first order desorption, by differentiating the Polanyi-Wagner equation and setting the differential of the desorption rate equal to zero, the desorption energy E_d can be solved for directly as a function of the peak desorption temperature T_p.

$$\frac{E_d}{RT_p^2} = \frac{A}{\beta} e^{\left(-\frac{E_d}{RT_p}\right)}$$

Equation 22

Solving for the desorption energy and assuming the value of A/β to be between 10^8 and 10^{13} K^{-1} produces the following conclusion to the Redhead analysis for a first order desorption:

$$E_d = RT_p \left[\ln\left(\frac{AT_p}{\beta}\right) - 3.26 \right]$$

Equation 23

Which allows a simply and approximate estimation of the desorption energy of a species given its peak desorption temperature from a TPD spectra and assuming a preexponential factor A which is usually on the order of 10^{13} s^{-1}. Qualitatively, for a species X desorbing with a lower peak temperature than species Y, species X will have a lower desorption energy than species Y. As described earlier, the desorption energy should be distinguished from the reaction energy, however if the reaction is the rate limiting step and desorption is immediate, then E_d is equal to E_{rxn}. (2) (3)

VII.3 Photoelectron Spectroscopy for Surface Analysis

In 1905, Einstein made his first Nobel prize winning discovery when he correctly explained the photoelectric effect via the quantization of light into massless particles that he called *quanta* and we now know as photons. Heinrich Hertz and other scientists at the end of the 19th century realized that incident light of a sufficient frequency that hits a metal surface will eject electrons whose energy is proportional to the frequency of the incident light rather than its brightness, but could not understand the origin of this phenomena. Einstein famously theorized that light was quantized, and a surface would emit electrons only when the incident photon energy was greater than the minimum energy required to remove an electron from the surface of the material, known as the work function. This explained why the energy of the emitted electrons was dependent on incident photon energy only, while the abundance of emitted photoelectrons was dependent on the number of incident photons, rather than their energy. (4)

The kinetic energy of the ejected photoelectron is then dictated by the conservation of energy relationship, wherein it will be the difference between the incident energy of the photon and the total energy initially binding the electron to the material or molecule, as shown for an incident X-ray photon with enough energy to detach a core level electron in **Figure VII-IV**.

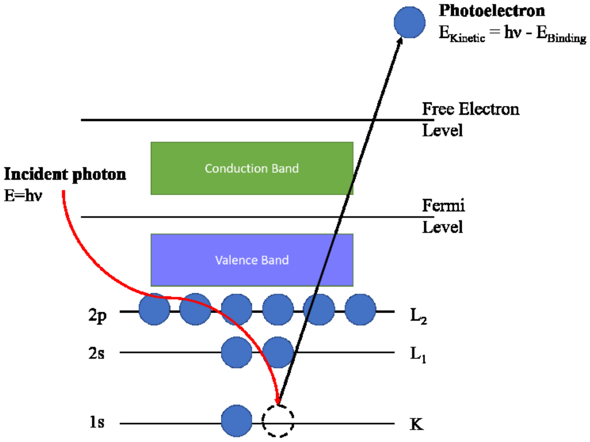

Figure VII-IV: *photoemission process depicted in the electron band structure of a hypothetical atom*

In 1951, Steinhardt and Serfass described the development of a device that would take advantage of the photoelectric effect for the chemical analysis of a surface. (5) By illuminating a prepared surface with a fixed frequency X-ray source, they discovered that by measuring the kinetic energy and intensity of ejected photoelectrons, they could "perform a quantitative analysis of the nominal surface of a solid". With a fixed photon frequency, they could measure the kinetic energy of the ejected electron to determine the original binding energy it had. After removal of a core electron, an atom will either relax via x-ray emission or the emission of an Auger electron.

The technique, by virtue of the mean free path of electrons in a solid, probes only the top layers of a surface. In a solid, the inelastic mean free path of electrons in a solid follow a characteristic curve displayed in figure X. (6)

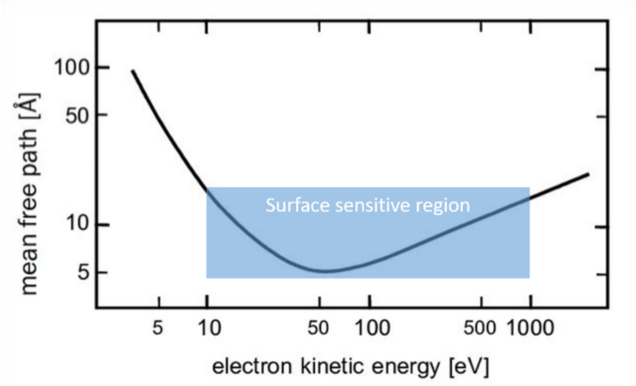

Figure VII-V: *Universal curve of Inelastic mean free path for an electron in a solid*

Because the kinetic energy of photoelectrons tends to be in the range of 10-1000 eV and while they may be generated deep in the material via photon processes, only photoelectrons generated in the most superficial layers will be able to escape the solid for detection, so this analysis is inherently surface sensitive. Because every element will have different binding energies for the same electron orbital, it is possible to use the measured binding energy as a fingerprint to determine the identity and abundance of atoms on the surface. At a deeper level of analysis, small changes in the local binding environment of an element causes *chemical shifts*, or small shifts in the binding energy of the electron, which are then detected via the measurement of the ejected kinetic energy. **Figure VII-VI** shows the how the binding energy for a 1s electron changes dramatically for first row elements, and how within a specific photoelectron peak, or envelope, different binding environments lead to small changes in the peak shape and position.

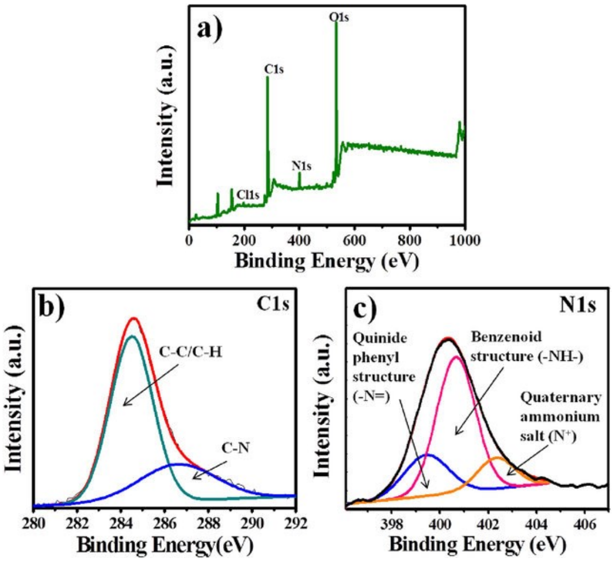

***Figure VII-VI**: XPS spectra of a) various 1s orbitals for row 1 elements, b) & c) chemical shift in orbital envelope*

Electron withdrawing groups bonded to the probed atom will pull electronic density away from the atom, unshielding the positively charged nucleus and causing electrons to be more tightly bound, i.e. have higher binding energy. Because of spin orbit coupling, some peaks will be split, with their height ratios determined by their degeneracy. While the shape and position are dependent on the local electronic environment, the integrated area under the peak is a measure of the relative abundance of the atom that produced the peak. Although there is a rising background in photoelectron spectra due to electron scattering, peak integration with the proper background subtraction method is a useful tool for determine the relative abundance of different elements on a surface, allowing one to make composition and even structural determinations.

While core level electrons can be ejected and measured to identify elements with X-ray photons, less strongly bound valence electrons can also be ejected via the same process with photons of less energy in the ultra-violet range. Using ultra-violet photoelectron spectroscopy (UPS), valence electrons and their local bonding environment can be probed, as well as electronic work function of the surface. Because UV photon sources create photoelectrons with kinetic energies of at most ~ 40eV, the photoelectrons have a shorter mean free path and UPS is inherently even more surface sensitive than XPS. (7)

VII.3.1 Electron Kinetic Energy Analyzer

Only two years after Einstein published his 1905 paper on the photoelectric effect, a student of J.J. Thomson, P. D. Innes constructed a device to deflect electrons by an angle that was proportional to their velocity, giving a measure of kinetic energy and became the first to measure the photoelectron emission spectrum of a material. (8) Innes' instrument was impractical and the development of a robust energy analyzer for electrons was slow until Steinhardt and Serfass's 1951 paper describing a device for the relatively simple quantification of elements present on a surface. Thanks to Milliken's 1909 oil droplet experiment, the mass of the electron was known and scientists could now solve directly for the kinetic energy of ejected electrons. Unlike the early version by Innes, electron impacts were recorded electronically rather than on photosensitive plates, of deflected electrons of the correct velocity through a 180° bend in the flight tube using a variable magnetic field (**Figure VII-VII**).

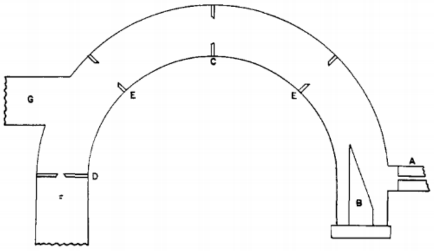

Figure 3. Schematic Diagram of Spectrometer Tube

Figure VII-VII: *Early electron kinetic energy analyzer*

In versions of the instrument that followed, the magnetic field was replaced in favor of an electric field, but the double hemisphere remained; and the hemispherical electron energy analyzer is the most versatile tool for electron energy analysis over an extended range. A modern hemispherical electron energy analyzer consists of electron input optics, a pair of hemisphere electrodes, and sensitive electron counting equipment (**Figure VII-VIII)**.

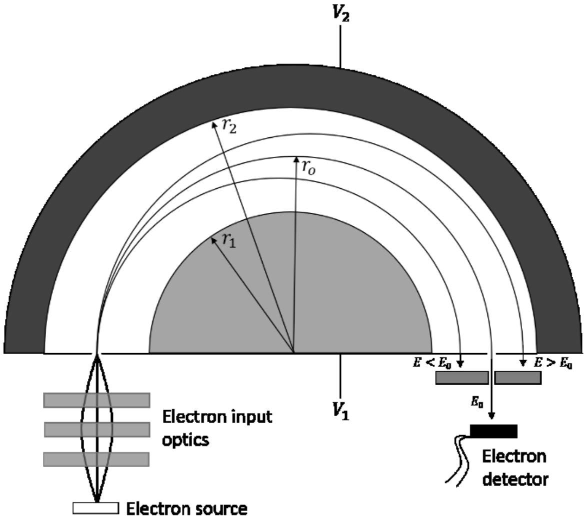

Figure VII-VIII*: diagram of modern hemispherical electron energy analyzer*

Electrons that enter the hemisphere with the correct kinetic energy to travel along the equipotential path half-way between hemisphere electrodes and onto the electron detector are said to have kinetic energy equal to the pass energy, E_0. The two applied voltages V_1 and V_2 create an electrical potential that varies with the radial coordinates according to the Laplace equation:

$$V(r) = -\left[\frac{V_2 - V_1}{r_2 - r_1}\right] \cdot \frac{r_1 r_2}{r} + const$$

Equation 24

Assuming the absence of fringe fields, the radial electric field in between the hemispheres will then be given by:

$$|E(r)| = -\left[\frac{V_2 - V_1}{r_2 - r_1}\right] \cdot \frac{r_1 r_2}{r^2}$$

Equation 25

The required potential for the inner and outer hemispheres is then described by Equation 26 and Equation 27: (9) (10)

$$V_1(r) = V_0\left[\frac{2r_0}{R_1} - 1\right]$$

Equation 26

$$V_1(r) = V_0\left[\frac{2r_0}{R_2} - 1\right]$$

Equation 27

Where the pass energy potential V_0 is related to the pass energy by the electron charge e according to:

$$E_0 = eV_0$$

Equation 28

Over time, many hemispherical energy analyzers have come to operate in constant pass energy mode, instead of using the input optics to accelerate electrons of different initial kinetic energies to the correct pass energy. Because the energy resolution of the hemisphere is proportional to the pass energy, a constant pass energy produces spectra with a constant resolution.

The cluster deposition chamber is equipped with a Perkin-Elmer PHI Model 5100-360 Electron Energy Analyzer with an extended lens. The X-ray source is a PHI 04-548 dual anode source with two filaments, capable of emitting either the Mg $K\alpha$ 1253.6 eV or the Al $K\alpha$ 1486.6 eV characteristic emission. The ultraviolet source is a PHI 232 UV lamp capable of creating the He 1α 21.2 eV and 2α 40.81 eV emission lines. The electron energy analyzer is positioned symmetrically between the UV and X-Ray sources on the deposition chamber, so that the angle both sources and the hemisphere entrance is 54.7°, “the magic angle”. The angular symmetry parameter $L_A(\gamma)$ describing how the intensity of a particular core level photoemission line changes with the angle γ between the incident photon and the outgoing photoelectrons is given by;

$$L_A(\gamma) = 1 - \frac{\beta(3\cos^2\gamma - 1)}{4}$$

Equation 29

At the angle where $\gamma = \cos^{-1}\left(\frac{1}{\sqrt{3}}\right)$ or approximately γ = 54.7°, $L_A(\gamma)$ is equal to one, and the asymmetry parameter has no effect on the quantification of emitted photoelectrons. (11) For this reason, the deposition chamber was manufactured with the port for the hemispherical electron energy analyzer 54.7° away from either the X-ray or UV photon source.

VII.3.2 Low Energy Electron Diffraction Spectroscopy

In 1924, Louis de Broglie postulated his theory on the particle/wave duality of all matter; the de Broglie wavelength λ of a particle was related to a particle’s momentum and therefore it’s mass by the Planck constant h according to Equation 30.

$$\lambda = \frac{h}{p} = \frac{h}{mv}$$

Equation 30

In 1927, Clinton Davisson and Lester Germer at Bell Labs confirmed this experimentally when a beam of electrons incident on a nickel crystal target created backscattered electrons who’s intensity showed diffraction patterns. (12) It wasn’t for over 30 years, in 1960, that Germer was able to create a versatile technique that would effectively measure the angle and intensity of backscattered electrons. (13) Called low energy electron diffraction (LEED) spectroscopy, the technique involves directing a beam of 20-200eV electrons at a sample target. By applying deceleration potential grids before a phosphor screen, secondary electrons can be rejected, and the backscattered electron diffraction pattern can be measured.

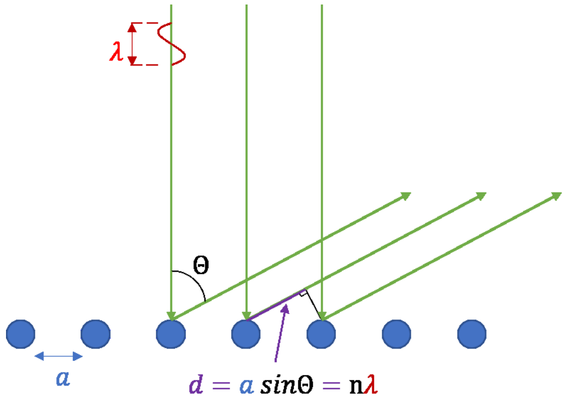

***Figure VII-IX**: Bragg diffraction from surface atoms*

Due to the constructive interference of waves, only diffraction angles where $n\lambda = a\sin\Theta$, such that the difference in path length of photons is a multiple of their wavelength (**Figure VII-IX**), will have strong electron diffraction signal. In the typical LEED set-up and experiment, shown in **Figure VII-X**, (14) an ordered surface will create spots on the detector screen according to the constructive interference of diffracted electrons defined by Bragg's law.

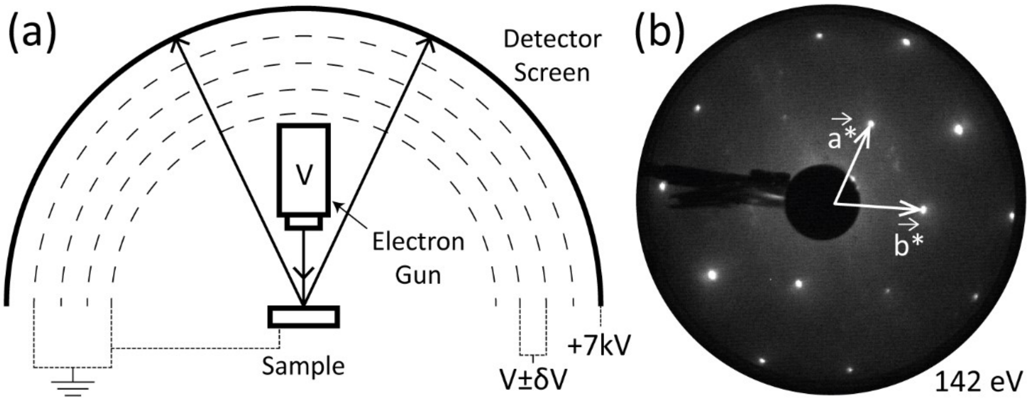

***Figure VII-X**: (a) Diagram of LEED setup. (b) Unprocessed LEED spectrum where spots represent lattice points in reciprocal space*

The reciprocal lattice vectors can be used to find the lattice parameters of the surface, or the spot intensity can be plotted as a function of circumferential angle to show the relative disorder of the surface; sharp peaks demonstrate well-ordered layers while diffuse peaks suggest a level of disorder between surface layers. (15) Finally, for complete structural determination, spot intensity can be measured as a function of electron beam energy to produce I-V curves with characteristic shapes for different functional groups, which can be compared to computational results to determine or verify structure (**Figure VII-XI**).

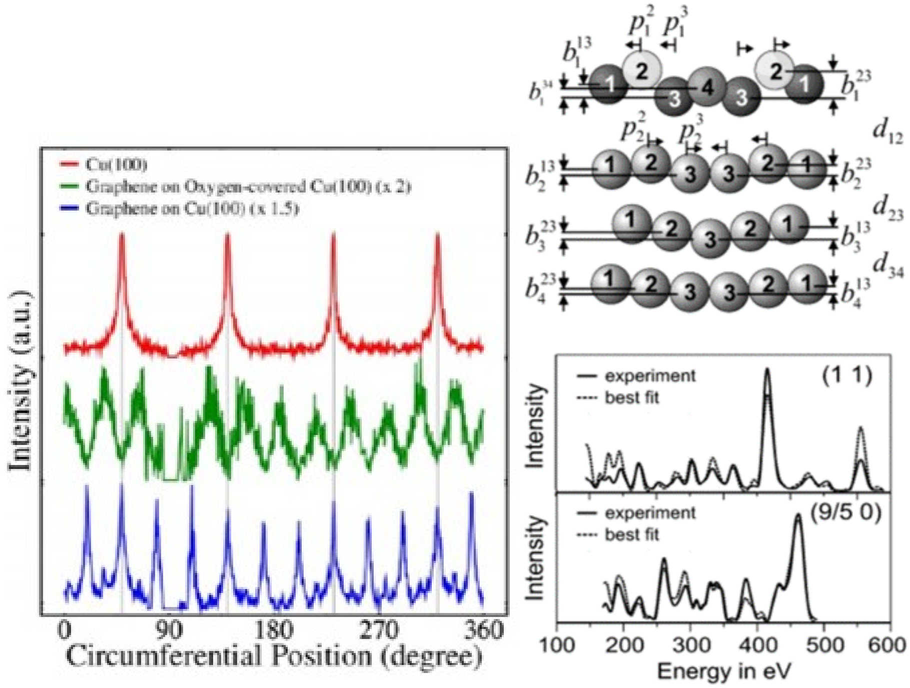

Figure VII-XI: *Spot intensity as a function of circumferential angle (left), I-V curve pictured with the surface it represents (right)*

The cluster deposition chamber is equipped with a SPECS ErLEED 1000-A in the spectroscopy level. In future experiments depositing clusters on prepared metal or metal oxide surfaces, LEED will be instrumental for verifying the structural characteristics of the surface.

VII.3.3 Scanning Tunneling Microscope

After developing the predecessor to the STM, a microscope that relied on field emission from a piezoelectric controlled tip to map the electronic surface topography in 1972, Russell Young was credited by the Nobel Committee for realizing that the tunneling current would produce a high resolution probe. In 1981, Gerd Binnig and Heinrich Rohrer used this information to create the first scanning tunneling microscope (STM) for which they won the Nobel Prize in 1986. In an STM, a conductive tip is brough extremely close to a surface using sensitive piezoelectric movement. When a voltage bias is applied to the probe tip, it's fermi level is raised and there is a tunneling current between the tip and sample that is influenced by the local density of states in both the tip and sample, as shown in (**Figure VII-XII**).

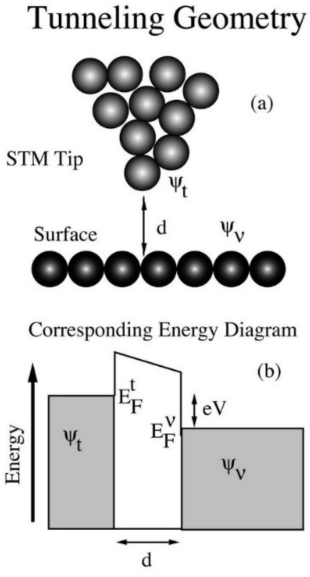

***Figure VII-XII**: Diagram of the STM geometry (a) and Electronic band structure (b), note the dimension d is flipped*

The instrument is equipped with an OMNICRON 1 *in-situ* STM for studying the surface topography. With the STM it is possible to study the aggregation of clusters after being deposited on the surface. In earlier work done with this instrument, the aggregation of ZrO clusters was studied.

References

1. *Thermal Desorption of Gases.* **Redhead, P.A.** 4, s.l. : Vacuum, Vol. 12. 1962.

2. **G Doll, P Shiller.** Thermal Desorption Spectroscopy. [book auth.] ASM International. *Materials Characterization.* 2019.

3. **S Schroeder, M Gottfried.** *Temperature-Programmed Desorption (TPD) Thermal Desorption Spectroscopy (TDS).* s.l. : FU Berlin, 2002.

4. *On the histroy of photoemission.* **H.P. Bonzel, Ch Kleint.** 2, s.l. : Progress in Surface Science, 1995, Vol. 49.

5. *X-Ray Photoelectron Spectrometer for Chemical Analysis.* **R. Steindardt, E. Serfass.** 11, s.l. : Analytical Chemistry, 1951, Vol. 23.

6. *Photoelectron Spectroscopy in Materials Science and Physical Chemistry.* **A Klein, T Mayer, A Thissen, W Jaegermann.** 4, s.l. : Sci. Phys. Chem. Bunsen-Magazin, 2008, Vol. 10.

7. **Thermo Scientific.** UV Photoelectron Spectroscopy. *XPS Simplified.* [Online] [Cited: 08 05, 2020.] https://xpssimplified.com/UPS.php.

8. *On the Velocity of the Cathode Particles Emitted by Various Metals under the Influence of Rontgen Rays, and Its Bearing on the Theory of Atomic Disintegration.* **Innes, P.D.** 532, s.l. : Royal Society, 1907, Vol. 79.

9. **Juarez, A.** *Introduction to hemispherical deflection analysers.* s.l. : AMLaM Group.

10. *Design of electron spectrometers.* **D Roy, D Tremblay.** s.l. : Rep. Prog. Phys., 1990, Vol. 53.

11. **Smith, Graham.** Compositional Analysis by Auger Electron and X-ray Photoelectron Spectroscopy. [book auth.] Sverre Myhra John Riveira. *Handbook of Surface and Interface Analysis: Methods for Problem-Solving.* s.l. : Marcel Dekker.

12. *The Scattering of Electrons by a Single Crystal of Nickel.* **C Davisson, L Germer.** s.l. : Nature, 1927, Vol. 119.

13. *Imrpoved Low Energy Electron Diffraction Apparatus.* **L Germer, C Hartman.** s.l. : Review of Scientific Instruments, 1960, Vol. 31.

14. **Murphy, Barry.** 2.2 Low-energy electron diffraction. *The physico-chemical properties of fullerenes and porphyrin derivatives deposited on conducting surfaces.* 2014.

15. *Influence of Chemisorbed Oxygen on the Growth of Graphene on.* **Z Robinson, E Ong, T Mowll, P Tyagi, D Gaskill, H Geisler, C Ventrice.** s.l. : ACS, 2013, Vol. 117.

VIII Preliminary results of DMMP decomposition on novel metal oxide cluster compositions

VIII.1 Brief History of Chemical Weapons

Although history and lore tell us that chemicals attacks have long been used in war; gases used by the Athenians and Spartans near 431 B.C., “Greek Fire” used by the Christians besieging Constantinople, and then hundreds of years later by the Union army during the American Civil War; it was on the afternoon of April 22, 1915, that the paradigm of war changed forever. (1) At 5pm at Ypres, members of the German army opened valves on thousands of steel cylinders that expelled 160 tons of chlorine gas into the air, where it was swept by the gentle wind over the French trenches, killing thousands. From then until the end of the war, the allies and central powers continued to use chlorine, mustard gas and phosgene in chemical attacks that left up to 90,000 dead and closer to a million injured. Forever after would countries be wary of invisible weapons of mass destruction. For decades after, the US and its allies continued to develop chemical warfare agents (CWAs) as a “deterrent” to other countries. (2)

According to the US government, CWAs were never used in battle following WWI. However, over 60,000 US servicemen were experimentally exposed to Mustard and Lewisite agents, thousands more to other experimental agents, and in at least 9 research projects, the effects of chemicals such as mustard gas was directly tested on servicemen of color to determine how racial differences affected its impact (3). Similarly, the US government does not consider the “rainbow herbicides” such as Agent Orange used extensively in Vietnam as chemical warfare agents and instead as simply defoliants and herbicides, discounting the millions injured by their toxic and carcinogenic properties. Mounting domestic and international pressure to stop the chemical warfare program finally led to a series of US laws passed, starting in 1967, that would limit the development and production of chemical warfare agents. In 1986 the US congress finally ordered the destruction of all remaining chemical warfare agents and the DoD is currently working to destroy the final <10% of the original stockpile. (4) (5)

While the US and much of the world has thankfully woken up to the need to deproliferate weapons of mass destruction such as CWAs, that does not mean that a rogue state or nefarious actor could not use homemade chemicals to deal horrendous damage. For this reason, the research of chemical warfare agents must continue, especially that related to the protection against them and the safe destruction of stockpiles, those existing and to be seized from enemies.

VIII.2 Development of Nerve Agents

In the late 1930's German chemist Gerhard Schrader was working on insecticides when he accidentally discovered tabun, an incredibly toxic chemical that works by interrupting biological nervous systems and was kept secret from the rest of the world. After World War II, it was discovered that Germany was working on a class of organophosphorus CWAs based on tabun (GA), known as the G-agents, and had additionally discovered sarin (GB) and soman (GD) by the wars end. Schrader's research continued after the war and he discovered the last G-agent, cyclosarin (GF), in 1948. While incredibly toxic, the G-agents are volatile, soluble in water, and prone to decomposition via hydrolysis, causing them to not persist long in the environment.

Continued research into the dangerous class of organophosphorus nerve agents (OPNA) at Porton Down in the UK resulted in the discovery of a much more deadly nerve agent, the so-called "venomous agent X" or VX as it became known, the first of the V-agents, in 1952. The USSR quickly developed R-VX as a counter measure, a similarly toxic constitutional isomer of VX. These V agents were an order of magnitude more toxic than the previous G-agents, even though they were based on a similar organophosphorus center (**Figure VIII-I**). Unlike G-agents, V-agents are not water soluble and less prone to hydrolysis, so they tend to persist in the environment, easily building up to harmful thresholds. Throughout the Cold War, the US and others continued to stock nerve agents and pursue experimental research in an arms race that only slowed with the détente of the Cold War and the public pressure regarding the inhumane nature of CWAs. This has not stopped the production and development of CWAs by rogue states, however, demonstrated by high-profile assassinations of Kim Jong-nam using VX and Russian political refugee's Sergei Skripal and his daughter Yulia Skripal with one of the Novichok agents.

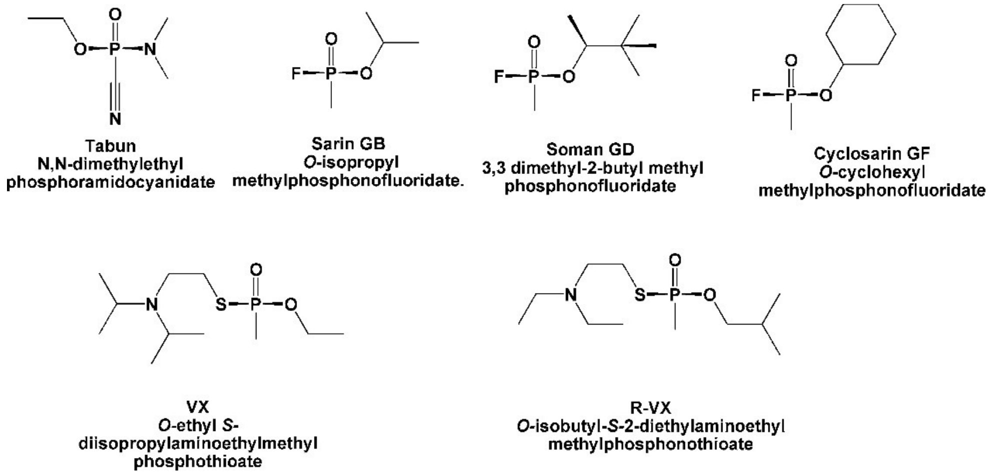

Tabun
N,N-dimethylethyl phosphoramidocyanidate

Sarin GB
***O*-isopropyl methylphosphonofluoridate.**

Soman GD
3,3 dimethyl-2-butyl methyl phosphonofluoridate

Cyclosarin GF
***O*-cyclohexyl methylphosphonofluoridate**

VX
***O*-ethyl *S*-diisopropylaminoethylmethyl phosphothioate**

R-VX
***O*-isobutyl-*S*-2-diethylaminoethyl methylphosphonothioate**

***Figure VIII-I**: Chemical structure of the common OPNAs. (7)*

VIII.2.1 Organophosphorus Nerve Agents

The V-agents and G-agents are both organophosphorus compounds, derivative of phosphonic acid. They have in common a pentavalent phosphorus center doubly bound to a phosphoryl oxygen [=O] and an alkoxy [-O-R] group. Except for Tabun, they all have a methyl group [-CH_3] bound to the phosphorous center as well. The final functional group of the

OPNAs are the “good” leaving group, the identity and nature of which determines the reactivity of the phosphorus center.

The OPNAs’ mechanism of toxicity lies in their ability to inhibit the acetylcholine esterase (AChE) enzyme in human nervous systems. (6) AChE plays an important role regulating the presence of the acetylcholine (ACh) molecule after it has completed its purpose and detached from a signaling receptor. The AChE envelopes the ACh and decomposes it through hydrolysis, binding to a catalytic triad active site containing a serine, histidine and glutamic acid group, decomposing the ACh neurotransmitter at a rate of 10^4 s^{-1}.

OPNAs are able to poison AChE via phosphorylation of the serine group in the triad active site. The pentavalent phosphorus species binds to AChE through nucleophilic attack of the serine’s hydroxyl group on the phosphorus, which is dependent on the departure of the “good” leaving group, X in Figure **VIII-II**. In this state, the enzyme is inhibited but it is not irreversibly poisoned. A final step involving the cleavage of the [PO-R] bond converts the enzyme from the “inhibited enzyme” form to a stable form known as the “aged enzyme” that is irreversibly inactivated toward the regulation of the ACh neurotransmitter. (7)

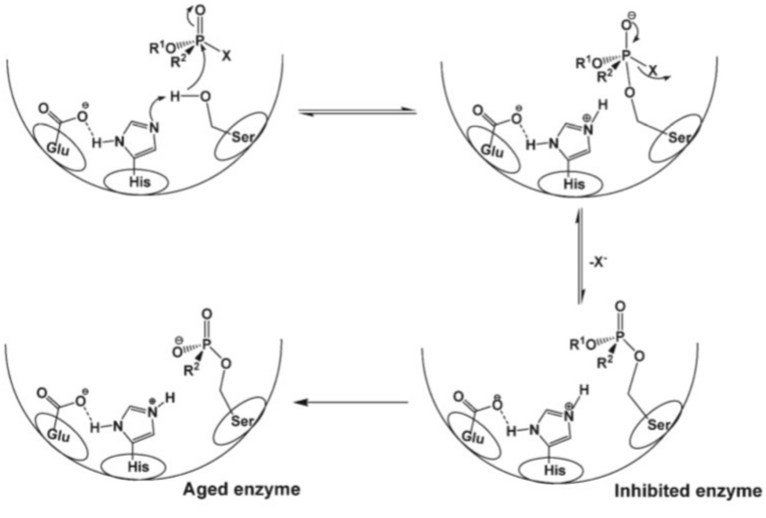

Figure VIII-II*: Route of inactivation for an OPNA destroying the signaling enzyme acetylcholine esterase (AChE). (7)*

Victims of exposure to nerve agents experience loss of muscle control, resulting in seizures, convulsions, paralysis, acute respiratory distress and other less acute symptoms. Nerve agents are fat soluble and absorb through skin, so exposure can occur either through inhalation or skin contact, introducing the nerve agent to the brain, periphera nervous system, muscles and endocrine system, all of which use ACh as a signaling molecule. (6) (8)

VIII.2.2 OPNA Simulant

Because CWAs are incredibly dangerous to handle and are strictly controlled by the U.S. government, it is necessary to find analogues that mimic the reactivity without posing the extreme health risk to researchers. A number of OPNA simulants exist, but the molecule dimethyl methylphosphonate (DMMP) has been historically used in the Bowen lab, and has been shown to closely mimic the physical properties of some OPNAs, especially GB and GD (**Figure VIII-III**). DMMP has a similar structure to the other pentavalent phosphorous OPNAs, but the alkoxy group is shorter than its more dangerous analogs, and the “good” leaving group has been replaced with another methoxy group. The lack of a “good” leaving group means that equilibrium for the nucleophilic attack that inactivates the enzyme is shifted in the direction of the active enzyme. However, DMMP has still been shown to mimic the physical and adsorption properties of OPNAs well, particularly GB (sarin), so it can be a useful tool particularly for finding surfaces that will bind strongly to the phosphorous center, allowing thermal decomposition chemistry to susequently take place. (9)

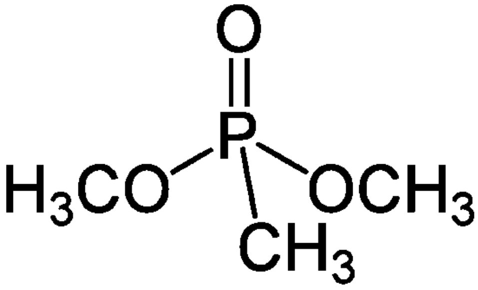

Figure VIII-III: *OPNA simulant dimethyl methylphosphonate (DMMP)*

In order to further confirm/visualize the structure of DMMP, and have a reference point for the binding energy of its electrons, we cooled the sample to -170^{oC} and dosed DMMP into the chamber, creating a frozen matrix of DMMP. The sample was moved into position for XPS and scans were taken of the oxygen 1s and phosphorus 2p envelopes. There are three distinct peaks in the oxygen 1s spectrum (**Figure VIII-IV**: XPS of O 1s region for a frozen matrix of DMMP), as expected from theory. The peak at 532.1 eV is from the oxygen in [P=O], whereas the 534.0 eV peaks is from the oxygen in [P-O-CH_3]. The integrated area ratio between these two oxygen peaks is 1:2, which agrees with the fact that there is one [P=O] for every two [P–O-CH_3] in a DMMP molecule. The oxygen species with an XPS peak at 536.5 eV is residue oxygen on HOPG, which are also seen on HOPG background XPS

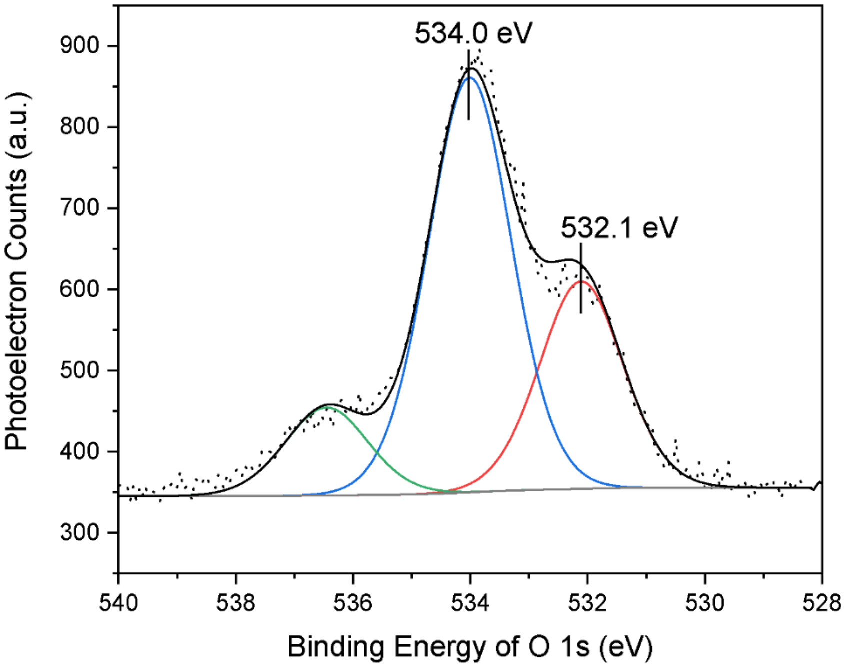

***Figure VIII-IV**: XPS of O 1s region for a frozen matrix of DMMP*

Figure VIII-V: Binding energies of P 2p from XPS measurement on frozen matrix of DMMP on HOPG substrate. shows that the peak binding energy of $P2p_{3/2}$ is 134.2 eV, with the spin orbit splitting expected from the 2p orbital. This binding energy works as a reference to determine how phosphorus will be reduced or oxidized when DMMP decomposes on metal oxide clusters in the future. Unfortunately, problems with contamination of the X-Ray gun has led to a decrease in the ability to perform XPS studies in the last year, work in several new directions should alleviate this.

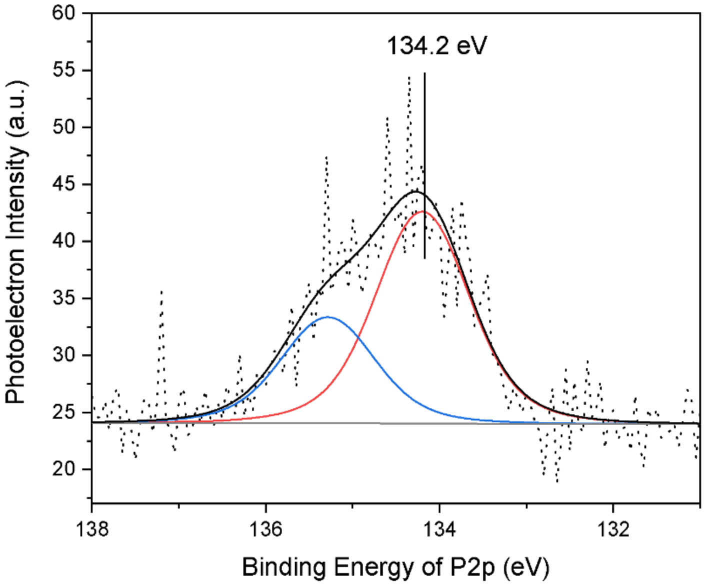

***Figure VIII-V**: Binding energies of P 2p from XPS measurement on frozen matrix of DMMP on HOPG substrate.*

VIII.3 Detoxification of Organophosophorous Nerve Agents

The chemistry of OPNAs have been studied extensively in order to determine reaction pathways that remove the leaving group that makes them destructive to AChE. The pentavalent phosphorous undergoes three characteristic decomposition reactions, hydrolysis, oxidation and adsorptive thermal decomposition (**Figure VIII-VI**). In hydrolysis, the OPNAs react with a water molecule to replace the leaving group with a hydroxyl group, and the alkoxy with a hydrogen, producing an alcohol with the R group from the OPNA and the species HX along with the decomposed OPNA. Hydrolysis can occur in solution or at a surface/gas or surface/liquid interface, forming alcohol products and HX. Oxidation of the OPNA involves a reaction with an oxidizing species that replaces one of the phosphorous functional groups with an oxygen, which will be protonated to an alcohol at most pH values creating the products X^- and RO_x. Finally, adsorptive thermal decomposition is a decomposition route that occurs when OPNA's adsorb strongly to a surface, where they can be decomposed with heat. Acid/base sites on the metal oxide surface can promote the transfer of the OPNAs functional groups to the surface where they may remain. (9) (10)

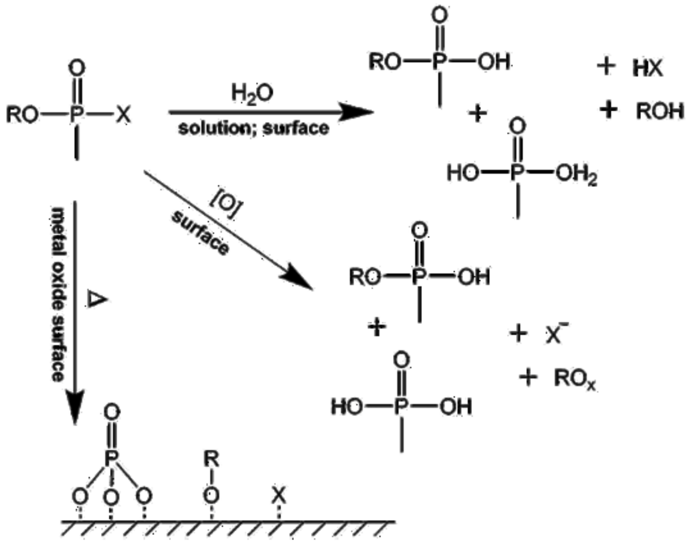

Figure VIII-VI: *Some of the most attractive decomposition reaction pathways for OPNAs. (7)*

An ideal solution for the protection against harmful CWAs would be personal protective equipment that adsorbs the toxic molecules and decomposes them to a form that is not dangerous to people or the environment. In the absence of a material that can be completely regenerated of decomposed CWA's, a replaceable cartridge with reactive metal impregnates distributed in a high surface area zeolite would be adequate. The US government and others have long used a proprietary filter material called ASZM-TEDA which consists of copper, silver, zinc and molybdenum compounds impregnated into an activated carbon bed with triethylenediamine. The high surface area of the material adsorbs high boiling point

OPNAs effectively, and there is thought that the metal impregnates increase the adsorption activity of the carbon zeolite as well as inducing decomposition.

Replaceable ASZM-TEDA filters have become a simple industrial standard for personal protective material, however it would be useful to identify particular metal oxide nanostructures, such as clusters, that are well suited for decomposing or pacifying certain CWAs. Because many metal and metal oxide surfaces and larger nanostructures have been studied for the decomposition of DMMP, but very few studies with size selected clusters, this is a promising application of the cluster deposition instrument.

VIII.4 Experimental Results

Using the new cluster deposition instrument, several metal oxide cluster species have been studied for their ability to adsorb and thermally decompose the OPNA simulant DMMP. In the last two years we have done preliminary studies on tungsten oxide, niobium oxide, and manganese oxide clusters to understand their reactivity toward the decomposition of DMMP. We have also continued the pure metal oxide work done previously with zirconium, copper, and molybdenum oxide clusters by probing the reactivity of mixed copper/molybdenum oxide clusters, and copper/zirconium oxide clusters.

In these studies, the magnetron sputtering source has been used exclusively due to its ability to create the clusters of interest and ion high ion intensity. Before the experiment, the freshly-cleaned, highly oriented pyrolytic graphite (HOPG) surface is frozen and DMMP is dosed onto the surface, creating a “frozen matrix”. Using the frozen matrix method has been shown to increase the number of metal oxide clusters that are able to coordinate with a DMMP and initiate the reaction. While not directly comparable to the process of DMMP adsorbing and decomposing on a surface, it provides a method to concentrate the cluster-DMMP interactions to a magnitude that allows straightforward analysis and suppression of cluster agglomeration.

Metal oxide clusters are formed by the magnetron and transported as a molecular beam to the QMS where they are mass selected and deposited into the frozen matrix of DMMP. After depositing a sufficient quantity of the cluster species of interest, a TPD can be done to study the production of volatile species as a function of temperature, or XPS to confirm the identity of deposited species, and at times, make deductions about the local bonding environment.

VIII.5 Manganese oxide clusters (Mn_xO_y)

Manganese is a group y, monoisotopic transition metal with a $3d^5 4s^2$ valence electron configuration. Manganese is known for having many oxidation states, i.e., compounds with manganese oxidation states from -3 to +7 have been observed, although the most commonly found states are +2, +3, +4, +6, and +7. Various forms of manganese oxide have been studied for their catalytic decomposition properties towards DMMP, showing activity for oxidation and hydrolytic decomposition of DMMP.

Early work by Satayapal et al probed the decomposition of DMMP over amorphous manganese oxide (AMO) and alumina-supported manganese oxide (Mn/Al_2O_3). They found that the AMO decomposed DMMP, forming methanol and CO_2 under air and UV irradiation in the range of 40-70$^{\circ C}$, while ASMO resulted only in CO_2 and at much high temperatures. (11) (12)

Further investigation by Mitchel et al. studied the reaction of DMMP adsorbed to an Mn/Al_2O_3 surface with ozone. They found ozone adsorbed and dissociated to react with DMMP via the Langmuir-Hinshelwood mechanism, forming roughly equal amounts of CO and CO_2. (13) More recently, V. Gupta et al found manganese oxide nanostructures to catalyze the hydrolytic decomposition of DMMP in aqueous media, which correlated with results seen by Prasad et al. regarding the hydrolytic decomposition of GB over AMO nanostructures. (14)

The Bowen lab has continued the investigation of manganese oxide's reactivity toward adsorbed DMMP by depositing size selected Mn_xO_y clusters created *in vacuo* into a frozen matrix of DMMP. By ramping the sample temperature from -170^{oC} to 450^{oC}, we were able to directly to directly measure the intensity of desorbing species and characterize the reaction pathways accessible to DMMP decomposing via adsorptive thermal decomposition.

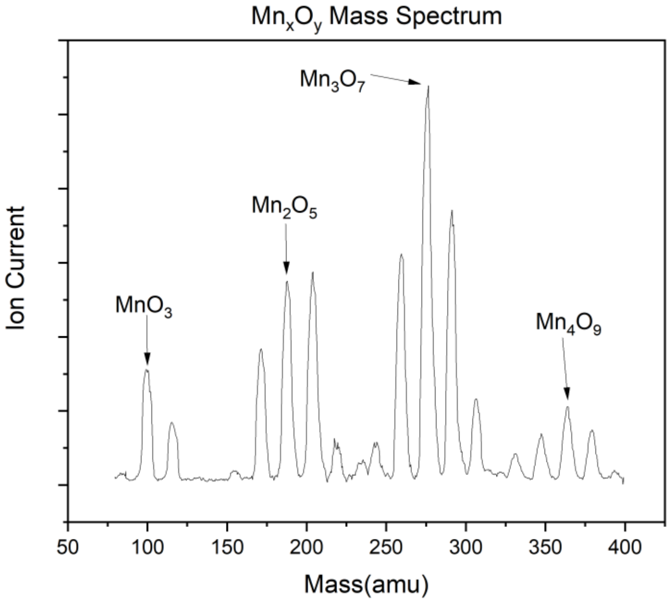

Figure VIII-VII: *Mass spectrum of Mn_xO_y clusters*

To attain a beam intensity that would allow deposition of a sufficient number of clusters over a reasonable time duration, we lowered the resolution of the QMS and allowed a mass region to pass that included the magnesium trimer species Mn_3O_6, Mn_3O_7, and Mn_3O_8.

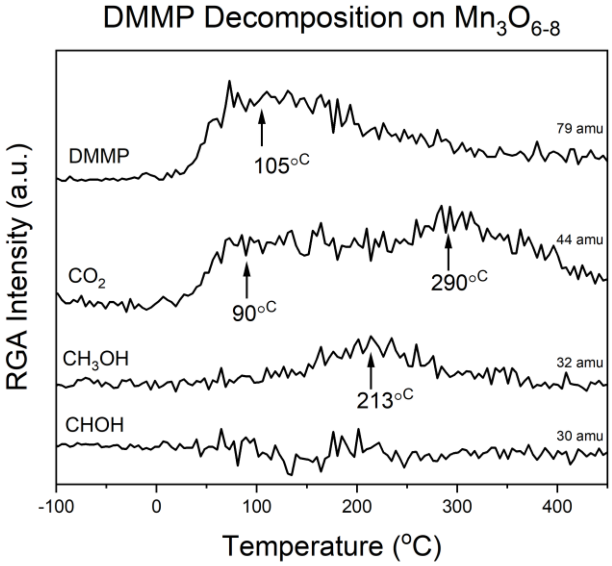

Figure VIII-VIII: *TPD of Mn_3O_{6-8} clusters and DMMP*

Although the results are promising, after only one experiment with Mn_3O_{6-8}, the sputtering target shattered and these studies were temporarily halted without completion at this time. Looking at the background subtracted TPD/R spectrum aquired for the manganese trimer, intact DMMP desorbs at 105^{oC}. The hydrolysis product, methanol, desorbs at 213^{oC} as well as the complete oxidatio product. Carbon dioxide had two desorption peaks, centered at 90^{oC} and 290^{oC}, indicating that total oxidation of adsorbed methoxy groups may be promoted by the manganese oxide clusters, and that there could be two different pathways for the decomposition that results in CO_2 or different oxidation pathways to CO_2..

VIII.6 Tungsten oxide clusters (W_xO_y)

Tungsten is a group 6 transition metal with a $5d^46s^1$ electron configuration, known for having the highest melting point and vapor pressure of all the elements. It is most common found in the oxidation state +6, although it has been made synthetically with oxidation states ranging from -2 to +6. Investigations of metal oxide materials for CWA sensors discovered that WO_3 bound strongly to adsorbed DMMP and decomposed at high temperatures coinciding with the evolution of methanol. (15) The decomposition of DMMP adsorbed to tungsten oxide trimer clusters have previously been studied in the Bowen lab and further demonstrated the binding of DMMP to WO_3 centers, and readily decomposing to evolve methanol at high temperatures.

Previously, the Bowen lab published studies looking at the decomposition of DMMP adsorbed to deposited tungsten trimer clusters, $(WO_3)_3$, however using the mass spectrometer at the time, the beamline mass resolution was 34amu wide at the trimer's mass, 695.5 amu, causing a mix of clusters W_3O_8, W_3O_9, and W_3O_{10} to pass when centered on 695.5 amu. In the new instrument, the QMS mass resolution can be as high as 0.5 amu at that mass range. Using the high resolution of the new QMS, we were able to resolve the neighboring oxygen species and study the decomposition of DMMP with deposited W_3O_9 and W_3O_{10} clusters independently (**Figure VIII-XI**, **Figure VIII-IX**, **Figure VIII-X**).

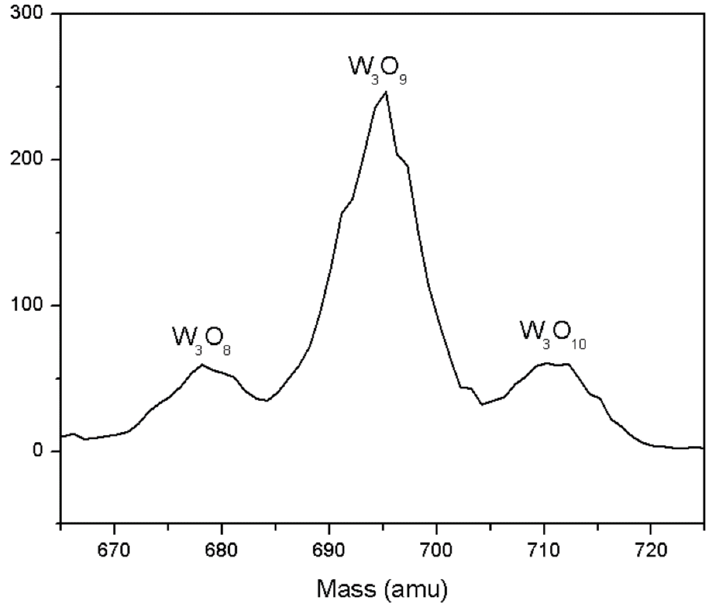

Figure VIII-IX: *Zoomed-in mass spectrum for tungsten oxide trimer, with all conditions optimized for* W_3O_9 *cluster.*

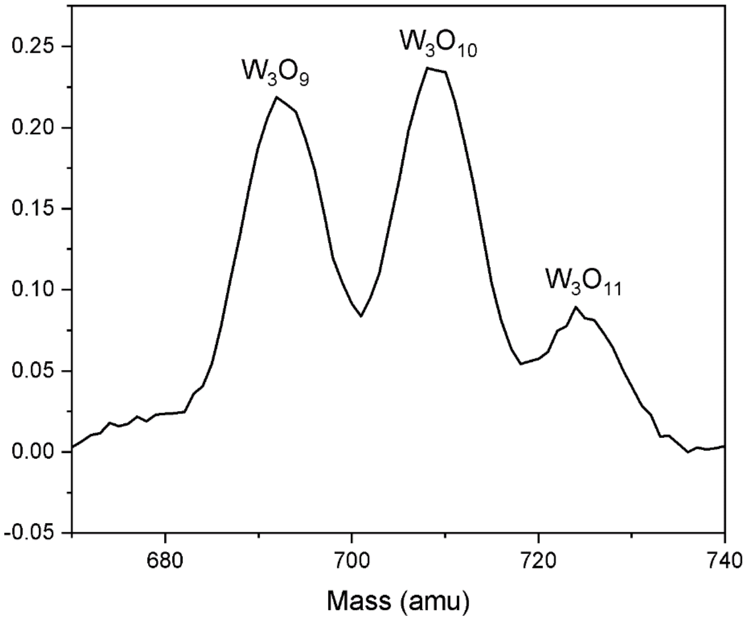

***Figure VIII-X**: Zoomed-in mass spectrum for tungsten oxide trimer, with all conditions optimized for W_3O_{10} cluster*

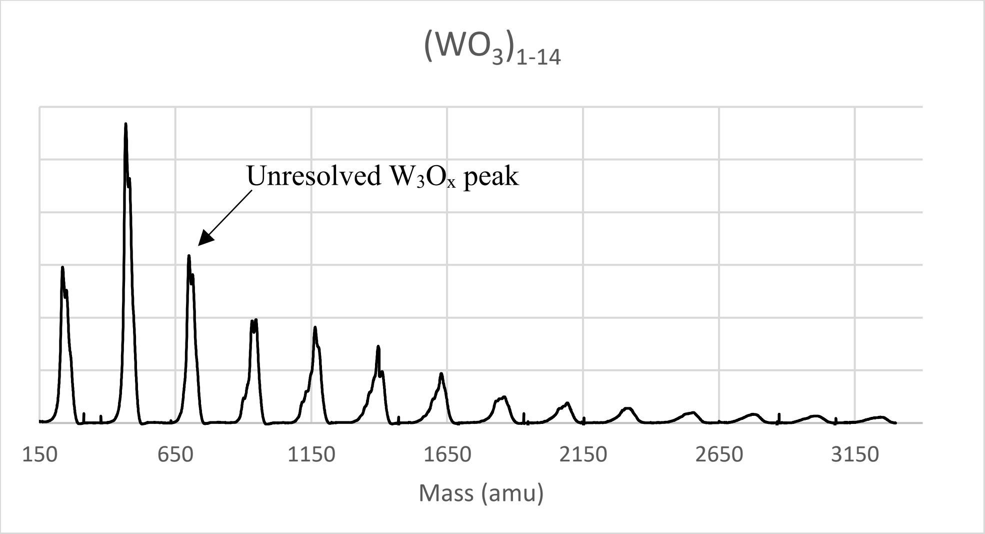

***Figure VIII-XI**: Wide rang mass spectrum of $(WO_3)_n$ clusters, where n=1-14*

In both the W_3O_9 and W_3O_{10} studies, the cluster was deposited into a frozen matrix of DMMP until there was 10% of a monolayer of the tungsten oxide cluster. **Figure VIII-XII** and

Figure VIII-XIII show TPD/R scans for DMMP decomposition on W_3O_9 and W_3O_{10}, respectively. In both cases, the intact DMMP desorbs at a relatively low temperature with peaks near 75^{oC}.. In both cases, methanol appears to desorb with a broad peak centered around 230^{oC}-240^{oC} and there was no sign of the dehydrative recombination product dimethyl ether, and while there is a broad peak and rising background for 29 amu, assumedly CHO^+, there is no peak for its parent molecule formaldehyde at 30 amu, making it unclear whether formaldehyde is produced or whether there may have been a reaction pathway or even a contaminant.

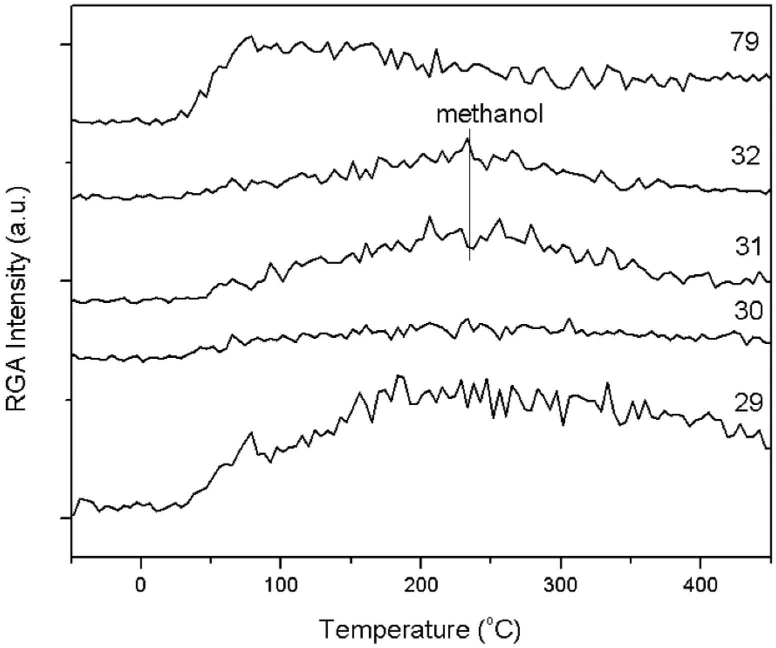

***Figure VIII-XII**: TPD/R scan of DMMP decomposition on W_3O_9 clusters.*

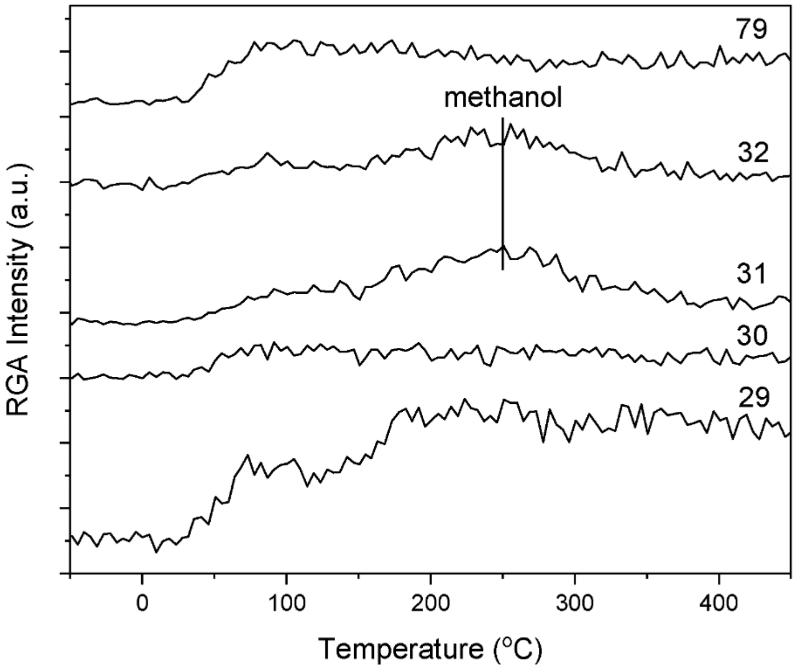

Figure VIII-XIII: *TPD/R scan of DMMP decomposition on W_3O_{10} clusters.*

Based on these preliminary results, there is no clear conclusion to be drawn yet from the differences between W_3O_9 and W_3O_{10} in terms of DMMP decomposition. Recent studies show that stoichiometric W_3O_9 clusters can be viewed as the smallest molecular analog of bulk WO_3, whereas W_3O_{10} can be viewed as replacing a terminal oxygen in W_3O_9 with a peroxo, O_2 unit. High electron binding energies (>7.0 eV) were observed for $W_3O_{10}^-$, suggesting that the W_3O_{10} neutral cluster is an unusually strong oxidizing agent. (16) Therefore, it is expected that reactivity towards DMMP is likely to be very different between W_3O_9 and W_3O_{10} even though there is only one oxygen atom difference. Unfortunately, with the RGA we can only track the desorption of a limited number of possible reaction product species, limiting our view of the situation. In the future, we believe measuring the CO_2 output will be useful to characterize the oxidation activity of the tungsten oxide clusters, as has already been demonstrated with other cluster studies since.

VIII.7 Niobium oxide clusters (Nb_xO_y)

These studies are discussed in depth in Section IX.

VIII.8 Copper molybdenum oxide clusters ($Cu_xMo_yO_z$)

Copper is a group 11 transition metal with a $3d^{10}4s^1$ electron configuration that is widely found in nature, and its useful structural, thermal, and electrical properties have made it an essential material to society. Its oxidation state can vary from +I to IV, although the most commonly found forms are CuO and Cu_2O, in the +II and +I states, respectively. Copper constitutes an important active species in the respiratory enzyme complex cytochrome c oxidase, making it an essential mineral in every living organism's diet. (17) Considering its abundance and continued use in the AZSM-TEDA filters which use metal impregnates with large size distributions, the Bowen lab investigated the decomposition of DMMP on copper and copper oxide clusters. In the unpublished work, we found that copper showed propensity as a species that would promote the chemical decomposition of adsorbed DMMP.

Molybdenum is a group 6 transition metal with a $4d^55s^1$ electron configuration. While the metal is not found naturally occurring, many of its oxidation states are found in minerals, although the +4 and +6 states are most stable and commonly found, such as MoS_2, and MoF_6. Because of the activity of molybdenum in the activation of alkane molecules, (18) the Bowen lab previously studies the adsorption and decomposition of DMMP on $(MoO_3)_3$ clusters. (19) The theoretical and experimental results show that partially reduced, non-stoichiometric clusters may be the active sites of OPNA adsorption and decomposition.

In an early effort to take the experimental capabilities one step further and investigate novel properties, the Bowen lab has pursued the synthesis and study of mixed metal oxide clusters, wherein we may take advantage of multiple advantageous properties at once, or discover emergent properties that did not exist. The first attempt to make mixed metal clusters was with copper molybdenum oxide clusters ($Cu_xMo_yO_z$) due to our past success studying the isolated reactivity of copper and molybdenum oxide clusters independently towards DMMP decomposition.

Because molybdenum and copper do not form a stable alloy, there is no single sputtering target that will generate $Cu_xMo_yO_z$ species. Early investigations included two approaches to creating mixed metal oxide cluster ions in the abundance needed for cluster ion studies. In one, conductive Cu/Mo disks were made through the sintering of copper and molybdenum powder a spark plasma sintering synthesis machine as part of a collaboration with the Hopkins Extreme Materials Institute. While the results were promising and we are currently working on a system to take better advantage of this capability, not every metal powder composition resulted in a solid target that would hold up in the harsh conditions of the magnetron sputtering source. In a second approach, we simply cut pure metal targets in half and loaded them into the magnetron target holder.

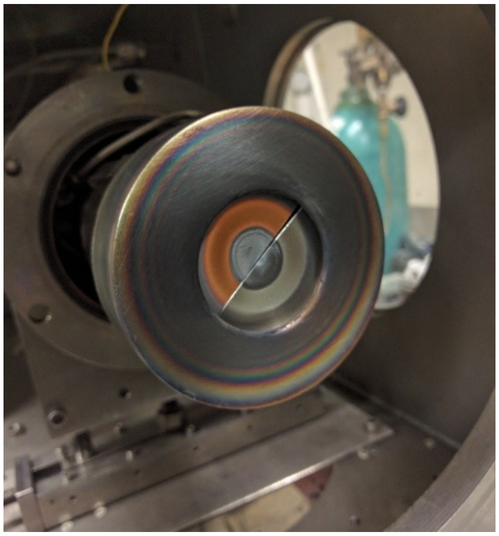

Figure VIII-XIV*: Copper and molybdenum "half moon" targets loaded into the magnetron sputtering source head*

The metal halves were cut by a professional so that they would match up into a nearly perfect circle, and they were placed on top of a copper plate in order to prevent sputtering the steel through the crack between the metal "half-moons". Mass spectra taken for a cluster beam generated with the copper/molybdenum mixed targets are shown in **Figure VIII-XV** and **Figure VIII-XVI**, where careful consideration of possible species must be done in order to correctly identify the species created.

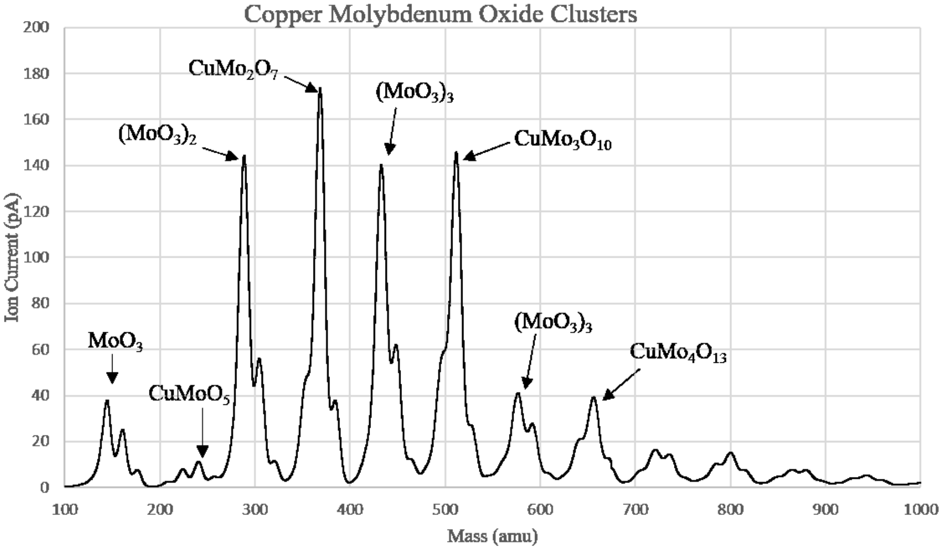

Figure VIII-XV: *Wide range mass spectrum of Cu/Mo oxide beam showing* $Cu_xMo_yO_z$ *and* MoO_x *clusters*

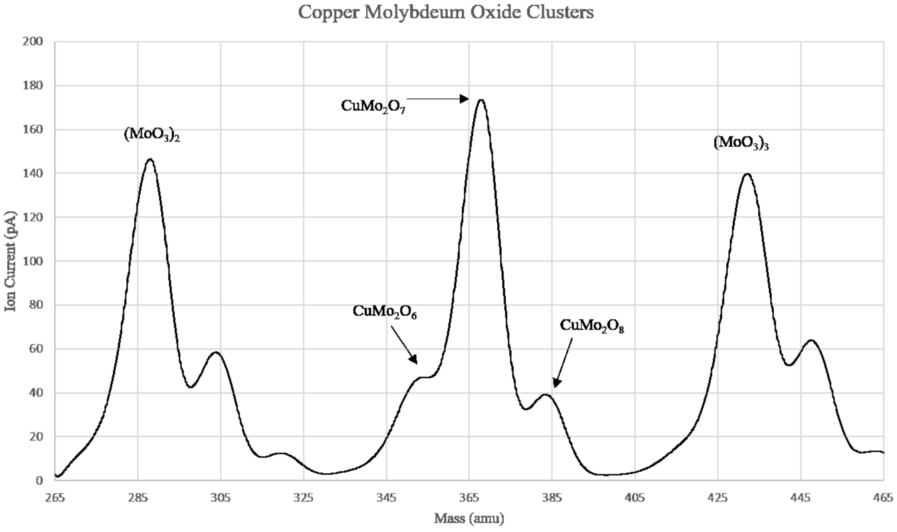

Figure VIII-XVI*: Higher resolution mass spectrum zoomed in on the cluster of interest,* $CuMo_2O_6$

The XPS shown in **Figure VIII-XVII** shows why mixed metal clusters, in this case copper and molybdenum can offer such novel reactivity. In the XPS of the Mo 3d orbital, for a pure molybdenum system, $(MoO_3)_3$, the right peak is centered at 232.5 eV, as expected for the +6 oxidation state of the $(MoO_3)_3$ species. However, in the XPS of the same electron orbital of the $CuMo_2O_6$, a system with the same number of metal atoms and oxygens, one molybdenum has been replaced with a more electropositive copper atom, and the other two molybdenum atoms are then observed in a slightly reduced state. This reduction of the molybdenum atoms is indicated by the shift in binding energy of the right peak of the Mo 3d orbital, from 232.5 to 231.7, as electron density is added to the molybdenum, the binding energy of its electrons is shifted slightly lower (**Figure VIII-XVII**).

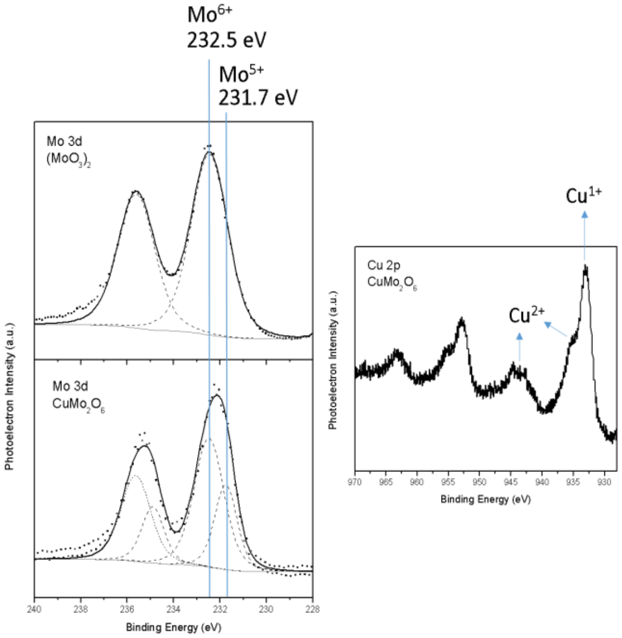

***Figure VIII-XVII**: In-situ XPS of Mo 3d for deposited $(MoO_3)_2$ and $CuMo_2O_6$ clusters(left and of Cu 2p envelope(right)*

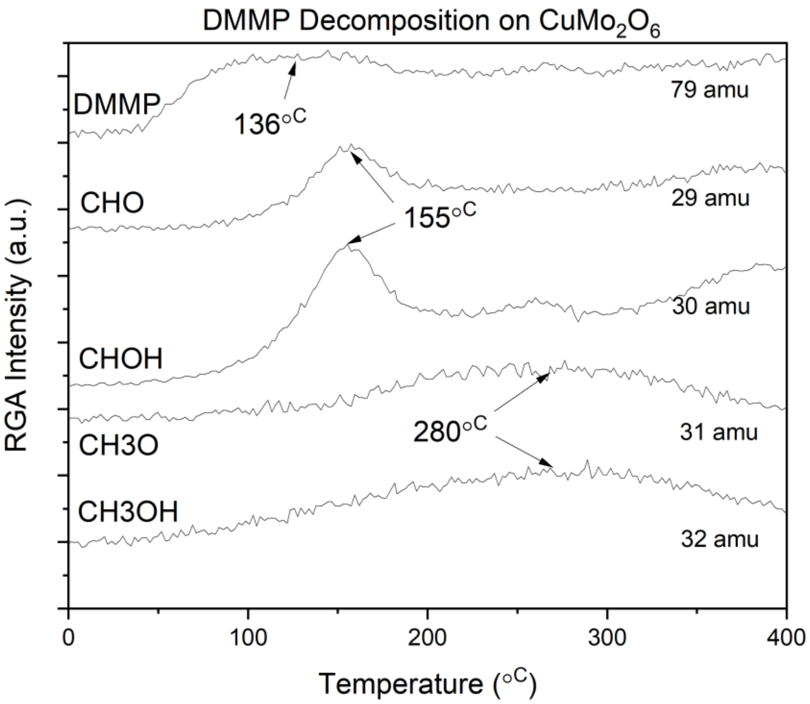

***Figure VIII-XVIII**: TPD of DMMP and $CuMo_2O_6$ on clean HOPG*

The decomposition of DMMP when exposed to $CuMo_2O_6$ clusters was investigated via TPR/D (**Figure VIII-XVIII**). In this spectrum, the contribution to methanol and formaldehyde from DMMP fragmenting in the RGA has been calibrated and subtracted out. Intact DMMP that has not bound to a metal center desorbs broadly with a peak centered at roughly 136^{oC}. The major fragments of formaldehyde indicate a peak desorption centered at 155^{oC}, showing that the $CuMo_2O_6$ has some oxidation capability. Formaldehyde was not a detected product in previous Cu_x, CuO_x, and MoO experiments, which is especially interesting. In the previous study on $(MoO_3)_3$, however, the desorption of methanol is centered 200^{oC}, whereas on $CuMo_2O_6$, the desorption of DMMP is centered at 280^{oC}, which demonstrates that the substitution for the copper atom could reduce the reaction barrier for the hydrolysis decomposition pathway. No dimethyl ether was detected, and unfortunately, CO_2 was not yet tracked in our studies at this point.

VIII.9 Copper Zirconium Oxide clusters

Zirconium is a group 4 transition metal with a $4d^2 5s^2$ valence electron configuration and can be found with formal oxidation states ranging from +II to +IV. Unpublished worked by the Bowen lab demonstrates that $(ZrO_2)_3$ clusters provide strong adsorption sites for DMMP, possibly due to the high Lewis acidity of zirconium's +IV oxidation state. Bulk zirconium(IV) hydroxide has recently been shown to promote the decomposition of several CWAs including GD via hydrolysis, thought to be catalyzed by basic OH groups from $Zr(OH)_4$ rather than acidic surface hydroxyls. (20) A hydroxylated zirconium oxide hexamer metal center has also shown promising results as a hydrolytically active species in a series of metal organic frameworks (MOFs) for the decomposition of OPNA simulants. The more recent MOF studies were initially motivated by the similarity in structure between the bridging Zn-OH-Zn active sites in a phosphotriesterase enzyme and the analogous Zr-OH-Zr sites found in the 6-metal node. (21) Due to the promising properties zirconium seems to have in mediating the decomposition reaction of adsorbed OPNAs and their simulants, and the promising results from mixed metal oxide clusters to fine tune electronic properties of the clusters, the Bowen lab decided to study the decomposition of DMMP with deposited copper zirconium oxide clusters, $Cu_xZr_yO_z$.

Similar to the copper molybdenum oxide mixed metal clusters, the copper zirconium clusters were generated via reactive magnetron sputtering by placing two metal halves in the magnetron In **Figure VIII-XIX**, a mass spectrum shows some of the mixed metal clusters that we generated in our molecular beamline apparatus. Because the cluster ion current was relatively low for each of the individual cluster stoichiometries, the resolution was lowered and a mixture of oxidation states for the same metal center was deposited, in this case Cu_2ZrO_3, Cu_2ZrO_4 and Cu_2ZrO_5, as well as the analogous clusters with one extra copper atom, i.e. Cu_3ZrO_{3-5} (**Figure VIII-XIX**).

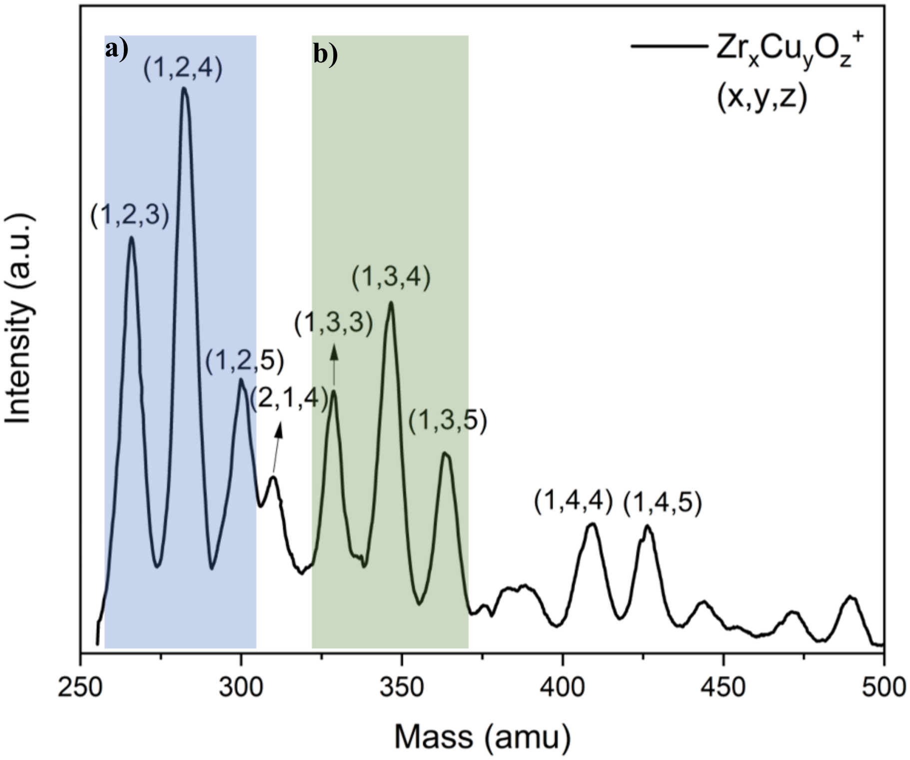

***Figure VIII-XIX**: Mass spectrum of copper zirconium oxide clusters with $ZrCu_2O_{3\text{-}5}$ (a) and $ZrCu_3O_{3\text{-}5}$ (b) highlighted*

In order to confirm the identity of the copper zirconium clusters that are identified in the mass spectrum, an XPS was taken of the deposited Cu_3ZrO_6, that shows the approximate peak envelopes expected for copper and zirconium atoms in mixed oxidation states (**Figure VIII-XX** and **Figure VIII-XXI**).

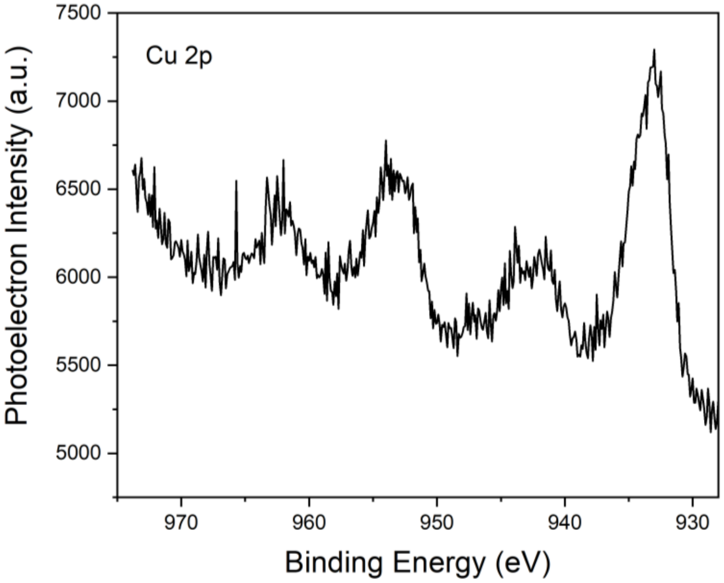

Figure VIII-XX*: XPS spectra of Cu 2p envelope from* Cu_3ZrO_6

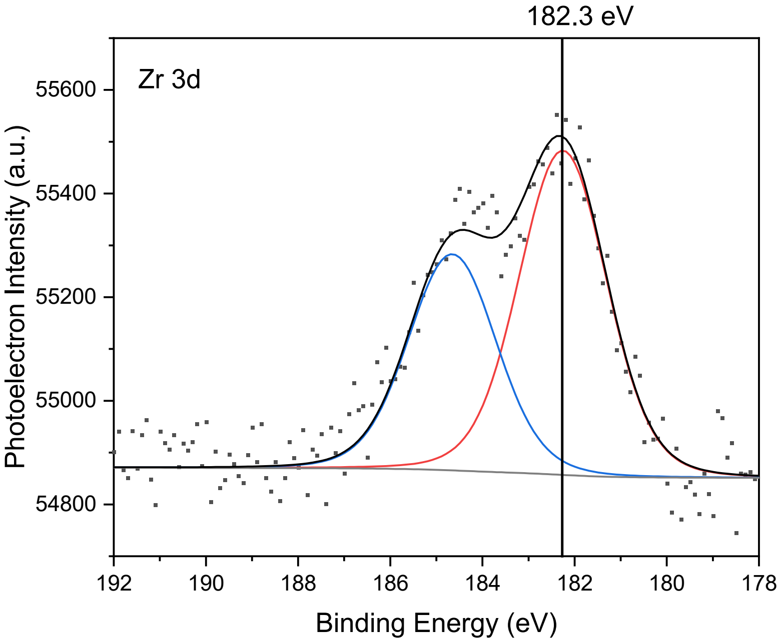

Figure VIII-XXI*: XPS spectra of Zr 3d envelope from* Cu_3ZrO_6

The mixed metal species Cu_2ZrO_{3-5} and Cu_3ZrO_{3-5} were successively deposited into frozen HOPG deposited on freshly cleaned HOPG. After depositing approximately 10% of a monolayer of one of the cluster species into frozen DMMP, a TPR/D of the surface is taken in order to observe the decomposition of DMMP that binds to metal oxide clusters. Comparing the desorption spectra of the two deposited species, $Cu_2ZrO_{3\text{-}5}$ and $Cu_3ZrO_{3\text{-}5}$, there is evidence of composition dependent chemistry, illustrating once again the fact that every atom matters.

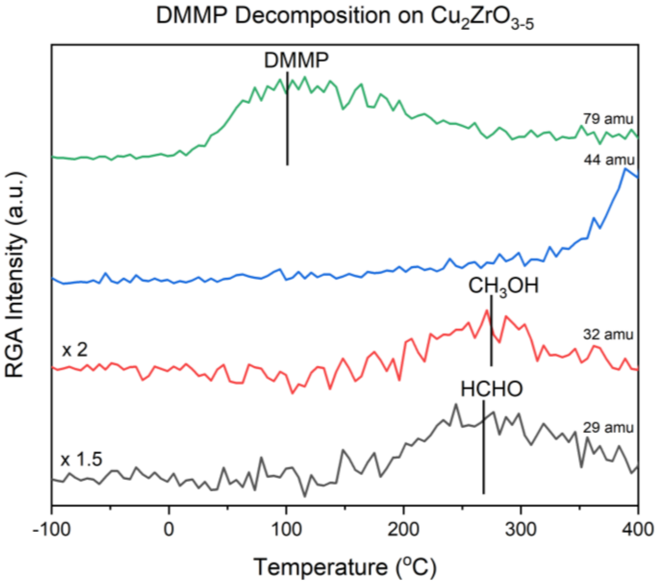

***Figure VIII-XXII**: TPD/R profiles for DMMP adsorbed to $Cu_2ZrO_{3\text{-}5}$ supported on HOPG*

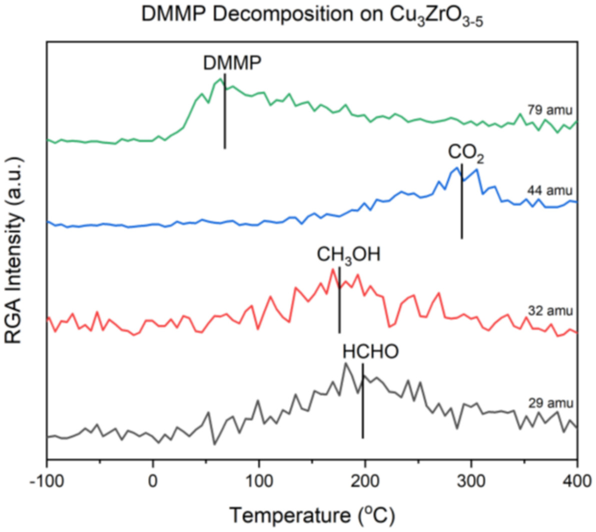

***Figure VIII-XXIII**: TPD/R profiles for DMMP adsorbed to $Cu_3ZrO_{3\text{-}5}$ supported on HOPG*

The TPD/R spectra for $Cu_2Zr_1O_{3-5}$ (**Figure VIII-XXII**) shows the desorption of methanol is observed near 275°C, with a desorption peak for formaldehyde at roughly the same temperature. The formation of formaldehyde coincidentally with methanol indicates that the rated determining step is the hydrolysis of DMMP resulting in surface bound methoxy species that can either desorb as is, or become oxidized to formaldehyde and then desorb. The spectrum shows a rising background of CO_2 that could indicate a high temperature CO_2 desorption peak, and bears further analysis.

In the TPD/R spectra for $Cu_3Zr_1O_{3-5}$ (**Figure VIII-XXIII**), the peak desorption of methanol is observed near 190°C indicating there is the potential for adsorbed DMMP to decompose hydrolytically. The presence of formaldehyde also desorbing with a peak near 200°C shows that some of the hydrolytically cleaved methanol will be partially oxidized to formaldehyde, and at a still higher temperature, some of those surface methoxy species are then completely oxidized to CO_2 which shows a desorption peak near 290°C.

References

1. *Chemical Warfare. A Course in the Study of Toxic Gases.* **Wells, C. F.** 8, s.l. : Journal of Chemical Education, 1928, Vol. 5.

2. *Chemical Warfare and Medicla Responce During World War I.* **Fitzgerald, G. J.** 4, s.l. : American Journal of Public Health, 2008, Vol. 98.

3. *Mustart Gas and American Race-Based Human Experimentation in World War II.* **Smith, Susan.** 3, s.l. : Journal of Law, Medicine & Ethics, 2008, Vol. 36.

4. **National Academy of the Sciences.** *Institute of Medicine: Committee to Survey the Health Effects of Mustart Gas and Lewisite: Veterans at Risk: Health Effects of Mustard Gas and Lewisite.* Washington DC : s.n., 1993.

5. *Military Chemical Warfare Agent Human Subjects Testing: Part 1 - History of Six-Decades of Military Experiments With Chemical Warfare Agents.* **Brown, Mark.** s.l. : Military Medicine, 2009, Vol. 174.

6. *Toxicity of the Organophosphate Chamical Warfare Agents GA, GB and VX: Implications for Public Protection.* **N Munro, K Ambrose, A Watson.** 1, s.l. : Enviornmental Health Perspectives, 1993, Vol. 102.

7. *Destruciton and Detection of Chemical Warfare Agents.* **K Kim, O.G. Tsay, H.O. Lutz and D.G. Churchill.** s.l. : Chem Rev., 2011, Vol. 111.

8. **P. Taylor, S. Camp, Z Radic.** *Encyclopedia Neuroscience.* s.l. : Elsevier, 2009.

9. *Decontamination of Chemical Warfare Agents.* **Y. Yang, J. Baker, J. Ward.** s.l. : Chemical Review, 1992, Vol. 92.

10. —.**B Singh, G Prasad, K Pandey, R Danikhel, R Vijayaraghavan.** 4, s.l. : Defence Science Journal, 2010, Vol. 60.

11. *Photoassistem Decomposition of Dimethyl Methylphosphonate over Amorphous Manganese Oxide Catalysts.* **S.R. Segal, S.L. Suib, X Tang, and S. Satyapal.** s.l. : J. Catalysis, 1999, Vol. 11.

12. *Thermal Decomposition of Dimethyl Methylphosphonate over Manganese Oxide Catalysts.* **S.R. Segal, L. Cao, S.L. Suib, X. Tang, and S. Satyapal.** s.l. : J. Catalysis, 2001, Vol. 198.

13. *Sustained Roomo Temperature Decomposition of Methyl Methylphosphonate (DMMP) by O3 on Alumina-Supported MnOx.* **M.B. Mitchell, V.N. Sheinker et al.** s.l. : J. Phys C, 2011, Vol. 115.

14. *Decontamination of 2-chloro ethyl ethyl sulphide and dimethyl methyl phosphonate from aqueous solutions using manganese oxide nanostructures.* **M Verma, R. Chandra, V.K. Gupta.** s.l. : J. Mol. Liq., 2016, Vol. 215.

15. *An Infrared Study of Adsorbed Organophosphonates on Silica: A prefiltering Strategy for the detection of Nerve Agents on Metal Oxide Sensors.* **Tripp, S. Kanan and C.** s.l. : Langmuir, 2001, Vol. 17.

16. *On the Structure and Chemical Bonding of Tri-Tungsten Oxide Clusters W3On- and W3On (n = 7−10): W3O8 As A Potential Molecular Model for O-Deficient Defect Sites in Tungsten Oxides.* **X Huang, Hua-Jin Zhai, Jun Li, Lai-Shen Wang.** 1, s.l. : J Phys Chem A, 2006, Vol. 110.

17. *Mitochondrial Copper Metabolism and Delivery to Cytochrome c Oxidase.* **D Horn, A. Barrientos.** 7, s.l. : IUBMB Life, 2008, Vol. 60.

18. *Mechanisms of Methane Activation and Transormation on Molylbdenum Oxide Based Catalysts.* **Fu, G.** 11, s.l. : Journal of the American Chemical Society, 2005, Vol. 127.

19. *Adsorption and decomposition of dimethyl methylphosphonate on size-selected (MoO3)3 clusters.* **X Tang, Z Hicks, L Wang, Kit Bowen, et al.** s.l. : Physical Chemistry Chemical Physics, 2018, Vol. 7.

20. *Reactions of VX, GD, and HD with Zr(OH)4: Near Instantaneous Deconamination of VX.* **T. Bandosz, M. Laskoski, J. Mahle et al.** 21, s.l. : J Phys Chem C, 2012, Vol. 116.

21. *Instantaneous Hydrolysis of Nerve-Agent Simulants with a Six-Connected Zirconium-Based Metal-Organic Framework.* **S.Y. Moon, Y Liu, J Hupp, O. Farha.** 23, s.l. : Angewandte Chemie, 2015, Vol. 54.

IX TPD Study of DMMP Decomposition on Size-Selected Nb3Ox Clusters Supported on HOPG

Nicolas Blando[1], Linjie Wang[1], Michael Denchy[1], Lucas Hansen[1], Zach Hicks[1], Xin Tang[1], and Kit H. Bowen[1*]

[1] Department of Chemistry, Johns Hopkins University, Baltimore, Maryland, 21218, USA

Due to the development of toxic nerve agents that unfortunately find continued use in both traditional and non-traditional warfare, the development of materials for personal protective equipment that can effectively protect the wearer from dangerous chemical warfare agents is extremely important. Due to past studies on the utility of ultra-small clusters towards the selective decomposition of organophosphorus nerve agents, as well as independent studies of the highly nucleophilic nature of polyoxoniobates and their derivatives, the reactivity of ultra-small niobium oxide clusters was investigated for the decomposition of a common nerve agent simulant dimethyl methylphosphonate, and the effects of increasing oxygen content on that reactivity. It was discovered that niobium oxide effectively adsorbed the organophosphorus nerve agent simulant DMMP and facilitated its decomposition at high temperature, assumed to be through the general mechanism of base hydrolysis that was shown elsewhere. Analyzing the desorption trends of decomposition products, trends regarding the dehydrogenation by-products of initial DMMP decomposition were discovered, and it was found that the full oxidation of reaction products to CO_2 was only possibly for the overoxidized species, and afterwards reactivity continued to increase with increasing overoxidation of the metal center.

IX.1 Introduction

Modern warfare is an everchanging landscape that offers unseen perils, especially in the form of biological and chemical weapons. Proper support for the men and women in the possible path of chemical warfare agent use by nefarious actors requires developing and improving the personal protective equipment to meet the ever-changing demands chemical warfare agent protection.[1] Organophosphorus nerve agents (OPNAs) constitute one of the most widely used and most lethal classes of chemical warfare agents (CWAs),[2] and their continued use in both traditional military encounters as well as global acts of terrorism and authoritarian control require the development of materials that can be used to protect against such a threat. Directed development towards materials that can immobilize and/or safely decompose dangerous CWAs would not only be useful for integration into protective equipment but could be used in sensors to actively monitor areas for the presence of dangerous species.

The difficulty in developing such materials lies in the inherent complexity of the system at hand, where an ideal material can preferentially adsorb and selectively decompose hazardous CWAs, as well as strongly bind any toxic by-products of the decomposition, so as not to risk exposing the user to other dangerous species. These requirements pose several technical challenges, for instance, a material that adsorbs extremely well may bind so strongly that physiologically inert by-products remain bound to the surface, quickly poisoning active sites to the continued decomposition of the CWA. On the other hand, a material that could easily desorb inert by-products after enabling some reaction on the surface, might not interact strongly enough with the CWA itself to adsorb it to an appreciable extent.

Understandably, the development of a robust solution to the problem at hand requires a fundamental understanding of the species involved and the reaction mechanisms.

Furthermore, the danger involved with live nerve agents necessitates the use of a safer analog that might be used in a civilian laboratory environment. When developing materials for the purpose of decomposing toxic OPNAs, the nerve agent simulant dimethyl methylphosphonate (DMMP) is widely used, especially in surface chemistry applications, and notably for studying the adsorption behavior of sarin (GB). In **Figure IX-I**, one can see the structural similarities between DMMP and sarin. Both contain a phosphorus center, double bonded to an oxygen and single bonded to a methyl although the other two functional groups differ.

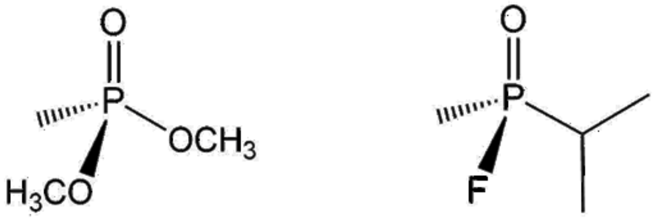

Figure IX-I: *Chemical structure of DMMP (left) and sarin (right)*

The majority of gas masks are still made with the same material and operating principle as they were in WWI, where activated charcoal was widely used in cartridges to widely adsorb dispersed molecules in the air, protecting the user from inhaling toxic chemicals. The downside of this method is that it is not selective, leading to the adsorption of a broad range of species, and does not employ any chemistry to decompose toxic species, pacifying them simply by a nonreversible absorption.

An advance that has been made on these basic activated carbon filters, has been to take advantage of the interesting acid, base and redox chemistry available to transition metal oxides.[5] In contemporary gas masks meant to selectively filter CWAs, materials such as ASZM-TEDA, wherein activated carbon is impregnated with copper-, molybdenum-, zinc-, and silver-oxide particles along with thriethylene diamine, are used to offer an increased protection over the traditional activated carbon.[6] Indeed, the literature provides many studies on the decomposition properties of transition metal oxides against CWAs. Some of the first studies to show promising results investigated the absorption and decomposition over single crystal surfaces such as Mo(110), Ni(111), Pd(111), Pt(111), and Rh(100).[7-10] Following these initial successes, DMMP's adsorption and reactivity towards a number of bulk transition metal oxide species, including Al_2O_3,[11,12] Cu_2O,[13] CuO,[14] Fe_2O_3,[15] FeO_x,[16] MgO,[17] MnO_x,[18] MoO_3,[19,20] TiO_2,[21–24] and WO_3[25], continued to demonstrate the utility of transition metal oxide towards the adsorption and decomposition of toxic CWAs. Others have reported on the decomposition properties of Cu, Ni, Pt, Au, and Au-Pt clusters supported on TiO_2(110),[32-32] as well as previous work from this group investigating DMMP decomposition of molybdenum oxide trimer and tungsten oxide trimer clusters, supported on a highly oriented pyrolytic graphite (HOPG) substrate.[34,35]

Working off the related success of polyoxometalates towards the decomposition of blistering agents, some thought to use the basic nature of polyoxoniobates (PONbs) to decompose the nerve agents via base hydrolysis. PONbs are the most basic of known polyoxometalates due to their high charge density, in an aqueous solution, each niobium cluster center was shown to bind up to three protons.[35] In particular, the hexaniobate ion, $[Nb_6O_{19}]^{8-}$, also known as the Lindqvist ion, is the most widely studied of PONbs, as it is very stable and easily synthesized in a lab.[36] Recent work has shown its utility towards the decomposition of similar nerve agent simulants,[35-40] and in this paper, we will isolated the niobium oxide trimer anion which has a similar formal oxidation state, and study the reactivity of the cluster as a function of oxidation state by changing the number of oxygens bound to the niobium trimer. The work reported here represents the first study of mass-selected ultra-small niobium oxide clusters towards the decomposition of nerve agent simulants such as DMMP.

IX.1.1 VIII.2 Experimental Methods

IX.1.2 VIII.2.1 Apparatus

A schematic of our apparatus is presented in **Figure IX-II**. Niobium oxide clusters were produced using a reactive sputtering magnetron source by mounting a metallic niobium disk in front of a permanent magnet (N42 Neodymium magnet, 4,300 Gauss measured directly in front of the magnetron head), and seeding an argon containing gas mixture in front of the target while a large voltage bias is applied to the magnetron head. The previous iteration of this instrument was limited to the magnetron sputtering source; however, the instrument upgrade introduced the flexibility of a laser vaporization source and pulsed arc ionization source. Argon ions formed and accelerated toward the sputtering target eject metal ions and neutrals into a discharge plasma in front of the magnetron head

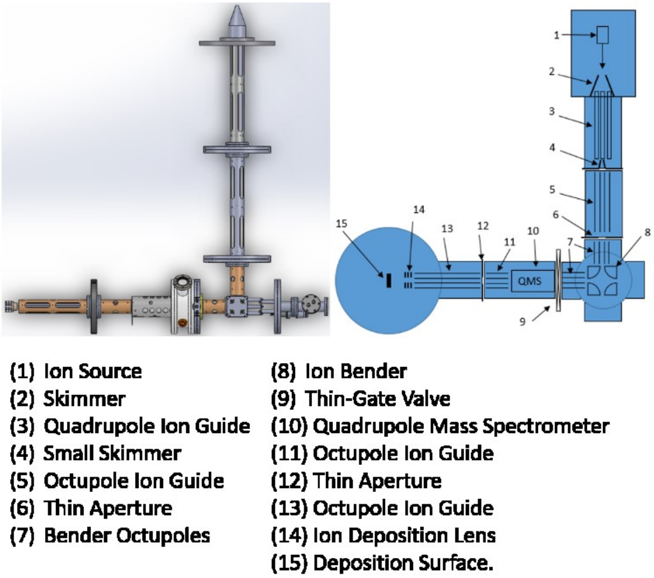

Figure IX-II *Schematic of the apparatus, showing only the ion optics on the left, and on the right are shown housed in their respective vacuum chambers*

Ions and neutrals created by the magnetron are carried down the beamline by their initial kinetic energy and are then collimated by a skimmer on the way out of the source chamber. Ions passing through the skimmer encounter a potential energy well created by the multi-pole RF ion guides. A quadrupole ion guide has a narrower potential well and is placed directly after the source chamber to confine the ion beam. After the initial quadrupole, octupoles are used to transport the created cluster ions down the length of the beamline instrument.

After transport through a series of multi-pole ion guides, the clusters encounter an electrostatic bender. Here, the direction of charged particles can be changed, allowing the user to filter out neutrals and ions of the chosen polarity. In our bender, ions with the selected charge polarity are bent 90° by the electrostatic bender.

After the electrostatic bender, traveling ions encounter the inline quadrupole mass spectrometer (QMS). With a resolution of $M/\Delta M=1000$, this QMS is able to resolve 1 amu differences for masses up to 1000 amu. Following the QMS, the ion beam contains only the species of interest and is focused by a lens into a final series of octupole ion guides. After exiting the final octupole ion guide, the ions pass through a thin plate lens to focus the ions onto the sample target, which is inside the final analytical region of the instrument.

The sample itself is mounted on the end of a sample column mounted on an XYZR sample stage. By filling the column with liquid nitrogen, the sample can be cooled to cryogenic temperatures. The sample, a 1cm x 1cm piece of highly oriented pyrolytic graphite (HOPG), is mounted between two copper leads with pieces of tantalum foil such that current can be driven through the sample for resistive heating, and its temperature manipulated anywhere between -173 °C to 500 °C.

In order to introduce reactants of interest, we use a high precision needle dosing valve to introduce a static background of gas pressure into the chamber. Depending on the temperature of the sample, the length of the dose and the interaction between the dosed molecules and the surface, some amount of the dosed sample will absorb to the surface. Reactants can in principle be dosed before, during, or after deposition of size selected clusters from the main beamline.

Size selected cluster ions focused by the final electrostatic lens are soft-landed(<1 eV/atom) onto the grounded HOPG surface, where they lose their charge and become neutral. The rate of deposition is proportional to the current from sample to ground, due to singly-charged cluster ions losing their charge. Therefore, the sample coverage can be easily determined in real time by accurately measuring and integrating the current from sample to ground.

The analysis region of the apparatus is maintained at ultra-high vacuum pressures in the region of $1*10^{-9}$ torr. Mounted on the analysis region are a number of instruments to probe the sample and reactions taking place on it. Available, but not used in this experiment, are Low Energy Electron Diffraction and *in-situ* Scanning Tunneling Microscopy techniques, as well as a hemispherical electron energy analyzer to measure the binding energy of electrons in the sample, ejected with either the incident X-Ray or Ultraviolet photon source.

In addition to the other analysis instruments, the analysis region boasts a high resolution RGA (Hiden HAL/3F PIC), in which an electron bombardment ionizer in tandem with a QMS and dedicated pulse-counting electron multiplier detector are brought extremely close to the sample in order to monitor the intensity of species desorbing from the surface. In a temperature programed desorption/reaction (TPD/R) experiment, the temperature of the sample is increased linearly while reaction products desorbing from the surface are detected via the RGA. By quantifying the peak desorption temperature, it is possible to compare apparent activation energies of reactions.

IX.1.3 Cluster Synthesis / Sample Preparation

Niobium oxide trimer cluster anions $(Nb_3O_x)^-$ with three different numbers of oxygen were synthesized via reactive magnetron sputtering of a niobium metal target (Kurt J. Lesker) using a gas mixture consisting of argon, helium and oxygen, the exact composition of which helps to direct the oxidation state and size of synthesized clusters. The actual sputtering is performed by argon atoms from the gas mixture that are ionized and then accelerated towards the niobium disk by an electrostatic bias applied to the metal target, in this case 340V-352V, adjusted during the day to maintain the cluster deposition current and cluster distribution. Fast moving argon ions hit the metal target and generate a discharge plasma, which then cools, and in doing so, condenses into clusters and picks up oxygen molecules present in the seed gas. The as-synthesized niobium oxide cluster anions are then transported through the beamline, and a single cluster species is selected and allowed to pass by the QMS, and then can then be soft landed onto the prepared sample.

The substrate, a 1cm x 1cm HOPG sample, is cleaned with mechanical exfoliation (scotch tape method) followed by a 20 minute anneal at 500 °C in UHV. Then, the DMMP sample was purified with three successive freeze-pump-thaw cycles using an ice bath and an attached rotary vane pump. The purification steps help to remove water and take advantage of its slightly higher vapor pressure to do so.

Before depositing clusters of interest, the HOPG sample is cooled to -173 °C and DMMP is dosed into the chamber in order to create a frozen matrix of DMMP on the sample surface. This frozen multilayer of DMMP can be maintained throughout the cluster deposition process in order to 1) maximize the interaction between deposited clusters and DMMP molecules, and 2) to minimize the agglomeration that ultra-small clusters tend to undergo on surfaces, migrating towards islands and defects through a number of mechanisms.

After cooling the sample to -173 °C, the sample was exposed to a 0.2 Langmuir dose (L, 10^{-6} torr·s) in order to form the frozen matrix of DMMP. Niobium oxide cluster anions ($Nb_3O_8^-$, $Nb_3O_9^-$, and $Nb_3O_{10}^-$) were each successively deposited into a fresh DMMP frozen matrix on HOPG, in order to probe the decomposition of DMMP absorbed to the niobium oxide clusters.

IX.2 Results

IX.2.1 Nb_3O_8

After depositing 5% of a monolayer of Nb_3O_8 into a frozen matrix of DMMP held at -173 °C, the sample was annealed at 25 °C for 2 minutes to allow physisorbed DMMP to desorb. Afterwards, the sample is cooled to -173 °C again, before approaching it to the RGA and inducing a linear temperature ramp from -173 °C to 500 °C at a rate of 2 °C/s. Any species desorbing from the sample surface are detected and tracked with the RGA.

The TPD in **Figure IX-III** shows desorbing product intensity as a function of temperature. If possible, the two major fragments for each species are tracked, in many cases the minor fragment is the same species minus a proton, which could be lost in the RGA's ionization process. The spectra clearly indicate low temperature desorption of intact DMMP and higher temperature desorption of decomposition products methanol, formaldehyde and dimethyl ether.

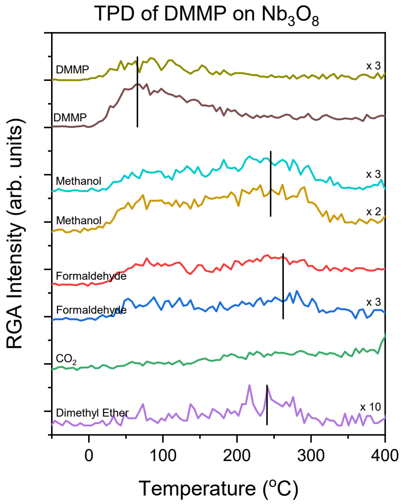

***Figure IX-III:** Unprocessed TPD of DMMP with Nb3O8 supported on DMMP*

The major DMMP fragment shows a clear desorption peak at ~67 °C. These peaks are attributed to the molecular desorption of DMMP that was chemisorbed to the Niobium clusters as well as the possibly the Ta foil clips or Cu leads of the sample holder. Sharp onset peaks could indicate a single prevalent desorption motif, which would probably be that of chemisorbed DMMP on the metal oxide clusters.

After subtracting the contribution of intact DMMP to the traces for methanol and formaldehyde major fragments, they were plotted again and individually fit with gaussian peaks to help determine the peak max. The TPD displayed in **Figure IX-IV** shows that methanol and dimethyl ether both have high temperature desorption at 234 °C. The major methanol peak fragment, the deprotonated methanol, has a peak intensity of roughly half of the DMMP desorption peak. The DME peak has an intensity of about a tenth of that of DMMP.

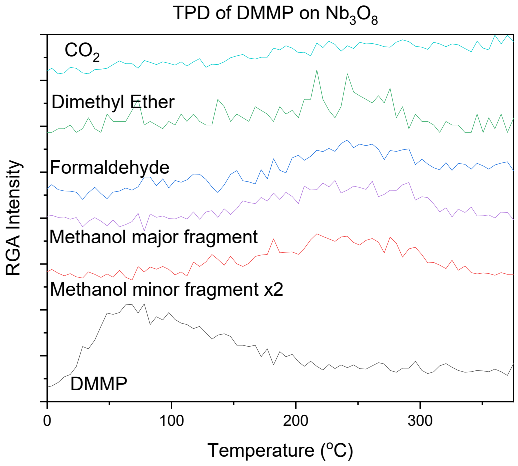

***Figure IX-IV**: TPD of DMMP on Nb_3O_8. Major DMMP desorption and decomposition products shown*

The contribution of formaldehyde to the spectra from the fragmentation of intact DMMP was determined and subtracted similarly to methanol. The major fragment of formaldehyde shows a strong peak centered at ~252 °C. The intensity of the formaldehyde peak is 62% of the max DMMP desorption intensity. There is no indication of a maximum desorption temperature peak for CO_2, merely a rising background.

IX.2.2 Nb_3O_9

The TPD procedure performed for the TPD of DMMP on Nb_3O_8 was repeated for Nb_3O_9, and the relevant data is shown in **Figure IX-V**.

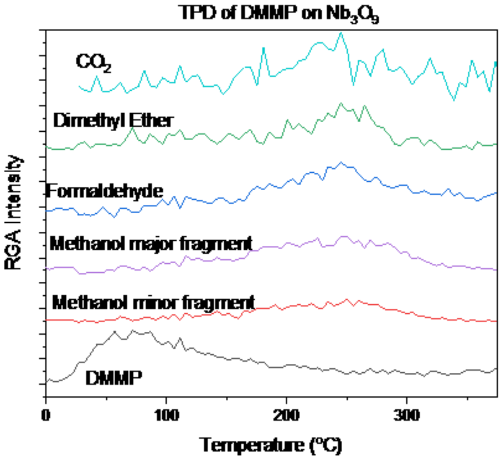

Figure IX-V *Background subtracted TPD of Nb_3O_9 clusters and DMMP supported on HOPG*

The data has been corrected by subtracting the contribution of electron bombardment induced fragmentation of DMMP. Like before, peaks were individually fitted with a gaussian distribution to help identify the point of max desorption. The major fragment of DMMP shows a clear desorption peak at ~70 °C. These peaks are attributed to the molecular desorption of DMMP that was chemisorbed to the niobium clusters.

Methanol and formaldehyde show a peak desorption at 246 °C. The major methanol peak fragment has a peak intensity of roughly half of the DMMP desorption peak. The intensity of the formaldehyde peak is roughly 82% of the DMMP peak.

After subtracting the linear, rising background of CO_2 for visibility, its trace indicates a desorption peak at 237 °C. The intensity of the CO_2 desorption peak is about 28% of that of the DMMP peak. The dimethyl ether trace shows a clear desorption peak at 243 °C. The dimethyl ether desorption peak intensity is about 10% of the DMMP desorption peak.

IX.2.3 Nb_3O_{10}

The TPD procedure for Nb_3O_8 was repeated for Nb_3O_{10} clusters deposited into a frozen matrix of DMMP, after the low temperature anneal, the sample temperature was ramped at 2 °C/s from -173 °Cto 500 °C, and the relevant data is plotted below in **Figure IX-VI**.

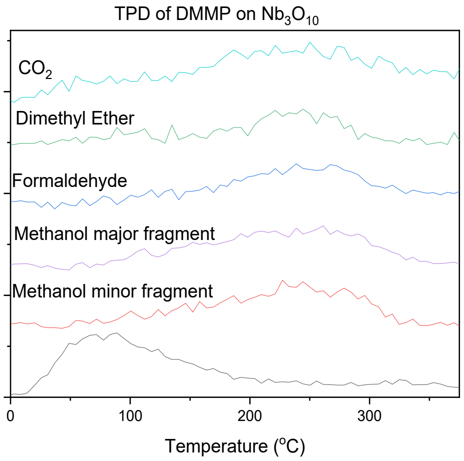

Figure IX-VI *:Background subtracted TPD of Nb_3O_{10} and DMMP supported on HOPG*

Since Methanol and formaldehyde are minor fragments of intact DMMP fragmentation in the RGA, that contribution was once again quantified and subtracted out. Similarly, peaks were fit with gaussian's to help determine the peak desorption temperature.

The DMMP fragments show a desorption peak centered at ~85 °C. These peaks are attributed to the molecular desorption of DMMP that was chemisorbed to the Niobium clusters or possibly the Ta foil or Cu clips. Methanol and formaldehyde show a peak desorption at 246℃, similar to Nb_3O_9. The major methanol fragment has a peak intensity of roughly 66% of the DMMP desorption peak. The major formaldehyde fragment has a peak intensity of ~62% of the DMMP peak.

After linear background subtraction for CO_2, its trace indicates a desorption peak at 235°C. The intensity of the CO_2 desorption peak is about 53% of that of the DMMP peak. The dimethyl ether trace shows a clear desorption peak at 243 °C. The dimethyl ether desorption peak intensity is about 10% of the DMMP desorption peak.

IX.2.4 Shifting peaks

As the number of oxygens in the cluster is increased, a few trends emerge. As seen in Figure IX-VII, for the less oxidized state, the peak desorption temperature of formaldehyde begins at a high temperature and shifts to lower temperatures when more oxygens are added to the metal center; although the temperature shift is small and could be within the room for erro, it is worth investigating.

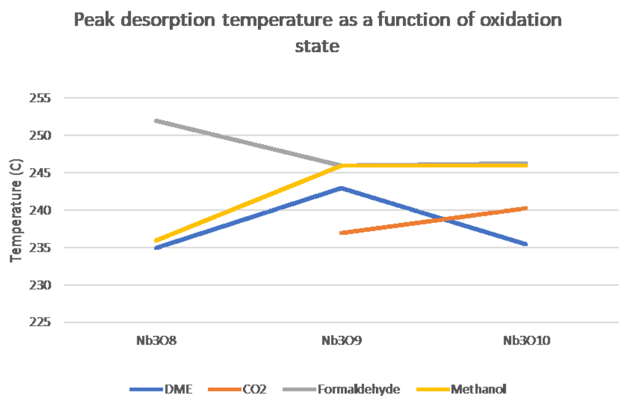

Figure IX-VII: *Peak desorption temperature for each species as a function of changing oxygen content*

Similarly, the methanol desorption peak begins at a lower temperature and rises with increasing oxidation state, until it matches the desorption temperature of formaldehyde. Dimethyl ether's peak desorption first goes up, and then back down to near the original temperature.

Finally, CO_2 shows no desorption for the fully oxidized niobium oxide, but begins to for the first over-oxidized species, and afterward the peak desorption temperature increases with increasing oxidation number.

IX.3 Growing peaks

As oxygen atoms are added to the cluster, the relative intensity of desorption products changes. Shown in **Figure IX-VIII**, methanol and formaldehyde track together, they show a rise in relative peak intensity from Nb_3O_8 to Nb_3O_9, and then a final decrease at Nb_3O_{10}.

On the other hand, the CO_2 desorption trends indicate a constantly rising peak intensity, from no CO_2 peak detected, to roughly half of the DMMP peak intensity. The intensity of dimethyl ether remained relatively constant throughout the experiment.

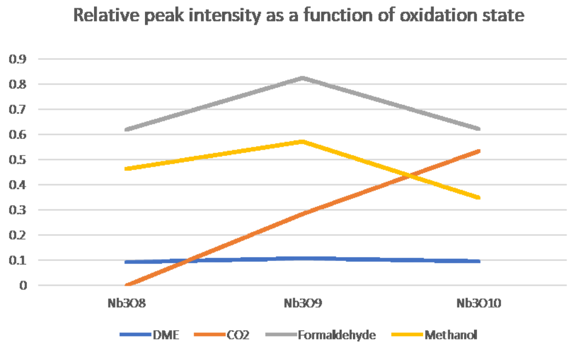

Figure IX-VIII*: Graph of relative peak intensity as a function of the changing oxygen content. Ratio of decomposition product peak height to DMMP max desorption height.*

As the number of oxygens increases above 8, the desorption of decomposition product formaldehyde decreased, while the desorption temperature of methanol remained relatively constant, increasing slightly.

While there was no clear trend for the dehydration product dimethyl ether, we see indication that the CO_2 desorption peak shifts to higher temperatures after seeing no production with the fully oxidized cluster.

IX.3.1 Conclusion

In this investigation, we saw the decomposition of DMMP when forced to interact with Nb_3O_{8-10} clusters via the frozen matrix method. As the oxidation state changed from a less oxidized state to successively overoxidized, we saw the increase in desorption temperature of methanol matched by a decrease in desorption temperature of formaldehyde. Similarly, while we saw no sign of CO_2 formation with the least oxidized cluster, we saw large increases in CO_2 product desorption with each of the successively oxidized species, mirrored by increasing peak desorption temperatures. This is likely due to the increasingly nucleophilic nature of the niobium oxide clusters driving a complete oxidation reaction.

Corresponding Author

*E-mail: kbowen@jhu.edu

References

1. Kim, K.; Tsay, O. G.; Atwood, D. A.; Churchill, D. G. Destruction and Detection of Chemical Warfare Agents. *Chem. Rev.* **2011**, *111* (9), 5345–5403. https://doi.org/10.1021/cr100193y.
2. Munro, N. B.; Ambrose, K. R.; Watson, A. P. Toxicity of the Organophosphate Chemical Warfare Agents GA, GB, and VX: Implications for Public Protection. *Environ. Health Perspect.* **1994**, *102* (1), 18–38.

3. Yang, Y. C.; Baker, J. A.; Ward, J. R. Decontamination of Chemical Warfare Agents. *Chem. Rev.* **1992**, *92* (8), 1729–1743. https://doi.org/10.1021/cr00016a003.

4. Ekerdt, J. G.; Klabunde, K. J.; Shapley, J. R.; White, J. M.; Yates, J. T. Surface Chemistry of Organophosphorus Compounds. *J. Phys. Chem.* **1988**, *92* (22), 6182–6188. https://doi.org/10.1021/j100333a005.

5. Park, S. H.; McClain, S.; Tian, Z. R.; Suib, S. L.; Karwacki, C. Surface and Bulk Measurements of Metals Deposited on Activated Carbon. *Chem. Mater.* **1997**, *9* (1), 176–183. https://doi.org/10.1021/cm9602712.

6. Morrison, R. W. *NBC Filter Performance*; U.S. Army Soldier and Biological Chemical Command: Aberdeen Proving Ground, MD, 2001.

7. Hegde, R. I.; Greenlief, C. M.; White, J. M. Surface Chemistry of Dimethyl Methylphosphonate on Rh(100). *J. Phys. Chem.* **1985**, *89* (13), 2886–2891. https://doi.org/10.1021/j100259a035.

8. Henderson, M. A.; White, J. M. Adsorption and Decomposition of Dimethyl Methylphosphonate on Platinum(111). *J. Am. Chem. Soc.* **1988**, *110* (21), 6939–6947. https://doi.org/10.1021/ja00229a002.

9. Smentkowski, V. S.; Hagans, P.; Yates, J. T. Study of the Catalytic Destruction of Dimethyl Methylphosphonate: Oxidation over Mo(110). *J. Phys. Chem.* **1988**, *92*, 6351–6357.

10. Guo, X.; Yoshinobu, J.; Yates, J. T. Decomposition of an Organophosphonate Compound (Dimethyl Methylphosphonate) on the Ni(111) and Pd(111) Surfaces. *J. Phys. Chem.* **1990**, *94* (17), 6839–6842. https://doi.org/10.1021/j100380a054.

11. Templeton, M. K.; Weinberg, W. H. Adsorption and Decomposition of Dimethyl Methylphosphonate on an Aluminum Oxide Surface. *J. Am. Chem. Soc.* **1985**, *107* (1), 97–108. https://doi.org/10.1021/ja00287a018.

12. Aurian-Blajeni, B.; Boucher, M. M. Interaction of Dimethyl Methylphosphonate with Metal Oxides. *Langmuir* **1989**, *5* (1), 170–174.

13. Trotochaud, L.; Head, A. R.; Büchner, C.; Yu, Y.; Karslıoğlu, O.; Tsyshevsky, R.; Holdren, S.; Eichhorn, B.; Kuklja, M. M.; Bluhm, H. Room Temperature Decomposition of Dimethyl Methylphosphonate on Cuprous Oxide Yields Atomic Phosphorus. *Surf. Sci.* **2019**, *680*, 75–87. https://doi.org/10.1016/j.susc.2018.10.003.

14. Trotochaud, L.; Tsyshevsky, R.; Holdren, S.; Fears, K.; Head, A. R.; Yu, Y.; Karslıoğlu, O.; Pletincx, S.; Eichhorn, B.; Owrutsky, J.; Long, J.; Zachariah, M.; Kuklja, M. M.; Bluhm, H. Spectroscopic and Computational Investigation of Room-Temperature Decomposition of a Chemical Warfare Agent Simulant on Polycrystalline Cupric Oxide. *Chem. Mater.* **2017**, *29* (17), 7483–7496. https://doi.org/10.1021/acs.chemmater.7b02489.

15. Henderson, M. A.; Jin, T.; White, J. M. A TPD/AES Study of the Interaction of Dimethyl Methylphosphonate with Iron Oxide a-Fe2O3 and SiO2. *J. Phys. Chem.* **1986**, *90* (19), 4607–4611. https://doi.org/10.1021/j100410a027.

16. Hegde, R. I.; White, J. M. Interaction of Dimethyl Methylphosphonate with Oxidized Iron and the Effect of Coadsorbed Water. *Appl. Surf. Sci.* **1987**, *28*, 1–10.

17. Mitchell, M. B.; Sheinker, V. N.; Mintz, E. A. Adsorption and Decomposition of Dimethyl Methylphosphonate on Metal Oxides; 1997.

18. Segal, S. R.; Cao, L.; Suib, S. L.; Tang, X.; Satyapal, S. Thermal Decomposition of Dimethyl Methylphosphonate over Manganese Oxide Catalysts. *J. Catal.* **2001**, *198*, 66–76. https://doi.org/10.1006/jcat.2000.3126.

19. Head, A. R.; Tsyshevsky, R.; Trotochaud, L.; Yu, Y.; Kyhl, L.; Karslıoğlu, O.; Kuklja, M. M.; Bluhm, H. Adsorption of Dimethyl Methylphosphonate on MoO3: The Role of Oxygen Vacancies. *J. Phys. Chem. C* **2016**, *120* (51), 29077–29088. https://doi.org/10.1021/acs.jpcc.6b07340.

20. Head, A. R.; Tang, X.; Hicks, Z.; Wang, L.; Bleuel, H.; Holdren, S.; Trotochaud, L.; Yu, Y.; Kyhl, L.; Karslıoğlu, O.; Fears, K.; Owrutsky, J.; Zachariah, M.; Bowen, K. H.; Bluhm, H. Thermal Desorption of Dimethyl Methylphosphonate from MoO3. *Catal. Struct. React.* **2017**, *3* (1), 112–118. https://doi.org/10.1080/2055074X.2017.1278891.

21. Rusu, C. N.; Yates, J. T. Adsorption and Decomposition of Dimethyl Methylphosphonate on TiO2. *J. Phys. Chem. B* **2000**, *104* (51), 12292–12298. https://doi.org/10.1021/jp002560q.

22. Kim, C. S.; Lad, R. J.; Tripp, C. P. Interaction of Organophosphorous Compounds with TiO2 and WO3 Surfaces Probed by Vibrational Spectroscopy. *Sensors Actuators, B Chem.* **2001**, *76*, 442–448. https://doi.org/10.1016/S0925-4005(01)00653-0.

23. Zhou, J.; Varazo, K.; Reddic, J. E.; Myrick, M. L.; Chen, D. A. Decomposition of Dimethyl Methylphosphonate on TiO 2 (110): Principal Component Analysis Applied to X-Ray Photoelectron Spectroscopy. *Anal. Chim. Acta* **2003**, *496*, 289–300. https://doi.org/10.1016/S0003-2670(03)01008-0.

24. Trubitsyn, D. A.; Vorontsov, A. V. Experimental Study of Dimethyl Methylphosphonate Decomposition over Anatase TiO2. *J. Phys. Chem. B* **2005**, *109* (46), 21884–21892. https://doi.org/10.1021/jp053793q.

25. Kanan, S. M.; Lu, Z.; Tripp, C. P. A Comparative Study of the Adsorption of Chloro- and Non-Chloro-Containing Organophosphorus Compounds on WO3. *J. Phys. Chem. B* **2002**, *106* (37), 9576–9580. https://doi.org/10.1021/jp014647x.

26. Verma, M.; Chandra, R.; Gupta, V. K. Decontamination of 2-Chloro Ethyl Ethyl Sulphide and Dimethyl Methyl Phosphonate from Aqueous Solutions Using Manganese Oxide Nanostructures. *J. Mol. Liq.* **2016**, *215*, 285–292. https://doi.org/10.1016/j.molliq.2015.12.039.

27. Šťastný, M.; Tolasz, J.; Štengl, V.; Henych, J.; Žižka, D. Graphene Oxide/MnO 2 Nanocomposite as Destructive Adsorbent of Nerve-Agent Simulants in Aqueous Media. *Appl. Surf. Sci.* **2017**, *412*, 19–28. https://doi.org/10.1016/j.apsusc.2017.03.228.

28. Gordon, W. O.; Tissue, B. M.; Morris, J. R. Adsorption and Decomposition of Dimethyl Methylphosphonate on Y2O3 Nanoparticles. *J. Phys. Chem. C* **2007**, *111* (8), 3233–3240. https://doi.org/10.1021/jp0650376.

29. Bisio, C.; Carniato, F.; Palumbo, C.; Safronyuk, S. L.; Starodub, M. F.; Katsev, A. M.; Marchese, L.; Guidotti, M. Nanosized Inorganic Metal Oxides as Heterogeneous Catalysts for the Degradation of Chemical Warfare Agents. *Catal. Today* **2016**, *277*, 192–199. https://doi.org/10.1016/j.cattod.2015.12.023.

30. Ma, S.; Zhou, J.; Kang, Y. C.; Reddic, J. E.; Chen, D. A. Dimethyl Methylphosphonate Decomposition on Cu Surfaces: Supported Cu Nanoclusters and Films on TiO 2 (110). *Langmuir* **2004**, *20*, 9686–9694. https://doi.org/10.1021/la048594x.

31. Zhou, J.; Ma, S.; Kang, Y. C.; Chen, D. A. Dimethyl Methylphosphonate Decomposition on Titania-Supported Ni Clusters and Films: A Comparison of Chemical Activity on Different Ni Surfaces. *J. Phys. Chem. A* **2004**, *108*, 11633–11644. https://doi.org/10.1021/jp040185m.

32. Ratliff, J. S.; Tenney, S. A.; Hu, X.; Conner, S. F.; Ma, S.; Chen, D. A. Decomposition of Dimethyl Methylphosphonate on Pt, Au, and Au-Pt Clusters Supported on TiO2(110). *Langmuir* **2009**, *25*, 216–225. https://doi.org/10.1021/la802361q.

33. Tang, X.; Hicks, Z.; Wang, L.; Ganteför, G.; Bowen, K. H.; Tsyshevsky, R.; Sun, J.; Kuklja, M. M. Adsorption and Decomposition of Dimethyl Methylphosphonate on Size-Selected (MoO3)3 Clusters. *Phys. Chem. Chem. Phys.* **2018**, *20*, 4840–4850. https://doi.org/10.1039/c7cp08427g.

34. Tang, X.; Hicks, Z.; Ganteför, G.; Eichhorn, B. W.; Bowen, K. H. Adsorption and Decomposition of DMMP on Size-Selected (WO 3) 3 Clusters. *ChemistrySelect* **2018**, *3* (13), 3718–3721. https://doi.org/10.1002/slct.201800229.

35. Kinnan, Mark K., et al. "Nerve agent degradation with polyoxoniobates." European Journal of Inorganic Chemistry 2014.14 (2014): 2361-2367.

36. Nyman, May. "Polyoxoniobate chemistry in the 21st century." Dalton Transactions 40.32 (2011): 8049-8058.

37. Black, Jay R., May Nyman, and William H. Casey. "Rates of Oxygen Exchange between the [H x Nb6O19] 8-x (aq) Lindqvist Ion and Aqueous Solutions." Journal of the American Chemical Society 128.45 (2006): 14712-14720.

38. Alam, Todd M., et al. "Multinuclear NMR investigations of the oxygen, water, and hydroxyl environments in sodium hexaniobate." Journal of the American Chemical Society 126.17 (2004): 5610-5620.

39. Chapleski Jr, Robert C., et al. "Reaction Mechanism of Nerve-Agent Hydrolysis with the Cs8Nb6O19 Lindqvist Hexaniobate Catalyst." The Journal of Physical Chemistry C 120.30 (2016): 16822-16830.

40. Wang, Qi, et al. "Atomic-level structural dynamics of polyoxoniobates during DMMP decomposition." Scientific reports 7.1 (2017): 1-8.

Curriculum vitae

Nicolas Blando • (915)861-8080 • Nicgblando@gmail.com

Education

- Johns Hopkins University
  - *MA Chemistry*, 8/2018; GPA- 3.7/4.0
  - *PhD Chemistry*, 8/2020; GPA – 3.7/4.0
- Texas A&M University
  - *B.S. Chemical Engineering* 5/2014; GPA- 3.3/4.0
  - *Minor - Chemistry*

Related Work Experience

- Johns Hopkins University Baltimore, MD **- PhD Research;** 11/2014 - present
  - Collaborated on the design, construction, operation and troubleshooting for multiple custom molecular beam apparatus's, supported the implementation of unique set-ups for several ultra-high vacuum techniques including mass spectrometry, photodetachment spectroscopy, temperature programed desorption, scanning tunneling microscopy, atomic force microscopy, etc.
  - Implemented instrument improvements such as home-built RF generators, an upgraded emission current regulator, molecular flow dosing, automated data acquisition systems, laser optic set-ups and redesigned ion sources.
  - Studied the size-dependent properties of ultra-small clusters deposited via molecular beam sputtering, analyzing not only the topography and composition of deposited monolayers, but also the electronic structure and reactivity via several UHV techniques.
- Cyclotron Institute College Station, TX - **Research Assistant**; 4/2012–8/2014
  - Contributed to the design of a novel ionization chamber particle detector used in the search for new super-heavy elements.
- Skills: Proficient with Windows and Office, popular Linux distributions, Simion LabVIEW, Matlab, AutoCAD, SolidWorks, VBA, Java, C & C++, Metalworking,
- Bilingual- English/French
- Publications-
  - Combined TPD and XPS Study of Ligation and Decomposition of 1,6-Hexanedithiol on Size-Selected Copper Clusters Supported on HOPG
  - A novel approach to the island of stability of super-heavy elements search
  - Evidence for Resonances in the 7 α disassembly of Si 28
  - Examination of evidence for resonances at high excitation energy in the 7 α disassembly of Si 28
  - Alpha Conjugate Neck Structures in the Collisions of 35 MeV/nucleon 40Ca with 40Ca